Cell

Article

Fine-tuning of gene expression through the Mettl3-Mettl14-Dnmt1 axis controls ESC differentiation

Graphical abstract

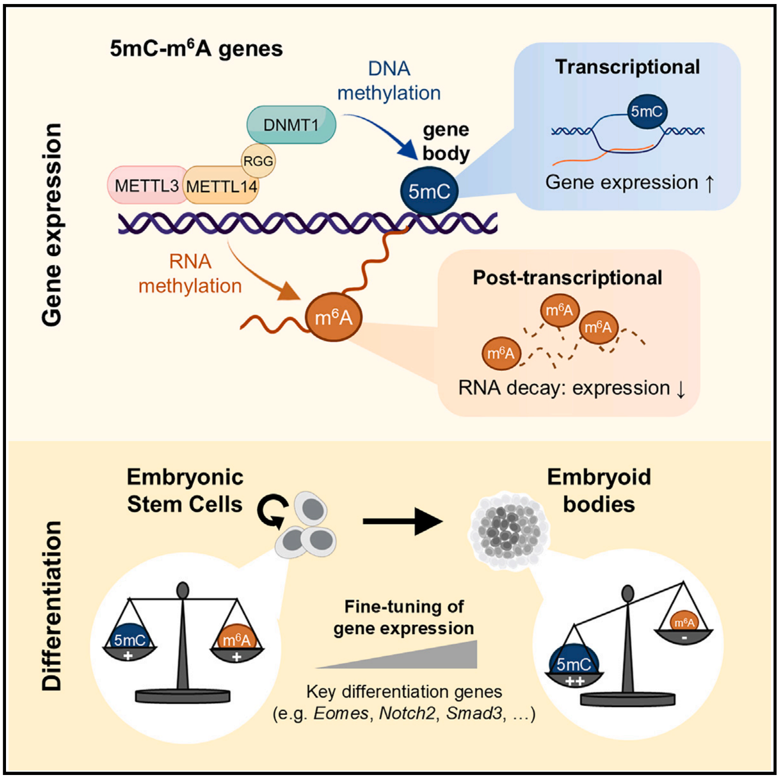

Highlights

- METTL3-METTL14 recruits DNMT1 to chromatin for gene-body methylation
- 5mC on DNA and m^6A on RNA frequently co-occur at the same targets
- The opposite effects of 5mC and m^6A fine-tune the expression of common target genes
- The shifting balance between these marks controls key differentiation genes in ESCs

Authors

Giuseppe Quarto, Andrea Li Greci,
Martin Bizet, ..., Rachel Deplus,
Evelyne Collignon, François Fuks

Correspondence

francois.fuks@ulb.be

In brief

Beyond its role as RNA m^6A writer, METTL3-METTL14 can mediate 5mC deposition on DNA by recruiting the DNA methyltransferase DNMT1 to chromatin. The two marks co-orchestrate the expression of key genes in differentiating ESC, allowing proper exit from pluripotency.

Quarto et al., 2025, Cell *188*, 998–1018

https://doi.org/10.1016/j.cell.2024.12.009

CellPress

CellPress

Cell

Article

Fine-tuning of gene expression through the Mettl3-Mettl14-Dnmt1 axis controls ESC differentiation

Giuseppe Quarto,[1,12] Andrea Li Greci,[1,12] Martin Bizet,[1,12] Audrey Penning,[1] Irina Primac,[1] Frédéric Murisier,[1] Liliana Garcia-Martinez,[2] Rodrigo L. Borges,[2] Qingzeng Gao,[3,4] Pradeep K.R. Cingaram,[2] Emilie Calonne,[1] Bouchra Hassabi,[1] Céline Hubert,[1] Adèle Herpoel,[1] Pascale Putmans,[1] Frédérique Mies,[1] Jérôme Martin,[1] Louis Van der Linden,[1] Gaurav Dube,[1] Pankaj Kumar,[1] Romuald Soin,[5] Abhay Kumar,[6] Anurag Misra,[6] Jie Lan,[1] Morgane Paque,[7,8] Yogesh K. Gupta,[6] Arnaud Blomme,[7,8] Pierre Close,[7,8] Pierre-Olivier Estève,[9] Elizabeth A. Caine,[10] Kristin M. Riching,[10] Cyril Gueydan,[5] Danette L. Daniels,[11] Sriharsa Pradhan,[9] Ramin Shiekhattar,[2] Yael David,[3,4] Lluis Morey,[2] Jana Jeschke,[1] Rachel Deplus,[1] Evelyne Collignon,[1] and François Fuks[1,13,*]

[1]Laboratory of Cancer Epigenetics, Faculty of Medicine, ULB-Cancer Research Center (U-CRC), Université libre de Bruxelles (ULB), Institut Jules Bordet, Brussels, Belgium
[2]Sylvester Comprehensive Cancer Center, Department of Human Genetics, University of Miami Miller School of Medicine, Miami, FL, USA
[3]Chemical Biology Program, Memorial Sloan Kettering Cancer Center, New York, NY, USA
[4]Department of Pharmacology, Weill Cornell Medicine, New York, NY, USA
[5]Laboratory of Molecular Biology of the Gene, Department of Molecular Biology, Université libre de Bruxelles (ULB), Gosselies, Belgium
[6]Greehey Children's Cancer Research Institute and Department of Biochemistry and Structural Biology, University of Texas Health Science Center, San Antonio, TX, USA
[7]Laboratory of Cancer Signaling, GIGA-Institute, University of Liège, Liège, Belgium
[8]WELBIO Department, WEL Research Institute, Wavre, Belgium
[9]New England Biolabs, Inc., Ipswich, MA, USA
[10]Promega Corporation, Madison, WI, USA
[11]Foghorn Therapeutics, Cambridge, MA, USA
[12]These authors contributed equally
[13]Lead contact
*Correspondence: francois.fuks@ulb.be

https://doi.org/10.1016/j.cell.2024.12.009

SUMMARY

The marking of DNA, histones, and RNA is central to gene expression regulation in development and disease. Recent evidence links N6-methyladenosine (m^6A), installed on RNA by the METTL3-METTL14 methyltransferase complex, to histone modifications, but the link between m^6A and DNA methylation remains scarcely explored. This study shows that METTL3-METTL14 recruits the DNA methyltransferase DNMT1 to chromatin for gene-body methylation. We identify a set of genes whose expression is fine-tuned by both gene-body 5mC, which promotes transcription, and m^6A, which destabilizes transcripts. We demonstrate that METTL3-METTL14-dependent 5mC and m^6A are both essential for the differentiation of embryonic stem cells into embryoid bodies and that the upregulation of key differentiation genes during early differentiation depends on the dynamic balance between increased 5mC and decreased m^6A. Our findings add a surprising dimension to our understanding of how epigenetics and epitranscriptomics combine to regulate gene expression and impact development and likely other biological processes.

INTRODUCTION

Epigenetic modifications on DNA and histones are intimately connected so as to dynamically regulate chromatin structures and orchestrate gene expression and cellular functions.[1–3] A major layer of gene expression control is DNA methylation (5mC [5-methylcytosine]), occurring at CpG dinucleotides. The DNA methyltransferase family (DNMT1, DNMT3A, and DNMT3B), responsible for DNA methylation, is indispensable for mammalian tissue development and homeostasis.[4–6] DNA methylation at promoters is well-known to transcriptionally repress the formation of coding and non-coding RNA.[7] In gene bodies, it correlates positively with gene expression.[8–10] The distribution of the mark is strongly influenced by interplay with histone modifications.[11–14] For instance, H3K36me3, a histone modification frequent at the bodies of actively transcribed genes, favors gene-body methylation via DNMT3B.[14,15] Promoter methylation is well known for critical roles played in embryonic development by repressing

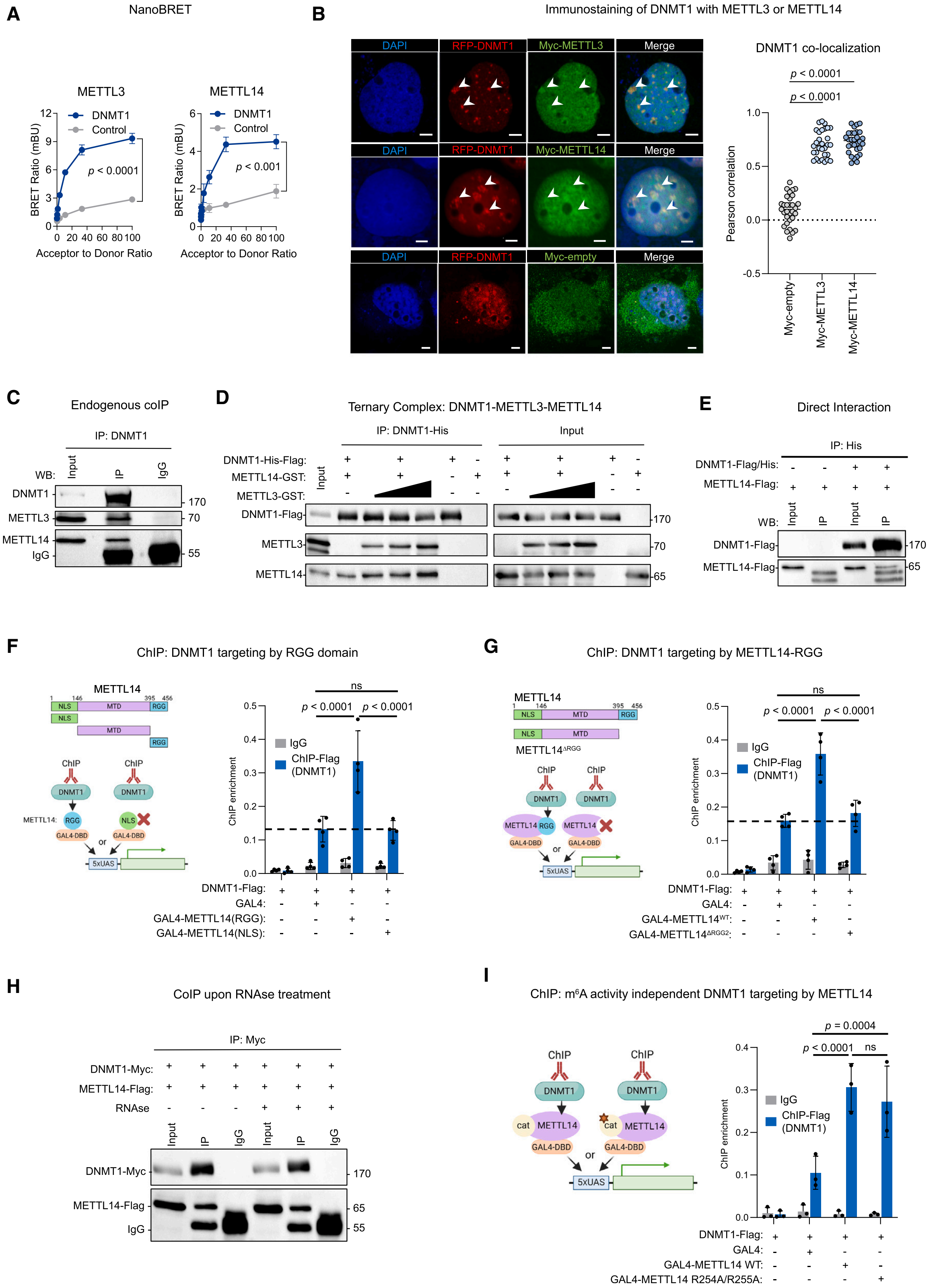

(legend on next page)

self-renewal genes. Less explored is the contribution of intragenic methylation in activating lineage-determining genes.[11,14,16,17]

Alongside DNA and histones, mRNA has recently been discovered as a substrate of epigenetic modifications, a discovery having led to the emergence of "epitranscriptomics." N^6-methyladenosine (m^{6}A) is the most prevalent internal modification in eukaryotic mRNA[18,19] and is an essential player in multiple post-transcriptional processes, e.g., RNA stability and translation efficiency.[20,21] It is notably involved in mammalian development,[22–24] wherein m^{6}A on mRNAs encoding key regulators of pluripotency ensures their rapid, timely downregulation in response to developmental cues, which in turn allows differentiation to occur.[23] This mark is deposited co-transcriptionally by the METTL3-METTL14 core methyltransferase complex at thousands of sites in the transcriptome,[25] especially in the 3′ end and stop codon.[20,26,27] Beyond regulating mRNA metabolism,[22,25,28,29] m^{6}A and its machinery influence the state of chromatin and control gene expression by affecting several modified histones.[30,31] For example, Li et al. have shown that the METTL3-METTL14 complex promotes H3K9me2 demethylation and gene expression via m^{6}A readers.[32] Further studies have shown that recruitment of METTL3-METTL14 to chromatin and subsequent m^{6}A deposition could be guided by chromatin-associated proteins and histone modifications, including H3K36me3.[29,33,34] Recent evidence also indicates that both METTL3 and METTL14 can regulate the chromatin landscape independently of m^{6}A.[35–39]

While connections between m^{6}A and histone modifications are gradually emerging, only hints of links between m^{6}A and DNA methylation have been reported. So far, three studies point to a link between the m^{6}A machinery and DNA modifications[31,40,41]: one descriptively suggests a link between m^{6}A and 5mC[31] and the other two provide evidence of a mechanistic link between m^{6}A readers and DNA hydroxymethylation via the TET (ten-eleven translocation) enzymes.[40,41]

The mechanisms, functions, and biological relevance of such connections are still poorly known. Are m^{6}A, 5mC, and their related enzymes directly connected? Do epigenetic and epitranscriptomic marks jointly regulate gene expression? What is the physiological role of this interplay? Tackling these questions in this study, we have made significant advances at all three levels. First, we identify a mechanism for gene-body methylation: recruitment of the 5mC writer DNMT1 by METTL3-METTL14, followed by deposition of the mark in the gene-body. Specifically, chromatin-bound METTL3-METTL14 interacts with DNMT1 via the METTL14 RGG domain, independently of the m^{6}A mark and apart from the well-known H3K36me3-DNMT3A-DNMT3B axis.[13–15] Second, a distinct mode of gene expression regulation emerges from the frequent co-occurrence of both marks at shared targets: combination of a transcriptional effect of gene-body 5mC with a post-transcriptional effect of m^{6}A. Thus, although m^{6}A is not involved in DNMT1 recruitment, it does play a major role, post-transcriptionally, in gene expression regulation. Third, we show how the combined effects of 5mC and m^{6}A on gene expression relate to a biological process: embryonic stem-to-embryoid body (ES-to-EB) differentiation. Specifically, 5mC favors gene transcription, whereas m^{6}A reduces transcript stability. During differentiation, a shift in the balance between the two marks influences expression of key differentiation genes. Overall, our findings suggest that fine-tuning of gene expression via the METTL3-METTL14-DNMT1 axis is critical for differentiating embryonic stem cells (ESCs).

RESULTS

The DNA methyltransferase DNMT1 is recruited to chromatin by METTL3-METTL14

In this study, we aimed to better understand the emerging link between epigenetics and epitranscriptomics. We began by searching for partners of METTL3 and METTL14 and unexpectedly found that they interact with the well-known DNA methyltransferase DNMT1. We first performed a NanoBRET (bioluminescence resonance energy transfer) binding assay with NanoLuc-tagged METTL3 or METTL14 (BRET donors) and HaloTag-tagged DNMT1 (BRET acceptor). DNMT1 was closely associated with METTL3 and METTL14 (Figure 1A). We then used immunostaining to investigate the subcellular localization of these proteins. All three proteins, presenting as punctate spots, displayed their reported nuclear localization,[27,28,42] with co-localization observed between RFP-DNMT1 and Myc-METTL3 or METTL14 (Figures 1B and S1A). No co-localization was found with the tags alone (Figures 1B and S1A).

Next, we performed co-immunoprecipitation (coIP) in HeLa cells and found FLAG-METTL14 to interact with Myc-DNMT1 (Figure S1B). Importantly, DNMT1 co-precipitated with both

Figure 1. The DNA methyltransferase DNMT1 is recruited to chromatin by METTL3-METTL14

(A) NanoBRET energy transfer indicates that NanoLuciferase-METTL3 and -METTL14 are in close proximity to Halo-DNMT1 in living HEK293 cells (HaloTag as negative control, *n* = 4).

(B) Immunostaining showing co-localization of transiently expressed DNMT1 with METTL3 or METTL14 in the nuclei of COS-7 cells. Scale bars: 5 μm, horizontal bar: median.

(C) Endogenous co-immunoprecipitation (coIP) of DNMT1 with METTL3 and METTL14 in HeLa cells (*n* = 3).

(D) *In vitro* coIP shows increased DNMT1-METTL14 interaction with rising METTL3 levels (*n* = 2).

(E) Direct interaction between recombinant METTL14 and DNMT1, observed by *in vitro* pull-down followed by western blotting (*n* = 3).

(F and G) Recruitment of DNMT1 to chromatin assessed by ChIP-qPCR in the GAL4-5XUAS system. In HEK2935XUAS cells, DNMT1 is recruited by the METTL14 RGG domain or by full-length METTL14, but not by the NLS domain nor by METTL14-ΔRGG2 (*n* = 4).

(H) RNase treatment does not impair the interaction of METTL14-FLAG with DNMT1-Myc, as assessed co-immunoprecipitation in HeLa cells (*n* = 3).

(I) Recruitment of DNMT1 to chromatin by METTL14 is independent of m^{6}A activity (*n* = 3). ChIP-qPCR in the GAL4-5XUAS system performed as in Figure 1G but using a GAL4-tagged METTL14 mutant (R254/255A) unable to support METTL3-mediated m^{6}A methylation.[86]

All data are means ± SEM (A) or means ± SD (F, G, and I). *p* values by two-way ANOVA (A), Pearson's correlation analysis (B), and two-tailed unpaired t test (F, G, and I).

See also Figure S1.

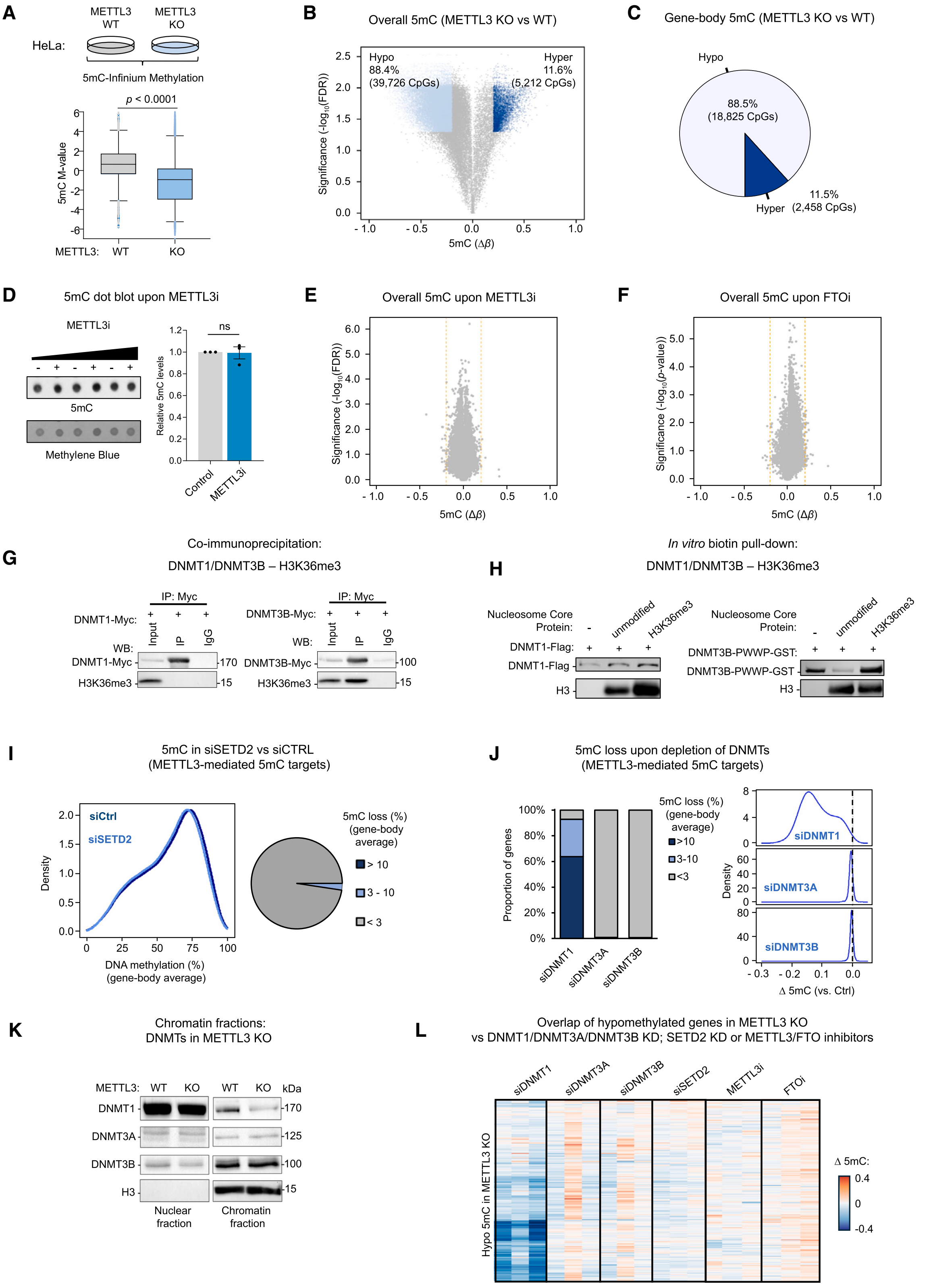

(legend on next page)

METTL3 and METTL14 in endogenous coIP experiments (Figure 1C), and interestingly, METTL3 enhanced the interaction of METTL14 with DNMT1, which suggests the formation of a ternary complex (Figure 1D). *In vitro* pull-down experiments showed that DNMT1 interacts directly with recombinant METTL14 protein (Figure 1E). We then identified the domain of METTL14 involved in this interaction: the essential arginine/glycine-rich RNA-binding (RGG)[43] domain (Figure S1C). A METTL14 variant lacking this domain (METTL14$^{\Delta RGG}$) proved unable to interact with DNMT1 (Figure S1D). Taken together, our data support the direct binding of DNMT1 to METTL14 in the context of the METTL3-METTL14 complex.

The above data prompted us to assess whether METTL3-METTL14 regulates DNMT1 recruitment to chromatin. Using METTL14-GAL4 tethering combined with DNMT1 chromatin immunoprecipitation (ChIP), we observed increased DNMT1 chromatin occupancy in the presence of either full-length METTL14 or its RGG subdomain (Figures 1F and 1G). By contrast, the METTL14$^{\Delta RGG2}$ variant did not enhance DNMT1 chromatin binding (Figures 1G and S1E), despite the similar recruitment of the GAL4 constructs to the integrated 5xGAL4 promoter (Figures S1F–S1H). These results are in line with our above observation that the RGG domain mediates the METTL14-DNMT1 interaction (Figures S1C–S1E).

An important question was whether the m^{6}A-depositing catalytic activity of METTL3-METTL14 is required to recruit DNMT1 to chromatin since both METTL3 and METTL14 can function independently of their m^{6}A-related enzymatic activity.[35,37] First, coIP following RNase treatment revealed that the interaction between DNMT1 and METTL14 does not require RNA scaffolding (Figure 1H). Second, in GAL4 tethering assays, using a METTL14-R254/255A mutant that suppresses m^{6}A deposition did not affect DNMT1 recruitment, as compared with METTL14 wild type (WT) (Figures 1I and S1I). These findings indicate that METTL14 recruits DNMT1 to chromatin via its RGG domain, independently of its effect on catalytic activity.

METTL3 promotes DNMT1-dependent gene-body methylation

Considering the essential role of DNMT1 in genome-wide DNA methylation[4] and its observed binding to METTL3-METTL14 (Figure 1), we investigated whether METTL3-METTL14 contributes to DNA methylation homeostasis. We knocked out METTL3 in HeLa cells (METTL3 knockout [KO]) and compared them with WT cells (Figure S2A). Genome-scale DNA methylation profiling with the Infinium methylation EPIC array revealed, upon METTL3 KO, a major decrease in global 5mC levels (Figures 2A, 2B and S2B–S2D; Table S3). We confirmed these findings using a second METTL3 KO clone (Figures S2A and S2B). Remarkably, most hypomethylated sites were found in gene-bodies (Figure 2C). It is worth stressing, furthermore, that the observed hypomethylation could not be attributed to changes in expression of the DNA methyltransferases (DNMT1, DNMT3A, and DNMT3B; see Figure S2E). Overall, we conclude that METTL3-METTL14 favors gene-body 5mC deposition through DNMT1 recruitment to chromatin (Figure 1).

We next assessed the possible contribution of the m^{6}A mark itself to regulating the deposition of 5mC. Treating HeLa cells with inhibitors targeting either the m^{6}A writer METTL3[44] or the m^{6}A eraser FTO (fat mass and obesity associated)[45] did not globally affect 5mC (Figures 2D–2F and S2F). Nor did targeting m^{6}A demethylation by means of a dCasRx-ALKBH5 fusion protein[46] result in any decrease in local 5mC levels (Figures S2G–S2I). Thus, our findings indicate that the METTL3-METTL14 complex, but not the m^{6}A mark itself, promotes both DNMT1 recruitment (Figure 1G–1I) and gene-body DNA methylation (Figures 2A–2F).

Gene-body methylation is well known to occur via the H3K36me3-DNMT3A-DNMT3B axis.[13–15] Therefore, we investigated whether this histone mark is involved in the DNA hypomethylation observed following METTL3 depletion. First, coIP in HeLa cells indicated that DNMT1, unlike DNMT3B, does not bind H3K36me3 (Figure 2G). Second, direct *in vitro* pull-down assays showed that DNMT1 exhibited no preference for H3K36me3-modified over unmodified recombinant nucleosomes, whereas the PWWP (proline-tryptophan-tryptophan-proline) domain of DNMT3B displayed the expected preferential binding to H3K36me3 (Figure 2H).

We then performed knockdown of SETD2, which catalyzes H3K36me3 formation, and measured both H3K36me3 and 5mC. As expected, we observed a global decrease in H3K36me3 (Figure S2J), yet DNA methylation profiling revealed

Figure 2. METTL3 facilitates DNMT1-dependent gene-body DNA methylation

(A) Reduced 5mC levels (M value) in METTL3 KO HeLa cells, based on the 50,000 most variable CpGs ($n = 3$).

(B) Volcano plot of 5mC changes in METTL3 KO HeLa cells, with significantly hypo- and hypermethylated sites as light and dark blue dots (corrected p value < 0.05 and $\Delta\beta$ value > 0.2).

(C) Percentage of gene-body 5mC changes in METTL3 KO HeLa cells (measured as in Figure 2B).

(D) Dot blotting in HeLa cells treated with METTL3 inhibitor STM-2457 (1, 5, and 25 μM) shows no difference in 5mC levels ($n = 3$; ns: not significant). Data (quantified for 25 μM) as means ± SEM.

(E and F) Volcano plot showing no changes in 5mC following METTL3 (STM-2457; E) or FTO (FB23-2; F) inhibitor treatment ($n = 3$).

(G and H) DNMT1 does not bind H3K36me3 by coIP in HeLa cells transiently expressing DNMT1-Myc (G) and *in vitro* pull-down of recombinant FLAG-tagged DNMT1 by unmodified and H3K36me3-modified nucleosomes (H). DNMT3B and recombinant glutathione S-transferase (GST)-PWWP domain of DNMT3B as positive controls ($n = 3$).

(I) SETD2 knockdown in HeLa cells has very limited impact on METTL3-dependent gene-body DNA methylation ($n = 3$).

(J) Knockdown of DNMT1, DNMT3A, or DNMT3B in HeLa cells reveals that METTL3-dependent gene-body 5mC mostly relies on DNMT1 ($n = 3$).

(K) METTL3 KO impairs DNMT1 binding to chromatin, but not that of DNMT3A or DNMT3B ($n = 3$).

(L) DNA methylation changes among METTL3-dependent 5mC genes in HeLa cells after knockdown of DNMT1, DNMT3A/DNMT3B, or SETD2, or perturbation of m^{6}A (by METTL3i or FTOi).

p values by two-tailed t test (A and D).

See also Figure S2.

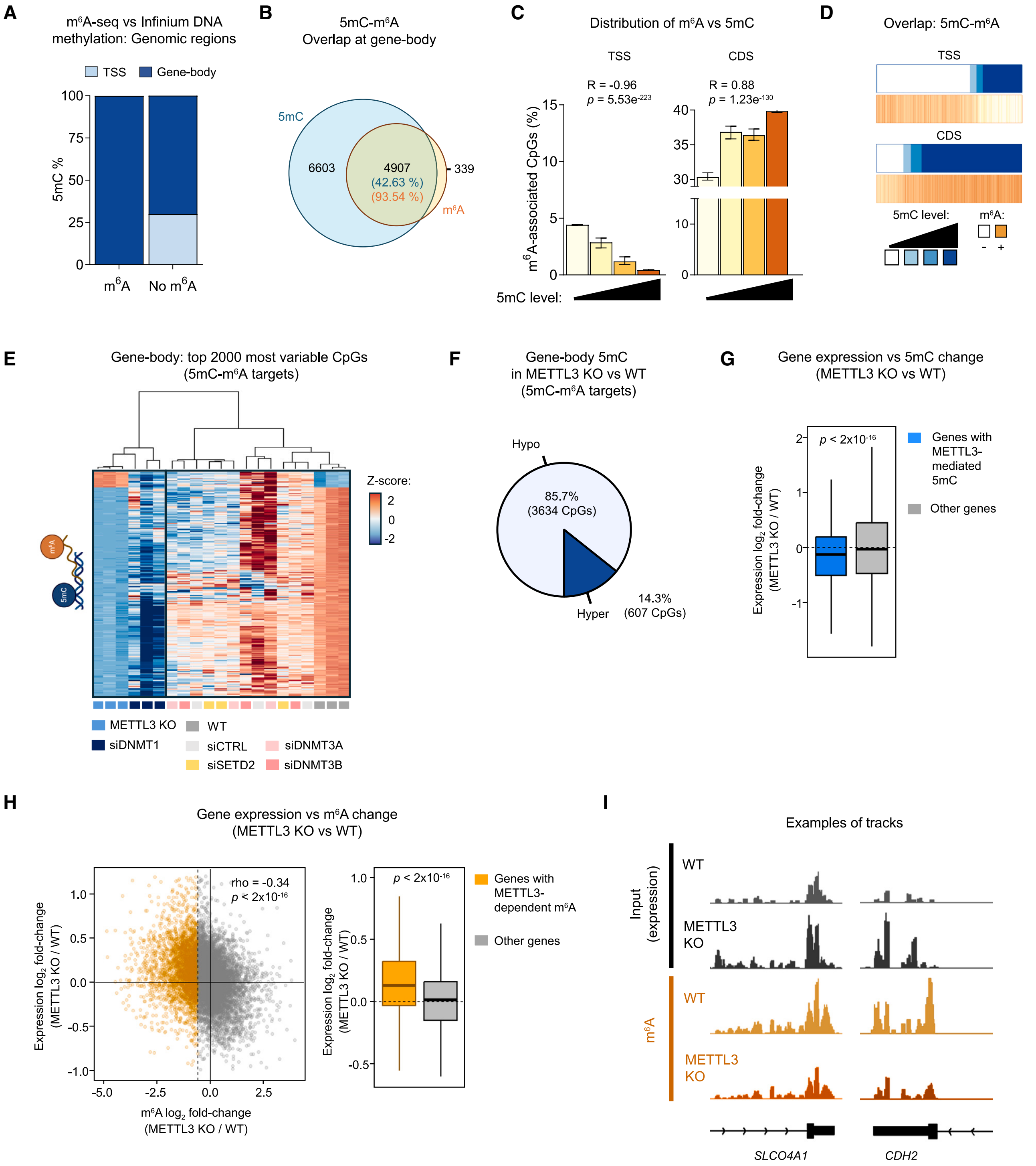

Figure 3. 5mC and m^{6}A contribute together to regulating the expression of common target genes

(A) In HeLa cells, gene-body 5mC strongly co-occurs with coding-sequence m^{6}A.

(B) Venn diagram of the overlap between 5mC-marked gene-bodies (mean β value > 0.25) and m^{6}A-marked coding sequences (peak in m^{6}A-seq).

(C) Proportion of m^{6}A-associated CpGs by 5mC level (0%–25%, 25%–50%, 50%–75%, 75%–100% β value), determined in the TSS and CDS by bootstrapping (STAR Methods).

(D) Association between 5mC and m^{6}A in TSS (top) and CDS (bottom). CpGs grouped by 5mC levels (0%–25%, 25%–50%, 50%–75%, 75%–100% β value) and by m^{6}A association or lack thereof.

(E) 5mC levels of the top 2,000 most variable intragenic CpGs among 5mC-m^{6}A target genes show dependence on METTL3 and DNMT1.

(legend continued on next page)

no notable decrease in 5mC among genes identified as depending on METTL3 for gene-body methylation (Figure 2I). This result indicates that the here-identified mechanism of gene-body methylation, depending on DNMT1-METTL3-METTL14, does not involve H3K36me3 as a determinant.

To assess how different DNMTs might contribute to METTL3-mediated 5mC deposition in gene-bodies, we knocked down DNMT1, DNMT3A, or DNMT3B in HeLa cells (Figure S2K). First, DNMT1 depletion strongly reduced 5mC within gene-bodies (Figure S2L). This indicates that, alongside the well-known role of DNMT3A and DNMT3B,[13–15] DNMT1 also contributes to intragenic 5mC deposition, consistent with previous reports.[47–49] As shown in Figure 2J, “METTL3-dependent” gene-body 5mC sites mostly rely on DNMT1, the roles of DNMT3A and DNMT3B being marginal at these sites. In subcellular fractionation, METTL3 depletion led to reduced chromatin binding by DNMT1, but not by DNMT3A/DNMT3B (Figure 2K). This further indicates that METTL3 recruits DNMT1 to chromatin for DNA methylation but affects neither DNMT3A nor DNMT3B. Moreover, we found an overlap between gene-body hypomethylation upon METTL3 KO and genes whose 5mC marking is DNMT1-dependent (Figure 2L). We found no such overlap with DNMT3A- or DNMT3B-dependent 5mC marking (Figure 2L). As expected, however, we observed an overlap between genes that are hypomethylated upon SETD2 depletion and those hypomethylated upon DNMT3A or DNMT3B depletion, thus confirming the previously established H3K36me3-DNMT3A/DNMT3B axis (Figure S2M). Overall, the H3K36me3-DNMT3A/DNMT3B axis appears dispensable for the methylation of gene-bodies targeted by METTL3 (Figures 2I, 2J, and S2M). Perturbing m^{6}A levels likewise did not affect DNA methylation at METTL3-dependent sites (Figure S2N).

Collectively, these results indicate that METTL3-METTL14 favors gene-body DNA methylation by recruiting DNMT1 to chromatin, independently of the m^{6}A mark itself and of the previously established H3K36me3-DNMT3A/DNMT3B mechanism.

Both 5mC and m^{6}A contribute to regulating the expression of common target genes

Having established the mechanism of DNMT1 recruitment to chromatin by METTL3-METTL14, we investigated its functional impact. As METTL3 acts as DNMT1 recruiter and mediator of 5mC deposition (cf. Figures 1 and 2) as well as m^{6}A writer, we investigated whether 5mC and m^{6}A co-occur on the same targets. Integrated analysis of m^{6}A sequencing (m^{6}A-seq) and genome-scale DNA methylation in HeLa cells revealed that genes with m^{6}A-modified RNAs are frequently marked by 5mC, and almost exclusively in gene-bodies (Figures 3A, 3B, S3A, and S3B). In CDS (coding DNA sequence) regions, but not TSS (transcription start site) regions, we observed a strong positive correlation between m^{6}A sites and 5mC levels (Figures 3C and 3D). Noteworthily, nearly half of the identified 5mC-m^{6}A targets contain intragenic CGIs, and these genes are often associated pluripotency mechanisms (Figure S3C). Together, these results reveal a significant co-occurrence between 5mC on DNA (mostly in gene-bodies) and m^{6}A on RNA.

Focusing on 5mC-m^{6}A target genes, we observed global gene-body hypomethylation following METTL3 or DNMT1 depletion (Figures 3E and 3F). By contrast, H3K36me3, DNMT3A, and DNMT3B did not seem involved in methylating CpGs at 5mC-m^{6}A targets (Figure 3E). These observations support a model where METTL3 recruits DNMT1 to promote 5mC deposition at 5mC-m^{6}A targets. Gene-body methylation is common in highly expressed genes in mammals, although the molecular basis of this observation remains unclear.[8–10] Having found strong co-occurrence of gene-body 5mC with m^{6}A (on the corresponding transcript), we examined whether and how 5mC and m^{6}A might co-contribute to regulating gene expression. RNA sequencing (RNA-seq) revealed significant downregulation among genes hypomethylated upon METTL3 depletion (Figure 3G), suggesting that METTL3-dependent 5mC favors gene expression, in line with the expected correlation between gene-body DNA methylation and transcription.[8–10,15,50,51]

Considering the dual role of METTL3 as mediator of 5mC deposition and as m^{6}A writer, we examined how the presence of m^{6}A affects transcript levels. First, transcriptome-wide mapping of m^{6}A revealed, as expected, a global decrease in m^{6}A upon METTL3 depletion (Figure S3D). Remarkably, we observed a negative correlation between m^{6}A levels and gene expression, reduced m^{6}A being associated with upregulation upon METTL3 KO (Figures 3H and 3I). Since m^{6}A is known to promote RNA degradation,[23,24,52] RNA stability was profiled by actinomycin D assay, and, in line with our prior results (Figures 3H and 3I), we found reduced m^{6}A to be globally associated with increased RNA stability (Figure S3E). By comparison, polysome profiling showed no correlation between translation efficiency and m^{6}A changes (Figure S3F). Upon METTL3 depletion, loss of m^{6}A thus appears to promote gene expression through increased transcript stability. Hence, in this context, METTL3-mediated m^{6}A deposition appears to modulate gene expression predominantly by affecting RNA stability. Altogether, these data suggest that both marks influence gene expression, with METTL3-dependent gene-body 5mC likely favoring gene expression and m^{6}A exerting a post-transcriptional downregulating effect through decreased RNA stability.

Overall, our findings point to a distinct mechanism of gene-body methylation by DNMT1 via METTL3-METTL14, independently of the m^{6}A mark itself. Furthermore, despite m^{6}A not being involved in DNMT1 recruitment, it may still play a major functional role. Indeed, as METTL3-METTL14 is involved in depositing both 5mC and m^{6}A, and as the two marks tend to co-occur, our results suggest that both marks may regulate

---

(F) Percentage of gene-body CpGs within 5mC-m^{6}A targets with decreased or increased 5mC in METTL3 KO HeLa cells.

(G) Genes exhibiting hypomethylation ($\Delta\beta < -0.2$) upon METTL3 KO are globally downregulated by RNA-seq ($n = 3$). Two-tailed Wilcoxon test.

(H and I) Genes showing reduced m^{6}A (1.5-fold decrease) in METTL3 KO show increased gene expression, as determined by IP and input of m^{6}A-seq, respectively ($n = 2$). Spearman correlation analysis and two-tailed t test.

See also Figure S3.

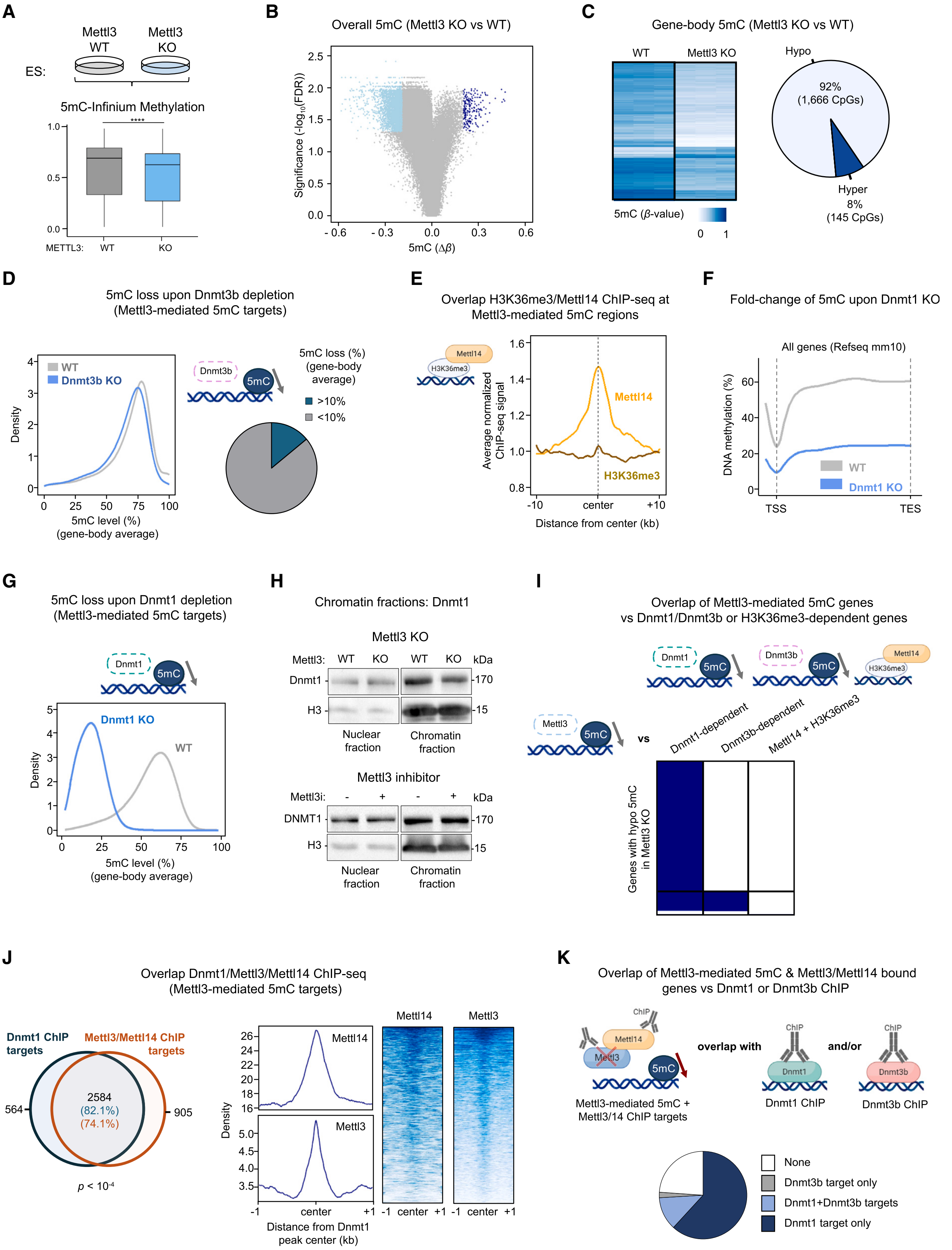

(legend on next page)

together the expression of common targets through their respective transcriptional and post-transcriptional effects.

Mettl13-Mettl14 regulates DNMT1-dependent gene-body DNA methylation in ESCs

To study the biological relevance of the METTL3-METTL14-DNMT1 axis, we investigated the dynamic regulation of m^6A and 5mC in ESCs, since these marks are known to orchestrate self-renewal and differentiation.[17,23,24,53,54] Consistent with our findings on HeLa cells, Mettl3 KO in ESCs induced global DNA hypomethylation, mostly in gene-bodies (Figures 4A–4C and S4A), despite no change in total Dnmt levels (Figure S4B). Moreover, reanalyzing data from Xu et al.[31] confirmed that Mettl3 KO ESCs display decreased gene-body 5mC (Figure S4C).

In ESCs, notably, H3K36me3 is reported to both recruit Dnmt3b for gene-body methylation and interact with Mettl14[14,15,33] (Figures S4D–S4F). Therefore, using public H3K36me3, Dnmt3b, Mettl3, and Mettl14 ChIP data and public genome-wide 5mC data for Dnmt3b KO,[15,35,52,55] we examined whether Mettl3-dependent gene-body 5mC deposition is mediated by the H3K36me3-Dnmt3b or H3K36me3-Mettl14 axis. First, only a minority of "Mettl3-dependent" gene-body targets were hypomethylated upon KO of Dnmt3b (Figures 4D and S4D). Second, Mettl14 ChIP-seq, but not H3K36me3 ChIP-seq, displays enriched signal at regions of Mettl3-mediated 5mC deposition (Figure 4E). Thus, the intragenic hypomethylation observed in Mettl3 KO ESCs does not depend on Dnmt3b, nor is it associated with H3K36me3.

We next assessed whether Dnmt1 plays a key role in Mettl3-mediated gene-body 5mC deposition in ESCs (as in HeLa cells). First, in agreement with previous studies,[47–49] Dnmt1 KO strongly reduced DNA methylation (Figure 4F). Second, in contrast to Dnmt3b depletion and consistently with findings on HeLa cells (Figure 2), Dnmt1 depletion strongly affected DNA methylation in targets of Mettl3-mediated 5mC deposition (Figures 4G, S4G, and S4H). Furthermore, chromatin fractionation showed impaired Dnmt1 binding to chromatin upon Mettl3 KO, but not upon inhibition of Mettl3 catalytic activity (Figure 4H). Accordingly, and as observed in HeLa cells, Mettl3 inhibition had no global effect on 5mC (Figures 2E and S4I). Overall, most genes hypomethylated in Mettl3 KO ESCs also appeared to depend on Dnmt1 for 5mC deposition, with only a fraction relying on both Dnmt1 and Dnmt3b (Figure 4I). Likewise, no overlap appeared between genes showing Mettl3-dependent 5mC deposition and genomic regions where Mettl14 acts as H3K36me3 reader (Figure 4I). Next, examining public Mettl3, Mettl14, and Dnmt1 ChIP-seq data for targets of Mettl3-mediated 5mC deposition, we found Dnmt1 to largely colocalize with Mettl3 and Mettl14 (Figure 4J). This is consistent with our observation that DNMT1 interacts with both METTL3 and METTL14 in HeLa cells (Figures 1C and 1D), further supporting that DNMT1 is recruited by the METTL3-METTL14 complex. Furthermore, in ESCs, Mettl3-Mettl14 ChIP targets exhibiting 5mC hypomethylation upon Mettl3 depletion primarily overlap with Dnmt1 targets (defined by either chromatin occupancy or 5mC dependency), only a few being identified as shared Dnmt1/Dnmt3b targets and even fewer as Dnmt3b-only targets (Figures 4K and S4J).

Overall, we uncover a mechanism of gene-body methylation and a distinct set of genes that do not depend on the presence of either H3K36me3 or Dnmt3b for their gene-body methylation. We reveal a mode of gene-body methylation that depends on Dnmt1 recruitment by Mettl3-Mettl14.

Coordinated regulation of gene expression through 5mC and m^6A in ESCs

In light of the dual function of Mettl3-Mettl14 as mediator of Dnmt1-dependent 5mC deposition (Figure 4) and as m^6A writer, we next examined in ESCs the potential co-occurrence of 5mC (on genes) and m^6A (on the corresponding transcripts). Consistent with our findings on HeLa cells, we found 5mC, particularly in gene-bodies, to co-occur frequently with m^6A (Figures 5A–5C). Our HeLa data (Figure 3) having hinted that both marks might jointly regulate the expression of their common target genes (5mC at the transcriptional level and m^6A at the post-transcriptional level), we sought to dissect the effects of both marks in ESCs.

First, as gene-body methylation is reported to correlate with active transcription,[56] we tracked nascent RNA synthesis by

Figure 4. In ESCs, Mettl3-Mettl14 partner with Dnmt1 for DNA methylation deposition in gene-bodies

(A) Reduced 5mC levels in Mettl3 KO ESCs ($n = 3$).

(B) 5mC changes ($\Delta\beta$ value) in Mettl3 KO ESCs, with hypo- and hypermethylated sites in light and dark blue (corrected p value < 0.05 and $\Delta\beta > 0.2$).

(C) Reduced 5mC levels in gene-bodies (corrected p value < 0.05 and $\Delta\beta > 0.2$).

(D) Gene-bodies whose 5mC marking is Mettl3-dependent (defined as 5mC loss $\geq$10% in Mettl3 KO) are barely affected in Dnmt3b KO ESCs. From published data (GEO: GSE72856).[15]

(E) High signal in Mettl14 ChIP-seq,[35] but not in H3K36me3 ChIP-seq[55] among sites of Mettl3-dependent 5mC deposition. From published data (GEO: GSE206730 and GSE31039).

(F) Reduced 5mC across all genes in Dnmt1 KO ESCs ($n = 3$).

(G) Targets of Mettl3-mediated 5mC deposition depend on Dnmt1 for gene-body methylation.

(H) Subcellular protein fractionation indicates that Mettl3 knockout, but not catalytic inhibition, reduces Dnmt1 binding to chromatin in ESCs ($n = 2$).

(I) Chart showing, for genes with METTL3-dependent gene-body 5mC (total column height), the proportion (in blue) of genes showing Dnmt1 and/or Dnmt3b dependency (defined as 5mC loss $\geq$10% in the corresponding DNA methyltransferase knockout) or genes associated with Mettl14 binding to H3K36me3 (Mettl14 and H3K36me3 ChIP-seq overlap).

(J) Dnmt1 binding (by ChIP-seq[87]), Dnmt1 largely overlaps with Mettl3[52] and Mettl14[35] binding in genes with "Mettl3-dependent" gene-body 5mC. From published data (GEO: GSM2059182, GSE202848, and GSE206735).

(K) Among genes with "Mettl3-dependent" gene-body 5mC, there is a strong overlap of Mettl3-Mettl14 ChIP-seq targets with Dnmt1, but minimal overlap with Dnmt3b.

p values by two-tailed unpaired t test (A) and one-sided hypergeometric test (J).

See also Figure S4.

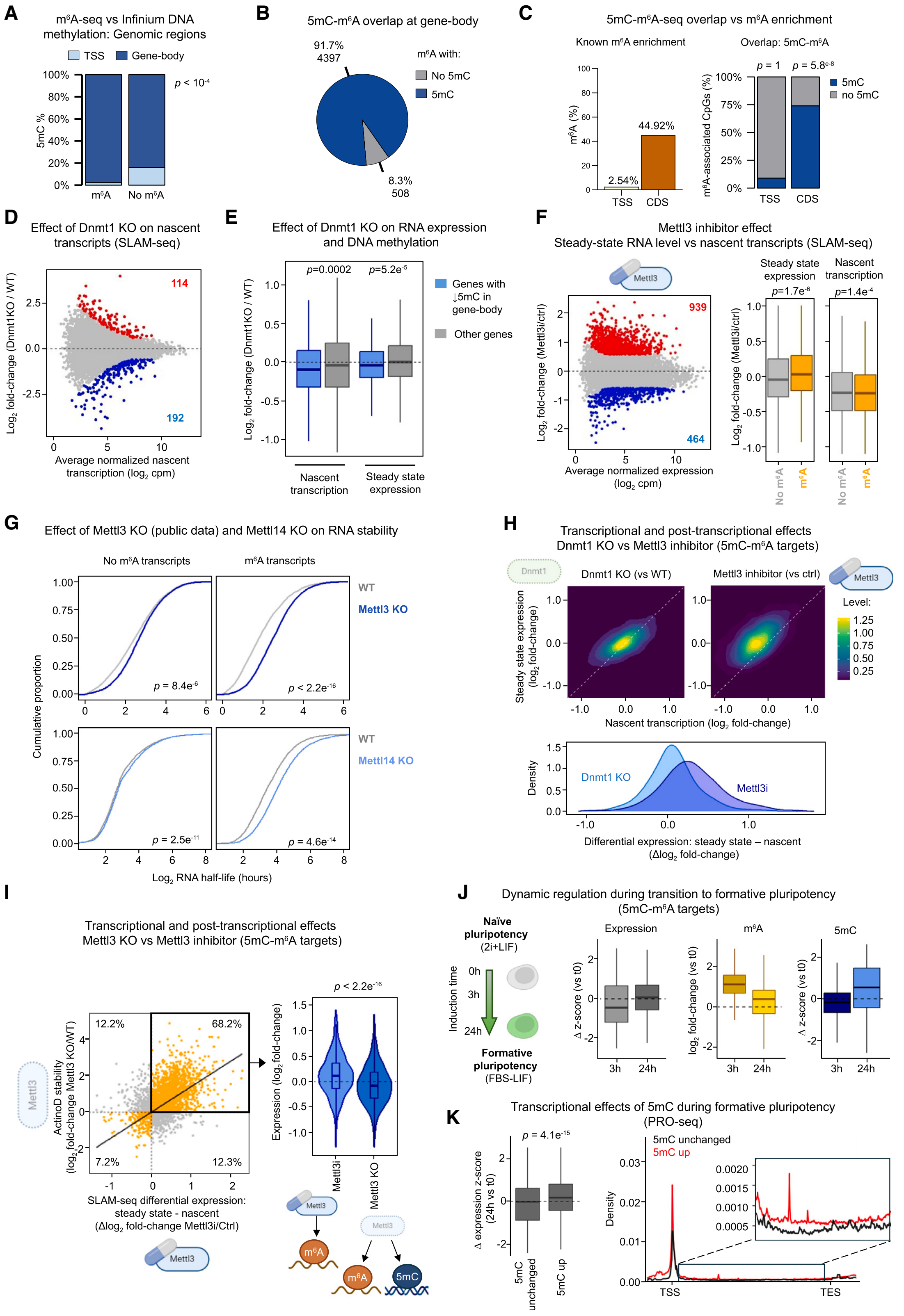

(legend on next page)

labeling new transcripts with a uridine analog[57–59] (SLAM-seq [thiol-linked alkylation for the metabolic sequencing of RNA], see STAR Methods and Figure S5A). In Dnmt1 KO ESCs, we observed both upregulation and downregulation of transcription (Figure 5D). Importantly, these transcriptional changes correlated with the 5mC status: genes hypomethylated in gene-bodies displayed both decreased transcriptional activity and downregulation of their steady-state expression level (Figures 5E, S5B, and S5C). We noted an opposite trend for genes displaying promoter hypomethylation, highlighting a location-specific impact of 5mC on transcription[56,60] (Figure S5B). Our findings underscore the role of DNA methylation in transcriptional regulation and indicate that Dnmt1-mediated intragenic methylation promotes transcriptional activity.

Next, we used acute catalytic inhibition of Mettl3 to evaluate the effect of m^{6}A on gene expression. This approach, unlike Mettl3 KO, enabled us to investigate m^{6}A without affecting DNA methylation, as seen in HeLa cells (Figures 2E, 4H, and S2G–S2I). SLAM-seq revealed significantly raised levels of m^{6}A-marked transcripts with no effect on nascent transcript formation, suggesting a post-transcriptional effect (Figure 5F). Re-analysis of public ESC data[61] further revealed increased stability of m^{6}A-marked transcripts upon Mettl3 KO (Figure 5G). Likewise, Mettl14 KO extended the half-lives of m^{6}A-bearing transcripts (Figures 5G and S5D–S5F). Mettl3 KO and Mettl14 KO had comparable effects on RNA stability (Figure S5G). Together, these results highlight that m^{6}A exerts a post-transcriptional effect, reducing RNA half-lives and steady-state expression levels. Both Mettl3 and Mettl14 contribute to this regulatory mechanism.

To further dissect the transcriptional vs. post-transcriptional effects of the two marks on common targets, we examined steady-state expression and nascent transcription (by SLAM-seq) following Dnmt1 depletion (affecting 5mC) or Mettl3 inhibition (affecting m^{6}A) (Figure S5H). Upon Dnmt1 depletion, we observed a strong correlation between changes in steady-state expression and in nascent transcript formation, suggesting mainly a transcriptional impact of 5mC on gene expression (Figures 5H and S5H). However, Mettl3 inhibition caused gene upregulation due to reduced transcript-destabilizing effect by m^{6}A (Figures 5H and S5H). Lastly, Mettl3 KO and inhibition of its catalytic activity had similar post-transcriptional effects on 5mC-m^{6}A targets (Figure 5I, left), likely related to m^{6}A loss. By contrast, while Mettl3 inhibition logically led to upregulation of steady-state RNA levels, this effect was absent in Mettl3 KO cells (Figure 5I, right). As Mettl3 KO affects both 5mC and m^{6}A and Mettl3 inhibition only affects m^{6}A, this discrepancy probably reflects transcriptional regulation. Overall, we uncover a combined effect on gene expression of an epigenetic mark (5mC) at the transcriptional level and an epitranscriptomic mark (m^{6}A) at the post-transcriptional level. Specifically, gene-body 5mC promotes gene expression through transcription, whereas m^{6}A represses gene expression by destabilizing RNAs, thus fine-tuning the expression of common target genes.

To provide additional functional insights, we investigated a previously described dynamic process involved in peri-implantation development: the transition from naive to formative pluripotency.[62–64] We observed a rapid increase in m^{6}A levels by 3h post-induction, whereas 5mC levels did not start to increase until 24 h (Figure 5J). Temporally, this rapid increase in m^{6}A coincided with decreased expression of shared 5mC-m^{6}A targets, whereas the later rise in 5mC was associated with a rebound in gene expression (Figure 5J). We thus hypothesized that m^{6}A initially downregulates expression, whereas 5mC later enhances it. Next, using nuclear run-on sequencing[59,65,66] (precision nuclear run-on sequencing [PRO-seq]) to map active transcription (Figure S5I), we found increased 5mC during induction to correlate with both higher steady-state expression (by RNA-seq) and active transcription (by PRO-seq), indicating a transcriptional effect (Figure 5K). By contrast, m^{6}A gain correlated with decreased expression but with no global changes in transcription, suggesting post-transcriptional regulation (Figure S5J). In conclusion, these data reinforce the notion that

Figure 5. The transcriptional effect of gene-body 5mC and the post-transcriptional effect of m^{6}A combine to regulate gene expression

(A) Distribution of 5mC sites (TSS vs. gene-body), according to corresponding transcript m^{6}A status.

(B) Strong overlap between genes with m^{6}A-marked transcripts and gene-body 5mC (mean β value > 0.25).

(C) Distribution of m^{6}A peaks (TSS vs. CDS) in ESCs (left) and proportions of 5mC-marked and -unmarked CpGs with m^{6}A-marked transcripts (right).

(D) SLAM-seq in Dnmt1 KO ESCs highlights changes in nascent transcription ($n = 3$), with significant up- and downregulation in red and blue, respectively (fold-change > 1.5 and corrected p value < 0.05).

(E) Decreased gene-body methylation in Dnmt1 KO ESCs coincides with reduced nascent transcription and reduced steady-state transcript levels.

(F) SLAM-seq in ESCs treated with 50 μM STM-2457 shows that while inhibition of Mettl3 catalytic activity increases steady-state levels of m^{6}A-marked RNAs, it does not affect nascent transcript formation ($n = 3$).

(G) Depletion of Mettl3 (from GEO: GSE86336)[61] or Mettl14 (in-house data, $n = 3$) increases the stability of transcripts that are normally m^{6}A-marked (by actinomycin D assay followed by RNA-seq).

(H) Comparison of nascent and steady-state transcript levels (SLAM-seq) for 5mC-m^{6}A targets indicates that Dnmt1 KO mostly affects transcription, whereas the effect of Mettl3 inhibition is post-transcriptional (top, see Figure S5H). Post-transcriptional regulation can be quantified by the difference between steady-state and nascent RNA levels (bottom).

(I) Mettl3 inhibition and KO display similar post-transcriptional effects (by SLAM-seq and actinomycin D assay) on 5mC-m^{6}A targets but different steady-state regulation (RNA-seq).

(J) Gene expression (input m^{6}A-seq), m^{6}A (m^{6}A-seq), and 5mC (Infinium array) were tracked during the transition from naive to formative pluripotency (at 0, 3, and 24 h, $n = 3$).

(K) Increased 5mC ($\Delta\beta > 0.1$) is associated with gene upregulation 24 h after induction of formative pluripotency (left). Precision nuclear run-on sequencing (PRO-seq) indicates a concomitant rise in active transcription (right, $n = 3$).

p values by chi-squared test (A), hypergeometric test (C), two-way t test (E, F, I, and K), Kolmogorov-Smirnov test (G).

See also Figure S5.

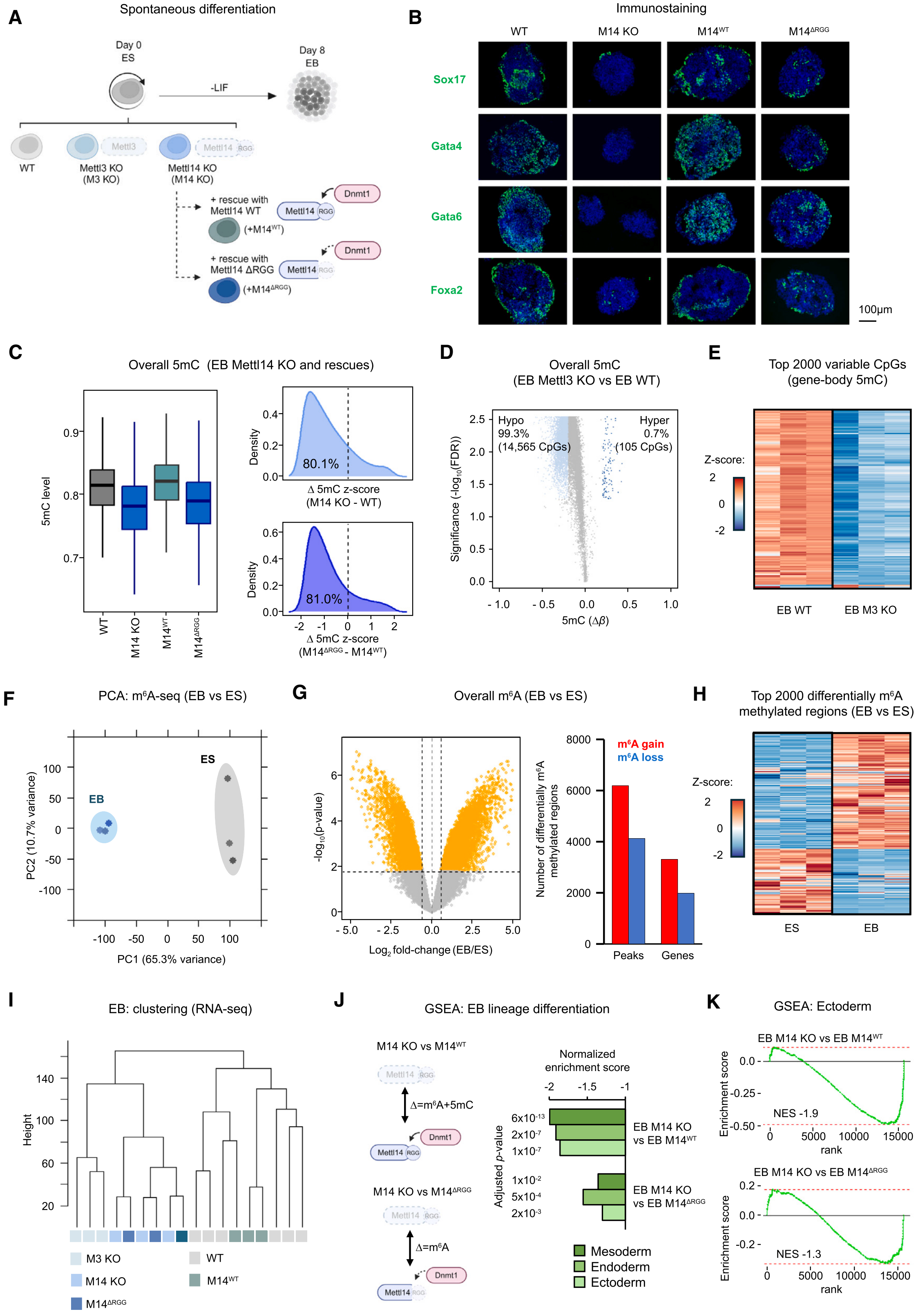

(legend on next page)

5mC and m^{6}A regulate gene expression through transcriptional and post-transcriptional effects, with substantial implications for dynamic gene regulation during peri-implantation development.

5mC and m^{6}A are both required for ES-to-EB differentiation

Given the effects of 5mC and m^{6}A in regulating gene expression during early embryonic development (Figure 5), we explored the biological functions of Mettl3 and Mettl14 in this context. First, we performed spontaneous ES differentiation to EBs using WT, Mettl3 KO, and Mettl14 KO ESCs. Furthermore, to investigate the role of Dnmt1 recruitment by the Mettl14 RGG domain (cf. Figure 1), we performed rescue experiments with either Mettl14^{WT} (rescuing both 5mC and m^{6}A) or Mettl14$^{\Delta RGG}$ (rescuing only m^{6}A) (Figures 6A and S6A). As previously reported,[23,24] Mettl3 KO ESCs displayed impaired differentiation, with higher expression of pluripotency genes and lower expression of differentiation markers (Figure S6B). In line with this, Mettl14 KO produced smaller EBs with reduced expression of differentiation markers (Figures 6B and S6C). Strikingly, only Mettl14^{WT} could fully rescue the normal EB phenotype. Mettl14$^{\Delta RGG}$ expression resulted in an intermediate phenotype (Figures 6B and S6C). Together, these observations indicate that Mettl3-Mettl14 contributes to EB differentiation via both m^{6}A and Dnmt1-deposited 5mC.

Delving deeper into EB differentiation, we examined the putative involvement of Mettl3-Mettl14-mediated 5mC deposition. In line with Mettl3 KO (Figures 4A–4C), we found Mettl14 KO to cause global DNA hypomethylation in both ESCs and EBs (Figures 6C and S6D), without affecting DNA methyltransferase expression (Figures S6E and S6F). Importantly, DNA methylation was rescued by expression of Mettl14^{WT}, but not of Mettl14$^{\Delta RGG}$ (Figures 6C and S6D). This highlights the critical role of the Mettl14-Dnmt1 interaction. Consistent with these findings, Mettl3-depleted EBs also displayed reduced global levels of DNA methylation (Figures 6D and S6G), with many hypomethylated sites in gene-bodies (Figure 6E). Considering the known increase in 5mC during WT ES differentiation (Figure S6G; Kalkan et al.,[53] Smith,[67] and Suelves et al.[68]), its impairment upon Mettl3 or Mettl14 depletion or removal of the Mettl14 RGG domain (Figures 6C–6E and S6G) suggests that the Mettl3-Mettl14-Dnmt1 axis contributes significantly to EB formation.

We then investigated m^{6}A deposition in differentiating ESCs. Transcriptome-wide mapping of RNA methylation revealed that ESCs and EBs have distinct m^{6}A profiles (Figure 6F), with both gain and loss of m^{6}A upon exit from pluripotency (Figures 6G, 6H, and S6H).

Since both marks are regulated during ESC differentiation, we performed RNA-seq and evaluated their separate and combined effects on expression of differentiation-related genes by comparing Mettl14 KO cells rescued by Mettl14$^{\Delta RGG}$ (rescuing only m^{6}A) vs. Mettl14^{WT} (rescuing both 5mC and m^{6}A). Hierarchical clustering revealed distinct patterns, with Mettl3 KO and Mettl14 KO EBs clustering with Mettl14$^{\Delta RGG}$-rescued EBs, possibly because of their respective defects in differentiation (Figure 6I). Focusing on EB lineage differentiation genes, gene set enrichment analysis (GSEA) confirmed only partial phenotypic rescue in Mettl14 KO cells by Mettl14$^{\Delta RGG}$, as compared with Mettl14^{WT} (Figures 6J-6K and S6I). Overall, these data underscore the crucial impact of the interaction between Mettl3-Mettl14 and Dnmt1 during ES-to-EB differentiation and emphasize that both 5mC and m^{6}A are required for this process.

The dynamics of 5mC and m^{6}A regulate key genes during ES-to-EB differentiation

Following our finding that Mettl3-Mettl14-dependent 5mC and m^{6}A both regulate gene expression and ES-to-EB differentiation, we aimed to identify key genes whose expression is controlled by both marks during ESC differentiation. We applied three criteria to pinpoint such targets in ESCs: (1) putative destabilization by m^{6}A (assessed by upregulation upon Mettl3 inhibition), (2) 5mC-promoted transcription (evidenced by lower expression upon Mettl3 KO vs. Mettl3 inhibition), and (3) the presence of both marks (Figure S7A). We thus identified 1,732 genes, hereafter referred to as "candidate genes" (Figure 7A). Importantly, the observed upregulation upon Mettl3 inhibition was not attributable to transcriptional effects, which confirms its post-transcriptional nature (Figure 7B).

Gene ontology analysis revealed many candidate genes to be involved in peri-implantation development (Figure S7B). During the ES-to-EB transition, candidate genes exhibited global upregulation in WT cells, but not upon Mettl3 KO (Figures 7C and 7D). As downregulation upon Mettl3 KO was observed in both ESCs and EBs, low expression cannot be attributed solely to defective EB differentiation (Figure 7C). We thus hypothesized that altered

Figure 6. 5mC and m^{6}A are both required during ES-to-EB differentiation

(A) Schematic model of ES-to-EB differentiation upon LIF removal, with all ESC lines used.

(B) Immunostaining of differentiation markers (Sox17, Gata4, Gata6, Foxa2) indicates that impaired EB formation in Mettl14 KO cells is fully rescued by expression of Mettl14^{WT} but only partially by Mettl14$^{\Delta RGG}$ expression. Scale bars, 100 μm.

(C) Mettl14 KO reduces 5mC levels in EBs, and these are rescued by expression of Mettl14^{WT}, but not Mettl14$^{\Delta RGG}$ ($n = 3$).

(D and E) Altered 5mC levels in Mettl3 KO EBs (D), with hypo- and hypermethylated CpGs in light and dark blue (corrected p value < 0.05 and $\Delta\beta > 0.2$), and heatmap of the top 2,000 most variable intragenic CpGs (E).

(F) PCA plot for all m^{6}A peaks found by m^{6}A-seq, showing that EBs and ESCs have distinct m^{6}A profiles ($n = 3$).

(G) Changes in m^{6}A between WT EBs and ESCs, with significant changes highlighted in orange (left, fold-change > 1.5 and corrected p value < 0.05) and number of significant peaks/genes (right).

(H) Heatmap of the top 2,000 most variable m^{6}A regions during the ESC-to-EB transition.

(I) Hierarchical clustering showing that EBs lacking Mettl3 or Mettl14 cluster with Mettl14$^{\Delta RGG}$-rescued EBs, from RNA-seq ($n = 3$).

(J and K) Comparing Mettl14 KO with Mettl14^{WT} and Mettl14$^{\Delta RGG}$ allows to assess the effects of reducing both 5mC and m^{6}A vs. m^{6}A alone in EBs. Gene set enrichment analysis (GSEA) of gene expression indicates that Mettl14 KO strongly impairs differentiation, with Mettl14$^{\Delta RGG}$ showing an intermediate phenotype. See also Figure S6.

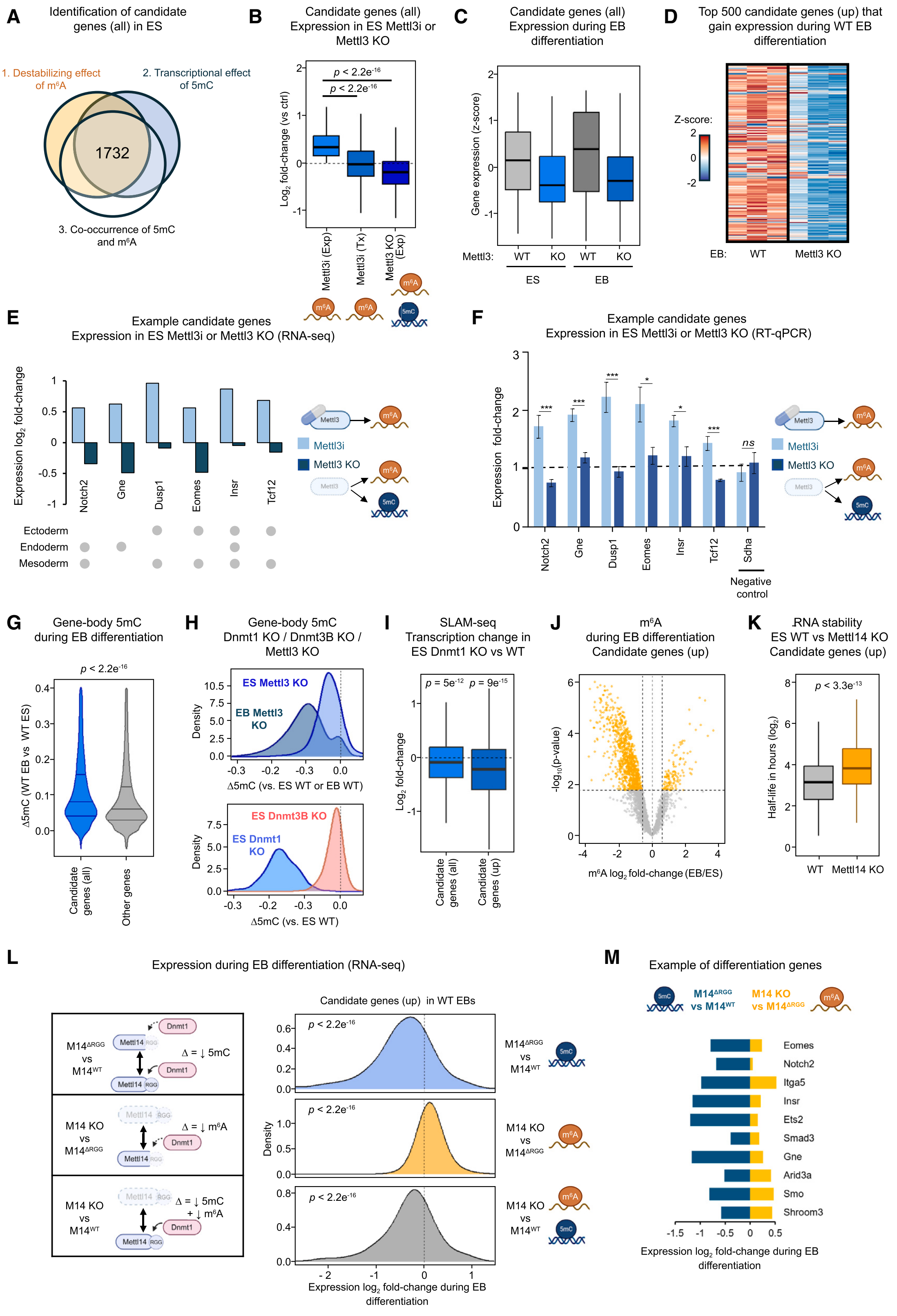

(legend on next page)

gene expression patterns may instead be attributable to 5mC and m^6A effects.

Notable examples of candidate genes involved in differentiation include Notch2,[69] Eomes,[70] Insr,[71] and Smad3[72] (Figures 7E, 7F and S7C). As expected, Mettl3 inhibition resulted in increased expression in ESCs, whereas Mettl3 KO caused lower expression than Mettl3 inhibition, suggesting a repressive role for m^6A and a permissive role for 5mC in regulating gene expression (Figures 7E, 7F, and S7C). Therefore, we next examined the function of each mark. DNA methylation is known to increase in differentiating ESCs,[53,67,68] but candidate genes exhibited even higher levels of gene-body methylation than other genes (Figures 7G and S7D). Importantly, we found intragenic 5mC to be mediated by the Mettl3-Mettl14-Dnmt1 axis, not Dnmt3b (Figures 7H and S7E). Furthermore, SLAM-seq analysis revealed transcription of candidate genes, especially those induced during WT EB formation, to be reduced following Dnmt1 KO (Figures 7I and S7F). These data suggest that gene-body methylation following Dnmt1 recruitment by Mettl3-Mettl14 promotes transcription of key genes in differentiating ESCs. We next analyzed dynamic changes in m^6A during EB differentiation. Overall, candidate genes displayed both gain and loss of m^6A upon exit from pluripotency (Figure S7G), but genes induced during differentiation appeared strongly biased toward reduced m^6A (Figures 7J, S7G, and S7H). Examining the half-lives of the corresponding transcripts in Mettl14-depleted ESCs, we observed a significant increase in their stability (Figures 7K and S7I). By contrast, candidate genes with increased m^6A during differentiation were not upregulated (Figure S7H). This suggests that m^6A can actively prevent the expression of such genes. Thus, while loss of m^6A during differentiation allows upregulation of the corresponding candidate genes, gain of m^6A can inhibit their expression. This nuanced regulatory mechanism supports the transition from pluripotency to differentiation.

To validate our model, we investigated the subset of candidate genes expected to be upregulated during EB formation (as defined in Figure 7D). Mettl14$^{\Delta RGG}$-rescued EBs showed reduced induction of these genes as compared with WT EBs, a defect attributable to impaired Dnmt1 recruitment resulting in reduced intragenic 5mC (Figures 7L and S7E). By contrast, comparing Mettl14 KO and Mettl14$^{\Delta RGG}$ cells suggested that reduced m^6A levels facilitate expression of the same genes. Lastly, comparing Mettl14 KO with WT EBs highlighted that the combined loss of 5mC and m^6A resulted in reduced expression of these genes. Thus, whereas 5mC and m^6A display opposite effects, the influence of 5mC prevails at genes expected to be upregulated during differentiation (Figure 7L). We illustrate this intricate regulation of gene expression by examining key genes involved in EB formation, including Eomes and Notch2 (Figure 7M).

In conclusion, our findings support a dynamic model wherein the balance between gene-body DNA methylation and RNA methylation, both mediated by Mettl3-Mettl14, shifts during exit from pluripotency. In particular, upregulation of well-known differentiation genes (e.g., Eomes, Notch2, Smad3) is made possible by a prominent increase in 5mC and decrease in m^6A (Figure S7J).

DISCUSSION

Our findings reveal an additional string to the already impressive bow of m^6A and its writer complex METTL3-METTL14. Beyond the roles of these players in controlling transcript processing and beyond their chromatin-state-regulating effects on histones, our data reveal that the METTL3-METTL14 complex is also involved in mediating DNA intragenic CpG methylation. It thus promotes both a transcriptional epigenetic effect and a post-transcriptional epitranscriptomic effect, which combine to fine-tune gene expression.

Our model includes two "paths," both beginning with METTL3-METTL14 (Figure S7J). The first is a mechanism of gene-body DNA methylation: chromatin-bound METTL3-METTL14 can recruit the DNA methyltransferase DNMT1 to chromatin, thus favoring gene-body 5mC deposition. In mammals, 60%–80% of CpG sites are methylated, with intragenic regions being more methylated than intergenic regions.[11,73] Previous studies have demonstrated (1) reliance of gene-body methylation on epigenetic interplay between the H3K36me3 histone modification and DNMT3B[14,15,74] and (2) H3K36me3-mediated recruitment of METTL14 to chromatin.[33] By contrast, METTL3-METTL14-dependent gene-body methylation in the here-identified gene set requires neither H3K36me3 nor DNMT3B.

Figure 7. Dynamic, coordinated adjustments of 5mC and m^6A fine-tune expression of key genes in differentiating ESCs

(A and B) Identification of 1,732 candidate genes (see Figure S7A and STAR Methods) and changes in expression upon Mettl3 inhibition (Exp: steady-state, Tx: nascent transcription, by SLAM-seq) or knockout (by RNA-seq).

(C) Expression of candidate genes in ESCs and EBs in WT and Mettl3 KO conditions.

(D) Heatmap showing that candidate genes upregulated in EBs (top 500 by EB/ES fold-change in WT cells, referred to as "up" candidates) show impaired expression in Mettl3 KO EBs.

(E and F) Divergent regulation of differentiation-involved candidate genes following Mettl3 inhibition or Mettl3 KO in ESCs by RNA-seq (E) and validation by RT-qPCR (F, $n = 6$).

(G) Candidate genes reach higher gene-body 5mC levels than other genes during EB differentiation.

(H) Gene-body methylation of candidate genes depends on Mettl3 and Dnmt1.

(I) Dnmt1 KO reduces nascent transcription of candidate genes, especially for genes that are upregulated in WT EBs ("up," as defined in Figure 7D).

(J) "Up" candidate genes display a global loss of m^6A during differentiation, with significant peaks highlighted in orange (fold-change > 1.5 and corrected p value < 0.05).

(K) "Up" candidate genes display increased transcript half-lives in Mettl14 KO ESCs.

(L and M) Comparing Mettl14 KO, Mettl14^{WT}, and Mettl14$^{\Delta RGG}$ conditions reveals the effects of reducing 5mC alone, m^6A alone, or both marks in EBs. "Up" candidate genes display opposite effects for 5mC and m^6A, with the influence of 5mC prevailing during differentiation.

Data as mean ± SD (F). p values by two-way t test (B, F, G, and K), one-sample t test (I and L).

See also Figure S7.

Only three studies, to date, have hinted at a link between m^{6}A and DNA methylation.[31,40,41] The work of Deng et al. (performed on HEK293T and ESCC [esophageal squamous cell carcinoma] cells) differs from ours (performed on HeLa and ES cells) in that it found METTL3 depletion to induce a higher level of 5mC. As regulation of DNA methylation is highly cell-context dependent,[75–77] it is noteworthy that Xu et al. made observations similar to ours in ESCs. More fundamental is the difference between the mechanisms of both Deng et al. and Sun et al., based on impaired hydroxymethylation due to a defect in Tet1 recruitment via m^{6}A readers, and ours, which relies neither on m^{6}A readers nor on Tet1 as 5mC demethylase.

The "second path" of our model concerns the well-known role of the METTL3-METTL14 complex as m^{6}A writer. Although this catalytic activity is not required for recruitment of DNMT1 and subsequent DNA methylation, the active m^{6}A writer complex intervenes in the second path of our model, as evidenced by co-occurring gene-body 5mC and m^{6}A on the corresponding transcript. Importantly, and despite not being involved in the "first path," m^{6}A plays a major role through the second path in the case of 5mC-m^{6}A target genes: the two marks co-contribute, in opposite ways, to regulating expression of these genes, gene-body 5mC by enhancing their transcription and m^{6}A by destabilizing their RNAs. The result is a dynamic balance between transcriptional activity and RNA stability, ensuring subtle control of gene expression.

The link evidenced here between epigenetics and epitranscriptomics is part of a larger gene-expression-regulating network. On the one hand, RNA methylation affects steady-state RNA levels through post-transcriptional control of transcript stability.[27,52,59,78,79] The transcript-destabilizing effect of m^{6}A is key to maintaining proper gene expression dynamics in cells.[23,80] On the other hand, gene-body 5mC upregulates transcription. The resulting balancing act brings to mind established interactions between activating and repressive histone marks, such as the intricate interplay observed in bivalent domains, whereby H3K4me3 and H3K27me3 coordinate nuanced gene expression regulation.[81]

Here we pinpoint an important area where our findings are biologically relevant: embryonic differentiation, showing that two regulating paths of our model are required for proper differentiation (Figures 6 and 7). Consistent with previous studies,[23,24] exit from pluripotency is accompanied by repression of naive pluripotency gene expression through m^{6}A-promoted RNA decay, and depletion of Mettl3 or Mettl14 results in differentiation defects. We have further established, by deleting the Mettl14-RGG domain, that recruitment of Dnmt1 by Mettl3-Mettl14 is crucial for efficient induction of EB formation. While a few studies have provided hints in this direction,[17,53] we now establish a pivotal role of gene-body methylation in early embryonic development. Noteworthy examples of key genes identified here as being regulated by both marks are Eomes, essential for specification of multiple lineages,[70] Smad3, involved in mesoderm and definitive endoderm cell fate,[72] and Notch2, which orchestrates the formation and patterning of tissues and organs across various stages of embryogenesis.[69] Thus, genes whose spatiotemporal expression ensures correct cell fate decisions during mammalian embryonic development[72] are tightly regulated by 5mC and m^{6}A in differentiating ESCs.

In a manner reminiscent of bivalent domains, the presence of both marks at crucial differentiation-related genes suggests that these genes are kept under control in pluripotent cells but remain poised for rapid expression upon differentiation.[81] During EB formation, accordingly, a local shift in the balance between 5mC and m^{6}A levels (the former increasing, the latter decreasing) facilitates activation of those genes. By contrast, it is worth mentioning that a subset of 5mC-m^{6}A genes displays gain of m^{6}A during differentiation, opposing the effects of gene-body 5mC and repressing their expression. This gain of m^{6}A tallies with the well-documented role of the mark in regulating pluripotency-related genes. Taken together, this nuanced regulation, supported by localized changes in m^{6}A distribution, underlies both repression of pluripotency and promotion of EB formation. What are the mechanisms driving gain and loss of the mark? Differential recruitment and activity of the m^{6}A writer complex have notably been linked to interactions with transcription factors, RNA-binding proteins, and the chromatin environment.[29,30,33,82–84] How external cues and intrinsic signaling mechanisms interact to influence local m^{6}A dynamics during ESC differentiation warrants future investigation.

The connections identified here between an RNA-modifying complex, a DNA methyltransferase, and the corresponding marks are reminiscent of the tight, critical interplay between histone-modifying enzymes and DNMTs or histone enzymes and m^{6}A.[1,85] In this exciting field, our findings have the potential to spark an explosion of discovery and perhaps to close a regulatory loop between histone modifiers, DNMTs, and RNA modifiers. A picture is forming in which these players work hand-in-hand within intimately connected epigenetic/epitranscriptomic programs, integrating gene regulation networks within the cell.

In conclusion, our results (1) identify a distinct set of genes depending on METTL3-METTL14-recruited DNMT1 for gene-body methylation, (2) demonstrate fine-tuning of gene expression regulation through the combined and opposite effects of 5mC and m^{6}A, and (3) show a role for this fine-tuning in ES-to-EB differentiation. Importantly, the balance between these contrasting effects shifts during exit from pluripotency, resulting in enhanced expression of key differentiation genes. By shedding another light on the links between epigenetics and epitranscriptomics as they relate to gene expression, our findings open prospects for future breakthroughs, notably in developmental biology and potentially in disease.

Limitations of the study

In addition to the open questions for future work noted in the discussion, the study has some limitations. First, this study focuses on the regulation of gene-body DNA methylation, gene-bodies being where we observed most of the hypomethylation following METTL3 depletion. However, hypomethylated sites also occur outside gene-bodies. Thus, it is plausible that METTL3-METTL14 may facilitate DNMT1 recruitment to other genomic regions, including promoters, enhancers, and repetitive elements. Investigating whether the here-identified mechanism is involved in regulating DNA methylation across various genomic regions would be interesting.

Second, spontaneous EB differentiation is inherently heterogeneous, with a diverse array of cell types and developmental stages observed. While examining inter-cell heterogeneity in relation to 5mC and m^{6}A regulation within distinct lineages would be an enriching endeavor, our analyses were limited by the substantial amounts of material required for the techniques used. Consequently, our findings might not fully capture the nuanced differences between individual cells, especially across different developmental lineages, within differentiating EBs. Such cellular heterogeneity warrants investigation with single-cell technologies.

RESOURCE AVAILABILITY

Lead contact

Further information and requests for resources and reagents should be directed to and will be fulfilled by the lead contact, François Fuks (francois.fuks@ulb.be).

Materials availability

Further information and requests for resources and reagents should be directed to and will be fulfilled by the lead contact.

Data and code availability

- Infinium MethylationEPIC array, Infinium MouseMethylation array, m^{6}A-seq, Polysome-seq, ChIP-seq, PRO-seq, SLAM-seq, and RNA-seq raw data have been deposited in the Gene Expression Omnibus (GEO) repository and are publicly available as of the date of publication. Accession numbers are listed in the key resources table. This paper also analyzes existing, publicly available data. The accession numbers of datasets are listed in the key resources table.
- This paper does not report original code, but the available software packages used for analysis are described in the STAR Methods section and key resources table.
- Any additional information required to reanalyze the data reported in this paper is available from the lead contact upon reasonable request.

ACKNOWLEDGMENTS

HEK293^{5XUAS} cells, mouse ESC J1 WT/Mettl3 KO, WT/Dnmt1 KO, and E14TG2a WT/Mettl14 KO were kindly provided by the laboratories of Pr. Bastian Stielow (Germany), Pr. Howard Y. Chang (USA), Pr. Fabio Spada (Germany), and Pr. Laixin Xia (China), respectively. G.Q., A.L.G., M.B., A.P., I.P., F. Murisier, B.H., J.M., L.V.d.L., P.K., G.D., J.J., and E. Collignon were supported by the Belgian FRS-FNRS, FRIA, or Télévie. Q.G and A.L.G. were supported by the Fondation Rose et Jean Hoguet and the Fondation Jaumotte-Demoulin and Fonds David and Alice Van Buuren. F.F. is a ULB professor. R.D. is a ULB lecturer. This work was partially supported by R01GM141349 and R01GM146409 from the National Institute of General Medical Sciences to L.M. We thank the Sylvester Comprehensive Cancer Center Onco-Genomics Core Facility for high-throughput sequencing. This work was supported by funding from the University of Miami Miller School of Medicine, Sylvester Comprehensive Cancer Center, and grants R01GM078455 from the National Institute of Health to R.S. Research reported in this publication was supported by the National Cancer Institute of the National Institutes of Health under award number P30CA240139. The content is solely the responsibility of the authors and does not necessarily represent the official views of the National Institutes of Health. This work was partially supported by the Welch Foundation (AQ-2101-20220331) and the National Institute of Allergy and Infectious Diseases (R01AI161363) to Y.K.G. F.F.'s lab was funded by grants from the FNRS and Télévie, the "Action de Recherche Concertée" (ARC) (AUWB-2018-2023 ULB-No 7), a Walloon Region grant (Win2Wal), FNRS Welbio grants (FNRS-WELBIO-CR-2017A-04 and FNRS-WELBIO-CR-2019A-04R), the FWO and FNRS under the Excellence of Science (EOS O.0020.22/RG3483) programme, the ULB Foundation, the Belgian Foundation against Cancer (FCC 2016-086 FAF-F/2016/872), and H2020-MSCA-ITN ROPES.

AUTHOR CONTRIBUTIONS

Investigation, G.Q., A.L.G., I.P., L.G.-M., Q.G., P.K.R.C., E. Calonne, B.H., C.H., A.H., P.P., F. Mies, J.M., L.V.d.L., R.S., A.K., A.M., J.L., M.P., A.B., P.-O.E., and E.A.C.; formal analysis, G.Q., A.L.G., M.B., F. Murisier, R.L.B., P.K.R.C., G.D., P.K., and E. Collignon; visualization, G.Q., M.B., A.P., F. Murisier, and E. Collignon; writing – review & editing, G.Q., A.P., E. Collignon, and F.F.; all authors discussed the results and commented on the manuscript; project administration, I.P., Y.K.G., P.K.R.C., K.M.R., C.G., D.L.D., S.P., R.S., Y.D., L.M., J.J., R.D., E. Collignon, and F.F.; funding acquisition, R.D. and F.F.; conceptualization and supervision, F.F.

DECLARATION OF INTERESTS

F.F. is a co-founder of Epics Therapeutics (Gosselies, Belgium).

STAR★METHODS

Detailed methods are provided in the online version of this paper and include the following:

- KEY RESOURCES TABLE
- EXPERIMENTAL MODEL AND STUDY PARTICIPANT DETAILS
  - Cell lines
- METHOD DETAILS
  - Manipulations on cultured cells
  - *In vitro* differentiation of ESCs
  - Cell line generation
  - Immunofluorescence
  - NanoBRET
  - RNA extraction and RT-qPCR
  - Western blotting
  - Recombinant protein purification
  - GST pull-down assays
  - Co-immunoprecipitation with purified recombinant proteins
  - Co-immunoprecipitation assays on cell lysates
  - GAL4-5XUAS recruitment assay
  - Dot blotting for 5mC and m^{6}A quantification
  - Site-specific m^{6}A demethylation
  - Bisulfite pyrosequencing
  - RNA-seq
  - m^{6}A Sequencing
  - Infinium Methylation array
  - SLAM-seq
  - RNA stability assay by actinomycin D treatment
  - Polysome profiling
  - Precision run-on and sequencing (PRO-seq)
- QUANTIFICATION AND STATISTICAL ANALYSIS
  - Sequencing & array data analysis
  - Data integration

SUPPLEMENTAL INFORMATION

Supplemental information can be found online at https://doi.org/10.1016/j.cell.2024.12.009.

Received: April 11, 2023
Revised: October 29, 2024
Accepted: December 9, 2024
Published: January 17, 2025

REFERENCES

1. Du, J., Johnson, L.M., Jacobsen, S.E., and Patel, D.J. (2015). DNA methylation pathways and their crosstalk with histone methylation. Nat. Rev. Mol. Cell Biol. *16*, 519–532. https://doi.org/10.1038/nrm4043.

2. Li, Y., Chen, X., and Lu, C. (2021). The interplay between DNA and histone methylation: molecular mechanisms and disease implications. EMBO Rep. *22*, e51803. https://doi.org/10.15252/embr.202051803.
3. Lee, J.S., Smith, E., and Shilatifard, A. (2010). The Language of Histone Crosstalk. Cell *142*, 682–685. https://doi.org/10.1016/J.CELL.2010.08.011.
4. Lyko, F. (2018). The DNA methyltransferase family: a versatile toolkit for epigenetic regulation. Nat. Rev. Genet. *19*, 81–92. https://doi.org/10.1038/nrg.2017.80.
5. Bestor, T.H. (2000). The DNA methyltransferases of mammals. Hum. Mol. Genet. *9*, 2395–2402. https://doi.org/10.1093/HMG/9.16.2395.
6. Li, E., Bestor, T.H., and Jaenisch, R. (1992). Targeted mutation of the DNA methyltransferase gene results in embryonic lethality. Cell *69*, 915–926. https://doi.org/10.1016/0092-8674(92)90611-F.
7. Mattei, A.L., Bailly, N., and Meissner, A. (2022). DNA methylation: a historical perspective. Trends Genet. *38*, 676–707. https://doi.org/10.1016/j.tig.2022.03.010.
8. Ball, M.P., Li, J.B., Gao, Y., Lee, J.-H., LeProust, E.M., Park, I.-H., Xie, B., Daley, G.Q., and Church, G.M. (2009). Targeted and genome-scale strategies reveal gene-body methylation signatures in human cells. Nat. Biotechnol. *27*, 361–368. https://doi.org/10.1038/nbt.1533.
9. Laurent, L., Wong, E., Li, G., Huynh, T., Tsirigos, A., Ong, C.T., Low, H.M., Kin Sung, K.W., Rigoutsos, I., Loring, J., et al. (2010). Dynamic changes in the human methylome during differentiation. Genome Res. *20*, 320–331. https://doi.org/10.1101/gr.101907.109.
10. Kulis, M., Heath, S., Bibikova, M., Queirós, A.C., Navarro, A., Clot, G., Martínez-Trillos, A., Castellano, G., Brun-Heath, I., Pinyol, M., et al. (2012). Epigenomic analysis detects widespread gene-body DNA hypomethylation in chronic lymphocytic leukemia. Nat. Genet. *44*, 1236–1242. https://doi.org/10.1038/ng.2443.
11. Lister, R., Pelizzola, M., Dowen, R.H., Hawkins, R.D., Hon, G., Tonti-Filippini, J., Nery, J.R., Lee, L., Ye, Z., Ngo, Q.-M., et al. (2009). Human DNA methylomes at base resolution show widespread epigenomic differences. Nature *462*, 315–322. https://doi.org/10.1038/nature08514.
12. Ooi, S.K.T., Qiu, C., Bernstein, E., Li, K., Jia, D., Yang, Z., Erdjument-Bromage, H., Tempst, P., Lin, S.P., Allis, C.D., et al. (2007). DNMT3L connects unmethylated lysine 4 of histone H3 to de novo methylation of DNA. Nature *448*, 714–717. https://doi.org/10.1038/NATURE05987.
13. Weinberg, D.N., Papillon-Cavanagh, S., Chen, H., Yue, Y., Chen, X., Rajagopalan, K.N., Horth, C., McGuire, J.T., Xu, X., Nikbakht, H., et al. (2019). The histone mark H3K36me2 recruits DNMT3A and shapes the intergenic DNA methylation landscape. Nature *573*, 281–286. https://doi.org/10.1038/s41586-019-1534-3.
14. Baubec, T., Colombo, D.F., Wirbelauer, C., Schmidt, J., Burger, L., Krebs, A.R., Akalin, A., and Schübeler, D. (2015). Genomic profiling of DNA methyltransferases reveals a role for DNMT3B in genic methylation. Nature *520*, 243–247. https://doi.org/10.1038/nature14176.
15. Neri, F., Rapelli, S., Krepelova, A., Incarnato, D., Parlato, C., Basile, G., Maldotti, M., Anselmi, F., and Oliviero, S. (2017). Intragenic DNA methylation prevents spurious transcription initiation. Nature *543*, 72–77. https://doi.org/10.1038/nature21373.
16. Smith, Z.D., and Meissner, A. (2013). DNA methylation: roles in mammalian development. Nat. Rev. Genet. *14*, 204–220. https://doi.org/10.1038/nrg3354.
17. Wu, H., Coskun, V., Tao, J., Xie, W., Ge, W., Yoshikawa, K., Li, E., Zhang, Y., and Sun, Y.E. (2010). Dnmt3a-dependent nonpromoter DNA methylation facilitates transcription of neurogenic genes. Science *329*, 444–448. https://doi.org/10.1126/science.1190485.
18. Dominissini, D., Moshitch-Moshkovitz, S., Schwartz, S., Salmon-Divon, M., Ungar, L., Osenberg, S., Cesarkas, K., Jacob-Hirsch, J., Amariglio, N., Kupiec, M., et al. (2012). Topology of the human and mouse m6A RNA methylomes revealed by m6A-seq. Nature *485*, 201–206. https://doi.org/10.1038/nature11112.
19. Meyer, K.D., Saletore, Y., Zumbo, P., Elemento, O., Mason, C.E., and Jaffrey, S.R. (2012). Comprehensive analysis of mRNA methylation reveals enrichment in 3′ UTRs and near stop codons. Cell *149*, 1635–1646. https://doi.org/10.1016/j.cell.2012.05.003.
20. Lee, M., Kim, B., and Kim, V.N. (2014). Emerging roles of RNA modification: m(6)A and U-tail. Cell *158*, 980–987. https://doi.org/10.1016/j.cell.2014.08.005.
21. Roundtree, I.A., Evans, M.E., Pan, T., and He, C. (2017). Dynamic RNA Modifications in Gene Expression Regulation. Cell *169*, 1187–1200. https://doi.org/10.1016/j.cell.2017.05.045.
22. Wang, Y., Li, Y., Toth, J.I., Petroski, M.D., Zhang, Z., and Zhao, J.C. (2014). N6-methyladenosine modification destabilizes developmental regulators in embryonic stem cells. Nat. Cell Biol. *16*, 191–198. https://doi.org/10.1038/ncb2902.
23. Geula, S., Moshitch-Moshkovitz, S., Dominissini, D., Mansour, A.A., Kol, N., Salmon-Divon, M., Hershkovitz, V., Peer, E., Mor, N., Manor, Y.S., et al. (2015). Stem cells. m6A mRNA methylation facilitates resolution of naïve pluripotency toward differentiation. Science *347*, 1002–1006. https://doi.org/10.1126/science.1261417.
24. Batista, P.J., Molinie, B., Wang, J., Qu, K., Zhang, J., Li, L., Bouley, D.M., Lujan, E., Haddad, B., Daneshvar, K., et al. (2014). m(6)A RNA modification controls cell fate transition in mammalian embryonic stem cells. Cell Stem Cell *15*, 707–719. https://doi.org/10.1016/j.stem.2014.09.019.
25. Knuckles, P., Carl, S.H., Musheev, M., Niehrs, C., Wenger, A., and Bühler, M. (2017). RNA fate determination through cotranscriptional adenosine methylation and microprocessor binding. Nat. Struct. Mol. Biol. *24*, 561–569. https://doi.org/10.1038/nsmb.3419.
26. Yang, Y., Hsu, P.J., Chen, Y.-S., and Yang, Y.-G. (2018). Dynamic transcriptomic m6A decoration: writers, erasers, readers and functions in RNA metabolism. Cell Res. *28*, 616–624. https://doi.org/10.1038/s41422-018-0040-8.
27. Zaccara, S., Ries, R.J., and Jaffrey, S.R. (2019). Reading, writing and erasing mRNA methylation. Nat. Rev. Mol. Cell Biol. *20*, 608–624. https://doi.org/10.1038/s41580-019-0168-5.
28. Liu, J., Yue, Y., Han, D., Wang, X., Fu, Y., Zhang, L., Jia, G., Yu, M., Lu, Z., Deng, X., et al. (2014). A METTL3-METTL14 complex mediates mammalian nuclear RNA N6-adenosine methylation. Nat. Chem. Biol. *10*, 93–95. https://doi.org/10.1038/nchembio.1432.
29. Barbieri, I., Tzelepis, K., Pandolfini, L., Shi, J., Millán-Zambrano, G., Robson, S.C., Aspris, D., Migliori, V., Bannister, A.J., Han, N., et al. (2017). Promoter-bound METTL3 maintains myeloid leukaemia by m6A-dependent translation control. Nature *552*, 126–131. https://doi.org/10.1038/nature24678.
30. Liu, J., Dou, X., Chen, C., Chen, C., Liu, C., Xu, M.M., Zhao, S., Shen, B., Gao, Y., Han, D., et al. (2020). N6-methyladenosine of chromosome-associated regulatory RNA regulates chromatin state and transcription. Science *367*, 580–586. https://doi.org/10.1126/science.aay6018.
31. Xu, W., Li, J., He, C., Wen, J., Ma, H., Rong, B., Diao, J., Wang, L., Wang, J., Wu, F., et al. (2021). METTL3 regulates heterochromatin in mouse embryonic stem cells. Nature *591*, 317–321. https://doi.org/10.1038/s41586-021-03210-1.
32. Li, Y., Xia, L., Tan, K., Ye, X., Zuo, Z., Li, M., Xiao, R., Wang, Z., Liu, X., Deng, M., et al. (2020). N6-methyladenosine co-transcriptionally directs the demethylation of histone H3K9me2. Nat. Genet. *52*, 870–877. https://doi.org/10.1038/s41588-020-0677-3.
33. Huang, H., Weng, H., Zhou, K., Wu, T., Zhao, B.S., Sun, M., Chen, Z., Deng, X., Xiao, G., Auer, F., et al. (2019). Histone H3 trimethylation at lysine 36 guides m6A RNA modification co-transcriptionally. Nature *567*, 414–419. https://doi.org/10.1038/s41586-019-1016-7.
34. Dou, X., Xiao, Y., Shen, C., Wang, K., Wu, T., Liu, C., Li, Y., Yu, X., Liu, J., Dai, Q., et al. (2023). RBFOX2 recognizes N6-methyladenosine to suppress transcription and block myeloid leukaemia differentiation. Nat. Cell Biol. *25*, 1359–1368. https://doi.org/10.1038/s41556-023-01213-w.

35. Mu, M., Li, X., Dong, L., Wang, J., Cai, Q., Hu, Y., Wang, D., Zhao, P., Zhang, L., Zhang, D., et al. (2023). METTL14 regulates chromatin bivalent domains in mouse embryonic stem cells. Cell Rep. *42*, 112650. https://doi.org/10.1016/j.celrep.2023.112650.

36. Dou, X., Huang, L., Xiao, Y., Liu, C., Li, Y., Zhang, X., Yu, L., Zhao, R., Yang, L., Chen, C., et al. (2023). METTL14 is a chromatin regulator independent of its RNA N6-methyladenosine methyltransferase activity. Protein Cell *14*, 683–697. https://doi.org/10.1093/procel/pwad009.

37. Lin, S., Choe, J., Du, P., Triboulet, R., and Gregory, R.I. (2016). The m(6)A Methyltransferase METTL3 Promotes Translation in Human Cancer Cells. Mol. Cell *62*, 335–345. https://doi.org/10.1016/j.molcel.2016.03.021.

38. Choe, J., Lin, S., Zhang, W., Liu, Q., Wang, L., Ramirez-Moya, J., Du, P., Kim, W., Tang, S., Sliz, P., et al. (2018). mRNA circularization by METTL3-eIF3h enhances translation and promotes oncogenesis. Nature *561*, 556–560. https://doi.org/10.1038/s41586-018-0538-8.

39. Liu, P., Li, F., Lin, J., Fukumoto, T., Nacarelli, T., Hao, X., Kossenkov, A.V., Simon, M.C., and Zhang, R. (2021). m6A-independent genome-wide METTL3 and METTL14 redistribution drives the senescence-associated secretory phenotype. Nat. Cell Biol. *23*, 355–365. https://doi.org/10.1038/s41556-021-00656-3.

40. Deng, S., Zhang, J., Su, J., Zuo, Z., Zeng, L., Liu, K., Zheng, Y., Huang, X., Bai, R., Zhuang, L., et al. (2022). RNA m6A regulates transcription via DNA demethylation and chromatin accessibility. Nat. Genet. *54*, 1427–1437. https://doi.org/10.1038/s41588-022-01173-1.

41. Sun, T., Xu, Y., Xiang, Y., Ou, J., Soderblom, E.J., and Diao, Y. (2023). Crosstalk between RNA m6A and DNA methylation regulates transposable element chromatin activation and cell fate in human pluripotent stem cells. Nat. Genet. *55*, 1324–1335. https://doi.org/10.1038/s41588-023-01452-5.

42. Leonhardt, H., Page, A.W., Weier, H.U., and Bestor, T.H. (1992). A targeting sequence directs DNA methyltransferase to sites of DNA replication in mammalian nuclei. Cell *71*, 865–873. https://doi.org/10.1016/0092-8674(92)90561-p.

43. Thandapani, P., O'Connor, T.R., Bailey, T.L., and Richard, S. (2013). Defining the RGG/RG motif. Mol. Cell *50*, 613–623. https://doi.org/10.1016/j.molcel.2013.05.021.

44. Yankova, E., Blackaby, W., Albertella, M., Rak, J., De Braekeleer, E., Tsagkogeorga, G., Pilka, E.S., Aspris, D., Leggate, D., Hendrick, A.G., et al. (2021). Small-molecule inhibition of METTL3 as a strategy against myeloid leukaemia. Nature *593*, 597–601. https://doi.org/10.1038/s41586-021-03536-w.

45. Huang, Y., Su, R., Sheng, Y., Dong, L., Dong, Z., Xu, H., Ni, T., Zhang, Z.S., Zhang, T., Li, C., et al. (2019). Small-Molecule Targeting of Oncogenic FTO Demethylase in Acute Myeloid Leukemia. Cancer Cell *35*, 677–691.e10. https://doi.org/10.1016/j.ccell.2019.03.006.

46. Xia, Z., Tang, M., Ma, J., Zhang, H., Gimple, R.C., Prager, B.C., Tang, H., Sun, C., Liu, F., Lin, P., et al. (2021). Epitranscriptomic editing of the RNA N6-methyladenosine modification by dCasRx conjugated methyltransferase and demethylase. Nucleic Acids Res. *49*, 7361–7374. https://doi.org/10.1093/nar/gkab517.

47. Dahlet, T., Argüeso Lleida, A., Al Adhami, H., Dumas, M., Bender, A., Ngondo, R.P., Tanguy, M., Vallet, J., Auclair, G., Bardet, A.F., et al. (2020). Genome-wide analysis in the mouse embryo reveals the importance of DNA methylation for transcription integrity. Nat. Commun. *11*, 3153. https://doi.org/10.1038/s41467-020-16919-w.

48. Scelfo, A., Barra, V., Abdennur, N., Spracklin, G., Busato, F., Salinas-Luypaert, C., Bonaiti, E., Velasco, G., Bonhomme, F., Chipont, A., et al. (2024). Tunable DNMT1 degradation reveals DNMT1/DNMT3B synergy in DNA methylation and genome organization. J. Cell Biol. *223*, e202307026. https://doi.org/10.1083/jcb.202307026.

49. Stankevičius, V., Gibas, P., Masiulionytė, B., Gasiulė, L., Masevičius, V., Klimašauskas, S., and Vilkaitis, G. (2022). Selective chemical tracking of Dnmt1 catalytic activity in live cells. Mol. Cell *82*, 1053–1065.e8. https://doi.org/10.1016/j.molcel.2022.02.008.

50. Yang, X., Han, H., De Carvalho, D.D., Lay, F.D., Jones, P.A., and Liang, G. (2014). Gene body methylation can alter gene expression and is a therapeutic target in cancer. Cancer Cell *26*, 577–590. https://doi.org/10.1016/j.ccr.2014.07.028.

51. Su, J., Huang, Y.-H., Cui, X., Wang, X., Zhang, X., Lei, Y., Xu, J., Lin, X., Chen, K., Lv, J., et al. (2018). Homeobox oncogene activation by pan-cancer DNA hypermethylation. Genome Biol. *19*, 108. https://doi.org/10.1186/s13059-018-1492-3.

52. Collignon, E., Cho, B., Furlan, G., Fothergill-Robinson, J., Martin, S.-B., McClymont, S.A., Ross, R.L., Limbach, P.A., and Ramalho-Santos, M. (2023). m6A RNA methylation orchestrates transcriptional dormancy during paused pluripotency. Nat. Cell Biol. *25*, 1279–1289. https://doi.org/10.1038/s41556-023-01212-x.

53. Kalkan, T., Olova, N., Roode, M., Mulas, C., Lee, H.J., Nett, I., Marks, H., Walker, R., Stunnenberg, H.G., Lilley, K.S., et al. (2017). Tracking the embryonic stem cell transition from ground state pluripotency. Development *144*, 1221–1234. https://doi.org/10.1242/dev.142711.

54. Zhang, Y., Xiang, Y., Yin, Q., Du, Z., Peng, X., Wang, Q., Fidalgo, M., Xia, W., Li, Y., Zhao, Z.-A., et al. (2018). Dynamic epigenomic landscapes during early lineage specification in mouse embryos. Nat. Genet. *50*, 96–105. https://doi.org/10.1038/s41588-017-0003-x.

55. Yue, F., Cheng, Y., Breschi, A., Vierstra, J., Wu, W., Ryba, T., Sandstrom, R., Ma, Z., Davis, C., Pope, B.D., et al. (2014). A comparative encyclopedia of DNA elements in the mouse genome. Nature *515*, 355–364. https://doi.org/10.1038/nature13992.

56. Maunakea, A.K., Nagarajan, R.P., Bilenky, M., Ballinger, T.J., D'Souza, C., Fouse, S.D., Johnson, B.E., Hong, C., Nielsen, C., Zhao, Y., et al. (2010). Conserved role of intragenic DNA methylation in regulating alternative promoters. Nature *466*, 253–257. https://doi.org/10.1038/nature09165.

57. Herzog, V.A., Reichholf, B., Neumann, T., Rescheneder, P., Bhat, P., Burkard, T.R., Wlotzka, W., von Haeseler, A., Zuber, J., and Ameres, S.L. (2017). Thiol-linked alkylation of RNA to assess expression dynamics. Nat. Methods *14*, 1198–1204. https://doi.org/10.1038/nmeth.4435.

58. Neumann, T., Herzog, V.A., Muhar, M., von Haeseler, A., Zuber, J., Ameres, S.L., and Rescheneder, P. (2019). Quantification of experimentally induced nucleotide conversions in high-throughput sequencing datasets. BMC Bioinformatics *20*, 258. https://doi.org/10.1186/s12859-019-2849-7.

59. Kim, Y.-K., Collignon, E., Martin, S.B., and Ramalho-Santos, M. (2024). Hypertranscription: the invisible hand in stem cell biology. Trends Genet. *40*, 1032–1046. https://doi.org/10.1016/j.tig.2024.08.005.

60. Varley, K.E., Gertz, J., Bowling, K.M., Parker, S.L., Reddy, T.E., Pauli-Behn, F., Cross, M.K., Williams, B.A., Stamatoyannopoulos, J.A., Crawford, G.E., et al. (2013). Dynamic DNA methylation across diverse human cell lines and tissues. Genome Res. *23*, 555–567. https://doi.org/10.1101/gr.147942.112.

61. Ke, S., Pandya-Jones, A., Saito, Y., Fak, J.J., Vågbø, C.B., Geula, S., Hanna, J.H., Black, D.L., Darnell, J.E., and Darnell, R.B. (2017). m6A mRNA modifications are deposited in nascent pre-mRNA and are not required for splicing but do specify cytoplasmic turnover. Genes Dev. *31*, 990–1006. https://doi.org/10.1101/gad.301036.117.

62. Hayashi, K., Ohta, H., Kurimoto, K., Aramaki, S., and Saitou, M. (2011). Reconstitution of the mouse germ cell specification pathway in culture by pluripotent stem cells. Cell *146*, 519–532. https://doi.org/10.1016/j.cell.2011.06.052.

63. Krishnakumar, R., Chen, A.F., Pantovich, M.G., Danial, M., Parchem, R.J., Labosky, P.A., and Blelloch, R. (2016). FOXD3 Regulates Pluripotent Stem Cell Potential by Simultaneously Initiating and Repressing Enhancer Activity. Cell Stem Cell *18*, 104–117. https://doi.org/10.1016/j.stem.2015.10.003.

64. Yang, P., Humphrey, S.J., Cinghu, S., Pathania, R., Oldfield, A.J., Kumar, D., Perera, D., Yang, J.Y.H., James, D.E., Mann, M., et al. (2019). Multi-omic Profiling Reveals Dynamics of the Phased Progression of Pluripotency. Cell Syst. *8*, 427–445.e10. https://doi.org/10.1016/j.cels.2019.03.012.

65. Cingaram, P.R., Beckedorff, F., Yue, J., Liu, F., Dos Santos, H.G., and Shiekhattar, R. (2024). Enhancing Transcriptome Mapping with Rapid PRO-seq Profiling of Nascent RNA. Preprint at bioRxiv. https://doi.org/10.1101/2024.05.08.593182.

66. Dasilva, L.F., Blumenthal, E., Beckedorff, F., Cingaram, P.R., Gomes dos Santos, H., Edupuganti, R.R., Zhang, A., Dokaneheifard, S., Aoi, Y., Yue, J., et al. (2021). Integrator enforces the fidelity of transcriptional termination at protein-coding genes. Sci. Adv. *7*, eabe3393. https://doi.org/10.1126/sciadv.abe3393.

67. Smith, A. (2017). Formative pluripotency: the executive phase in a developmental continuum. Development *144*, 365–373. https://doi.org/10.1242/dev.142679.

68. Suelves, M., Carrió, E., Núñez-Álvarez, Y., and Peinado, M.A. (2016). DNA methylation dynamics in cellular commitment and differentiation. Brief. Funct. Genomics *15*, 443–453. https://doi.org/10.1093/bfgp/elw017.

69. Djabrayan, N.J.-V., Dudley, N.R., Sommermann, E.M., and Rothman, J.H. (2012). Essential role for Notch signaling in restricting developmental plasticity. Genes Dev. *26*, 2386–2391. https://doi.org/10.1101/gad.199588.112.

70. Bisia, A.M., Costello, I., Xypolita, M.-E., Harland, L.T.G., Kurbel, P.J., Bikoff, E.K., and Robertson, E.J. (2023). A degron-based approach to manipulate Eomes functions in the context of the developing mouse embryo. Proc. Natl. Acad. Sci. USA *120*, e2311946120. https://doi.org/10.1073/pnas.2311946120.

71. Wang, K., Shen, H., Gan, P., Cavallero, S., Kumar, S.R., Lien, C.-L., and Sucov, H.M. (2019). Differential roles of insulin like growth factor 1 receptor and insulin receptor during embryonic heart development. BMC Dev. Biol. *19*, 5. https://doi.org/10.1186/s12861-019-0186-8.

72. Senft, A.D., Costello, I., King, H.W., Mould, A.W., Bikoff, E.K., and Robertson, E.J. (2018). Combinatorial Smad2/3 Activities Downstream of Nodal Signaling Maintain Embryonic/Extra-Embryonic Cell Identities during Lineage Priming. Cell Rep. *24*, 1977–1985.e7. https://doi.org/10.1016/j.celrep.2018.07.077.

73. Meissner, A., Mikkelsen, T.S., Gu, H., Wernig, M., Hanna, J., Sivachenko, A., Zhang, X., Bernstein, B.E., Nusbaum, C., Jaffe, D.B., et al. (2008). Genome-scale DNA methylation maps of pluripotent and differentiated cells. Nature *454*, 766–770. https://doi.org/10.1038/nature07107.

74. Morselli, M., Pastor, W.A., Montanini, B., Nee, K., Ferrari, R., Fu, K., Bonora, G., Rubbi, L., Clark, A.T., Ottonello, S., et al. (2015). In vivo targeting of de novo DNA methylation by histone modifications in yeast and mouse. eLife *4*, e06205. https://doi.org/10.7554/eLife.06205.

75. Schübeler, D. (2015). Function and information content of DNA methylation. Nature *517*, 321–326. https://doi.org/10.1038/nature14192.

76. Kreibich, E., Kleinendorst, R., Barzaghi, G., Kaspar, S., and Krebs, A.R. (2023). Single-molecule footprinting identifies context-dependent regulation of enhancers by DNA methylation. Mol. Cell *83*, 787–802.e9. https://doi.org/10.1016/j.molcel.2023.01.017.

77. Loyfer, N., Magenheim, J., Peretz, A., Cann, G., Bredno, J., Klochendler, A., Fox-Fisher, I., Shabi-Porat, S., Hecht, M., Pelet, T., et al. (2023). A DNA methylation atlas of normal human cell types. Nature *613*, 355–364. https://doi.org/10.1038/s41586-022-05580-6.

78. Murakami, S., and Jaffrey, S.R. (2022). Hidden codes in mRNA: control of gene expression by m6A. Mol. Cell *82*, 2236–2251. https://doi.org/10.1016/j.molcel.2022.05.029.

79. Collignon, E. (2024). Unveiling the role of cellular dormancy in cancer progression and recurrence. Curr. Opin. Oncol. *36*, 74–81. https://doi.org/10.1097/CCO.0000000000001013.

80. Wu, Y., Xu, X., Qi, M., Chen, C., Li, M., Yan, R., Kou, X., Zhao, Y., Liu, W., Li, Y., et al. (2022). N6-methyladenosine regulates maternal RNA maintenance in oocytes and timely RNA decay during mouse maternal-to-zygotic transition. Nat. Cell Biol. *24*, 917–927. https://doi.org/10.1038/s41556-022-00915-x.

81. Macrae, T.A., Fothergill-Robinson, J., and Ramalho-Santos, M. (2023). Regulation, functions and transmission of bivalent chromatin during mammalian development. Nat. Rev. Mol. Cell Biol. *24*, 6–26. https://doi.org/10.1038/s41580-022-00518-2.

82. Bertero, A., Brown, S., Madrigal, P., Osnato, A., Ortmann, D., Yiangou, L., Kadiwala, J., Hubner, N.C., de Los Mozos, I.R., Sadée, C., et al. (2018). The SMAD2/3 interactome reveals that TGFβ controls m6A mRNA methylation in pluripotency. Nature *555*, 256–259. https://doi.org/10.1038/nature25784.

83. He, P.C., and He, C. (2021). m6 A RNA methylation: from mechanisms to therapeutic potential. EMBO J. *40*, e105977. https://doi.org/10.15252/embj.2020105977.

84. Xiao, S., Cao, S., Huang, Q., Xia, L., Deng, M., Yang, M., Jia, G., Liu, X., Shi, J., Wang, W., et al. (2019). The RNA N6-methyladenosine modification landscape of human fetal tissues. Nat. Cell Biol. *21*, 651–661. https://doi.org/10.1038/s41556-019-0315-4.

85. Kan, R.L., Chen, J., and Sallam, T. (2022). Crosstalk between epitranscriptomic and epigenetic mechanisms in gene regulation. Trends Genet. *38*, 182–193. https://doi.org/10.1016/j.tig.2021.06.014.

86. Śledź, P., and Jinek, M. (2016). Structural insights into the molecular mechanism of the m(6)A writer complex. eLife *5*, e18434. https://doi.org/10.7554/eLife.18434.

87. Sharif, J., Endo, T.A., Nakayama, M., Karimi, M.M., Shimada, M., Katsuyama, K., Goyal, P., Brind'Amour, J., Sun, M.-A., Sun, Z., et al. (2016). Activation of Endogenous Retroviruses in Dnmt1(-/-) ESCs Involves Disruption of SETDB1-Mediated Repression by NP95 Binding to Hemimethylated DNA. Cell Stem Cell *19*, 81–94. https://doi.org/10.1016/j.stem.2016.03.013.

88. Stielow, B., Sapetschnig, A., Wink, C., Krüger, I., and Suske, G. (2008). SUMO-modified Sp3 represses transcription by provoking local heterochromatic gene silencing. EMBO Rep. *9*, 899–906. https://doi.org/10.1038/embor.2008.127.

89. Schmidt, C.S., Bultmann, S., Meilinger, D., Zacher, B., Tresch, A., Maier, K.C., Peter, C., Martin, D.E., Leonhardt, H., and Spada, F. (2012). Global DNA hypomethylation prevents consolidation of differentiation programs and allows reversion to the embryonic stem cell state. PLoS One *7*, e52629. https://doi.org/10.1371/journal.pone.0052629.

90. Ran, F.A., Hsu, P.D., Wright, J., Agarwala, V., Scott, D.A., and Zhang, F. (2013). Genome engineering using the CRISPR-Cas9 system. Nat. Protoc. *8*, 2281–2308. https://doi.org/10.1038/nprot.2013.143.

91. Estève, P.-O., Chin, H.G., Smallwood, A., Feehery, G.R., Gangisetty, O., Karpf, A.R., Carey, M.F., and Pradhan, S. (2006). Direct interaction between DNMT1 and G9a coordinates DNA and histone methylation during replication. Genes Dev. *20*, 3089–3103. https://doi.org/10.1101/gad.1463706.

92. Dedeurwaerder, S., Desmedt, C., Calonne, E., Singhal, S.K., Haibe-Kains, B., Defrance, M., Michiels, S., Volkmar, M., Deplus, R., Luciani, J., et al. (2011). DNA methylation profiling reveals a predominant immune component in breast cancers. EMBO Mol. Med. *3*, 726–741. https://doi.org/10.1002/emmm.201100801.

93. Gandin, V., Sikström, K., Alain, T., Morita, M., McLaughlan, S., Larsson, O., and Topisirovic, I. (2014). Polysome fractionation and analysis of mammalian translatomes on a genome-wide scale. J. Vis. Exp. *87*, 51455. https://doi.org/10.3791/51455.

94. Beckedorff, F., Blumenthal, E., DaSilva, L.F., Aoi, Y., Cingaram, P.R., Yue, J., Zhang, A., Dokaneheifard, S., Valencia, M.G., Gaidosh, G., et al. (2020). The Human Integrator Complex Facilitates Transcriptional Elongation by Endonucleolytic Cleavage of Nascent Transcripts. Cell Rep. *32*, 107917. https://doi.org/10.1016/j.celrep.2020.107917.

95. Babraham Bioinformatics (2023). FastQC A Quality Control tool for High Throughput Sequence Data. https://www.bioinformatics.babraham.ac.uk/projects/fastqc/.
96. Chen, S., Huang, T., Zhou, Y., Han, Y., Xu, M., and Gu, J. (2017). AfterQC: automatic filtering, trimming, error removing and quality control for fastq data. BMC Bioinformatics *18* (*Suppl 3*), 80. https://doi.org/10.1186/s12859-017-1469-3.
97. Langmead, B., and Salzberg, S.L. (2012). Fast gapped-read alignment with Bowtie 2. Nat. Methods *9*, 357–359. https://doi.org/10.1038/nmeth.1923.
98. Bolger, A.M., Lohse, M., and Usadel, B. (2014). Trimmomatic: a flexible trimmer for Illumina sequence data. Bioinformatics *30*, 2114–2120. https://doi.org/10.1093/bioinformatics/btu170.
99. Dobin, A., Davis, C.A., Schlesinger, F., Drenkow, J., Zaleski, C., Jha, S., Batut, P., Chaisson, M., and Gingeras, T.R. (2013). STAR: ultrafast universal RNA-seq aligner. Bioinformatics *29*, 15–21. https://doi.org/10.1093/bioinformatics/bts635.
100. Yates, A., Akanni, W., Amode, M.R., Barrell, D., Billis, K., Carvalho-Silva, D., Cummins, C., Clapham, P., Fitzgerald, S., Gil, L., et al. (2016). Ensembl 2016. Nucleic Acids Res. *44*, D710–D716. https://doi.org/10.1093/nar/gkv1157.
101. Volders, P.-J., Anckaert, J., Verheggen, K., Nuytens, J., Martens, L., Mestdagh, P., and Vandesompele, J. (2019). LNCipedia 5: towards a reference set of human long non-coding RNAs. Nucleic Acids Res. *47*, D135–D139. https://doi.org/10.1093/nar/gky1031.
102. Anders, S., Pyl, P.T., and Huber, W. (2015). HTSeq–a Python framework to work with high-throughput sequencing data. Bioinformatics *31*, 166–169. https://doi.org/10.1093/bioinformatics/btu638.
103. Antanaviciute, A., Baquero-Perez, B., Watson, C.M., Harrison, S.M., Lascelles, C., Crinnion, L., Markham, A.F., Bonthron, D.T., Whitehouse, A., and Carr, I.M. (2017). m6aViewer: software for the detection, analysis, and visualization of N6-methyladenosine peaks from m6A-seq/ME-RIP sequencing data. RNA *23*, 1493–1501. https://doi.org/10.1261/rna.058206.116.
104. Zhu, S., Xiang, J.-F., Chen, T., Chen, L.-L., and Yang, L. (2013). Prediction of constitutive A-to-I editing sites from human transcriptomes in the absence of genomic sequences. BMC Genomics *14*, 206. https://doi.org/10.1186/1471-2164-14-206.
105. Thorvaldsdóttir, H., Robinson, J.T., and Mesirov, J.P. (2013). Integrative Genomics Viewer (IGV): high-performance genomics data visualization and exploration. Brief. Bioinform. *14*, 178–192. https://doi.org/10.1093/bib/bbs017.
106. Robinson, M.D., McCarthy, D.J., and Smyth, G.K. (2010). edgeR: a Bioconductor package for differential expression analysis of digital gene expression data. Bioinformatics *26*, 139–140. https://doi.org/10.1093/bioinformatics/btp616.
107. Love, M.I., Huber, W., and Anders, S. (2014). Moderated estimation of fold change and dispersion for RNA-seq data with DESeq2. Genome Biol. *15*, 550. https://doi.org/10.1186/s13059-014-0550-8.
108. Li, B., and Dewey, C.N. (2011). RSEM: accurate transcript quantification from RNA-Seq data with or without a reference genome. BMC Bioinformatics *12*, 323. https://doi.org/10.1186/1471-2105-12-323.
109. Li, H., Handsaker, B., Wysoker, A., Fennell, T., Ruan, J., Homer, N., Marth, G., Abecasis, G., and Durbin, R.; 1000 Genome Project Data Processing Subgroup (2009). The Sequence Alignment/Map format and SAMtools. Bioinformatics *25*, 2078–2079. https://doi.org/10.1093/bioinformatics/btp352.
110. Soneson, C., Love, M.I., and Robinson, M.D. (2015). Differential analyses for RNA-seq: transcript-level estimates improve gene-level inferences. F1000Res *4*, 1521. https://doi.org/10.12688/f1000research.7563.2.
111. Dedeurwaerder, S., Defrance, M., Bizet, M., Calonne, E., Bontempi, G., and Fuks, F. (2014). A comprehensive overview of Infinium HumanMethylation450 data processing. Brief. Bioinform. *15*, 929–941. https://doi.org/10.1093/bib/bbt054.
112. McCartney, D.L., Walker, R.M., Morris, S.W., McIntosh, A.M., Porteous, D.J., and Evans, K.L. (2016). Identification of polymorphic and off-target probe binding sites on the Illumina Infinium MethylationEPIC BeadChip. Genom. Data *9*, 22–24. https://doi.org/10.1016/j.gdata.2016.05.012.
113. Dedeurwaerder, S., Defrance, M., Calonne, E., Denis, H., Sotiriou, C., and Fuks, F. (2011). Evaluation of the Infinium Methylation 450K technology. Epigenomics *3*, 771–784. https://doi.org/10.2217/epi.11.105.
114. Harrow, J., Frankish, A., Gonzalez, J.M., Tapanari, E., Diekhans, M., Kokocinski, F., Aken, B.L., Barrell, D., Zadissa, A., Searle, S., et al. (2012). GENCODE: the reference human genome annotation for the ENCODE Project. Genome Res. *22*, 1760–1774. https://doi.org/10.1101/gr.135350.111.
115. Hinrichs, A.S., Karolchik, D., Baertsch, R., Barber, G.P., Bejerano, G., Clawson, H., Diekhans, M., Furey, T.S., Harte, R.A., Hsu, F., et al. (2006). The UCSC Genome Browser Database: update 2006. Nucleic Acids Res. *34*, D590–D598. https://doi.org/10.1093/nar/gkj144.
116. Quinlan, A.R., and Hall, I.M. (2010). BEDTools: a flexible suite of utilities for comparing genomic features. Bioinformatics *26*, 841–842. https://doi.org/10.1093/bioinformatics/btq033.
117. Ramírez, F., Ryan, D.P., Grüning, B., Bhardwaj, V., Kilpert, F., Richter, A.S., Heyne, S., Dündar, F., and Manke, T. (2016). deepTools2: a next generation web server for deep-sequencing data analysis. Nucleic Acids Res. *44*, W160–W165. https://doi.org/10.1093/nar/gkw257.
118. Gaidatzis, D., Burger, L., Florescu, M., and Stadler, M.B. (2015). Analysis of intronic and exonic reads in RNA-seq data characterizes transcriptional and post-transcriptional regulation. Nat. Biotechnol. *33*, 722–729. https://doi.org/10.1038/nbt.3269.
119. Martin, M. (2011). Cutadapt removes adapter sequences from high-throughput sequencing reads. EMBnet J. *17*, 10. https://doi.org/10.14806/ej.17.1.200.
120. Langmead, B., Trapnell, C., Pop, M., and Salzberg, S.L. (2009). Ultrafast and memory-efficient alignment of short DNA sequences to the human genome. Genome Biol. *10*, R25. https://doi.org/10.1186/gb-2009-10-3-r25.
121. Korotkevich, G., Sukhov, V., Budin, N., Shpak, B., Artyomov, M.N., and Sergushichev, A. (2021). Fast gene set enrichment analysis. Preprint at bioRxiv. https://doi.org/10.1101/060012.

STAR★METHODS

KEY RESOURCES TABLE

REAGENT or RESOURCE	SOURCE	IDENTIFIER
Antibodies		
Mouse monoclonal anti-β-Actin	Sigma Aldrich	Cat#A5316; RRID:AB_476743
Rabbit polyclonal anti-Dnmt1	Abcam	Cat#ab19905; RRID:AB_731983
Rabbit monoclonal anti-Dnmt1	Cell Signaling Technology	Cat#5032; RRID:AB_10548197
Mouse monoclonal anti-DNMT1	Invitrogen	Cat# 60B1220.1; RRID:AB_838131
Rabbit polyclonal anti-METTL3	Proteintech	Cat#15073-1-AP; RRID:AB_2142033
Rabbit polyclonal anti-METTL14	Sigma Aldrich	Cat#HPA038002; RRID:AB_10672401
Mouse monoclonal anti-FLAG® M2	Sigma Aldrich	Cat#F3165; RRID:AB_259529
Mouse monoclonal anti-6X His tag®	Abcam	Cat#ab18184; RRID:AB_444306
Mouse monoclonal anti-Myc-tag	Cell Signaling Technology	Cat#2276; RRID:AB_331783
Mouse monoclonal anti-GAL4 (DBD) (RK5C1)	Santa Cruz Biotechnology	Cat#sc-510; RRID:AB_627655
Mouse monoclonal anti-GST tag	Cell Signaling Technology	Cat# 2624; RRID:AB_2189875
Mouse monoclonal anti-TBP	Abcam	Cat#ab818;RRID: AB_306337
Rabbit polyclonal anti-H3	Abcam	Cat#ab1791;RRID:AB_302613
Rabbit monoclonal anti-H3	Cell Signaling Technology	Cat#4499;RRID: AB_10544537
Rabbit monoclonal anti-SETD2	Cell Signaling Technology	Cat# 80290; RRID:AB_3105876
Rabbit monoclonal anti-Dnmt3a	Abcam	Cat#ab307503; RRID:AB_3105875
Rabbit monoclonal anti-DNMT3B	Cell Signaling Technology	Cat# 57868;RRID: AB_2799534
Rabbit monoclonal anti-H3K36me3	Cell Signaling Technology	Cat# 4909; RRID:AB_1950412
Rabbit monoclonal anti-FOXA2	Cell Signaling Technology	Cat# 8186; RRID:AB_10891055
Rabbit monoclonal anti-GATA4	Abcam	Cat# ab307823; RRID:AB_3105880
Rabbit monoclonal anti-GATA6	Cell Signaling Technology	Cat# 5851; RRID:AB_10705521
Rabbit monoclonal anti-SOX17	Abcam	Cat# ab224637; RRID:AB_2801385
Mouse monoclonal anti-GAPDH	Proteintech	Cat#60004-1-Ig; RRID:AB_2107436
Goat polyclonal secondary antibody anti-Mouse Alexa Fluor 594	ThermoFisher Scientific	Cat# A-11005; RRID: AB_2534073
Rabbit monoclonal anti-m^6A	Synaptic Systems	Cat#202003; RRID:AB_2279214
Mouse monoclonal anti-5mC	Diagenode	Cat# C15200003; RRID:AB_3105883
Bacterial and virus strains		
BL21 DE3	NEB	C2527H
Chemicals, peptides, and recombinant proteins		
STM-2457 METTL3 inhibitor	MedChemExpress	HY-134836; CAS: 2499663-01-1
FB23-2 FTO demethylase inhibitor	MedChemExpress	HY-127103; CAS: 2243736-45-8
MEK inhibitor PD0325901	Axon MedChem	Cat#1408; CAS: 391210-10-9
GSK3 inhibitor CHIR99021	Axon MedChem	Cat#1386; CAS: 252917-06-9
Actinomycin D	Sigma-Aldrich	Cat#SBR00013; CAS: 50-76-0
Cycloheximide	Sigma-Aldrich	Cat#C4859; CAS: 66-81-9
Lipofectamine 2000	Invitrogen	Cat# 11668019
Lipofectamine 3000	Invitrogen	Cat# L3000-008
FuGENE Transfection Reagent	Promega	Cat# E2311
TRIzol LS	Invitrogen	Cat#10296028
Isopropylthiogalactosidase (IPTG)	Sigma	Cat#3I5502-1G
cOmplete™ Mini Protease Inhibitor Cocktail	Roche	Cat#11836153001

(*Continued on next page*)

Continued

REAGENT or RESOURCE	SOURCE	IDENTIFIER
L-Glutathione reduced	Sigma-Aldrich	Cat# G4251-5G
RNase-Free DNase Set	Qiagen	Cat#79254
NanoBRET 618 fluorescent ligand	Promega	Cat#G9801
NanoBRET furimazine substrate	Promega	Cat#N1571
Human Recombinant DNMT1	Active Motif	Cat#31404; GenPept:P26358
Human Recombinant METTL3	Active Motif	Cat#31567; GenPept:Q86U44
Human Recombinant METTL14	Active Motif	Cat#31568; GenPept:Q9HCE5
Human Recombinant Histone H2A	This paper	N/A
Human Recombinant Histone H2B	This paper	N/A
Human Recombinant Histone H3.1	This paper	N/A
Human Recombinant Histone H4	This paper	N/A
Human Recombinant Biotinylated Nucleosome	This paper	N/A
Human Recombinant Biotinylated Nucleosome-H3K36me3	EpiCypher	Cat#16-0320; GenPept: P04908, O60814, P68431, P62805
Human Recombinant GST- DNMT3B-PWWP	Active Motif	Cat#31542; GenPept: Q9UBC3
Human Recombinant GST-METTL3	This paper	N/A
Human Recombinant GST-METTL14	This paper	N/A
Human Recombinant GST-METTL14-NLS	This paper	N/A
Human Recombinant GST-METTL14-MTD	This paper	N/A
Human Recombinant GST-METTL14-RGG	This paper	N/A
Human Recombinant GST-METTL14-RGG1	This paper	N/A
Human Recombinant GST-METTL14-RGG2	This paper	N/A
ESGRO® Recombinant Mouse LIF Protein	Merck Millipore	Cat#ESG1107
Critical commercial assays		
RNeasy Kit	Qiagen	Cat#74004
mRNA Miniprep Kit	Sigma-Aldrich	Cat#MRN10
QIAamp DNA Mini Kit	Qiagen	Cat#51306
EZ DNA 462 Methylation Kit	Zymo Research	Cat#D5002
HotStarTaq DNA Polymerase	Qiagen	Cat#203205
DC™ Protein Assay Kit	Bio-Rad	Cat#5000112
Deposited data		
All raw gel data are deposited at Mendeley Data	This paper	https://doi.org/10.17632/k9w73kftmt.1
Raw and analyzed data	This paper	GEO: GSE184757
Human and mouse rRNA and tRNA sequences for sequencing data filtering	The National Center for Biotechnology Information (NCBI)	https://www.ncbi.nlm.nih.gov/nuccore
Human reference genome build 37 (GRCh37), transcriptome and annotation version 85 for sequencing data analyses	Ensembl	https://ftp.ensembl.org/pub/grch37/release-85/
Human reference annotation version 28 for Infinium array analyses	Gencode	https://www.gencodegenes.org/human/release_28.html
Mouse reference annotation version M25 for Infinium array analyses	Gencode	https://www.gencodegenes.org/mouse/release_M25.html
Human long noncoding transcriptome and annotation version 5.2	LNCipedia	https://lncipedia.org/
Mouse reference genome, build 38 (GRCm38), transcriptome and annotation version 99	Ensembl	https://ftp.ensembl.org/pub/release-99/
Illumina Manifests for infinium probe target chromosomic positions	Illumina	https://support.illumina.com/

(*Continued on next page*)

Continued

REAGENT or RESOURCE	SOURCE	IDENTIFIER
Experimental models: Cell lines		
HeLa	ATCC	N/A
HeLa METTL3 knockout	This study	N/A
COS-7	Laboratory of Sriharsa Pradhan	N/A
HEK293	Promega Corporation	N/A
HEK293^{5XUAS}	Laboratory of Bastian Stielow	N/A
mouse embryonic stem cells J1 WT/Mettl3 knockout	Laboratory of Howard Y. Chang	N/A
mouse embryonic stem cells J1 WT/Dnmt1 knockout	Laboratory of Fabio Spada	N/A
mouse embryonic stem cells E14TG2a WT/Mettl14 knockout	Laboratory of Laixin Xia	N/A
mouse embryonic stem cells E14TG2a Mettl14 knockout + Mettl14^{WT} or Mettl14$^{\Delta RGG}$	This study	N/A
Oligonucleotides		
DNA oligos	This study	See Table S7
Recombinant DNA		
Plasmid: pcDNA3.1-Myc/His-METTL3	This study	N/A
Plasmid: pcDNA3.1-Myc/His-METTL14	This study	N/A
Plasmid: RFP-DNMT1	This study	N/A
Plasmid: NanoLuc-METTL3	This study	N/A
Plasmid: NanoLuc-METTL14	This study	N/A
Plasmid: HaloTag-DNMT1	This study	N/A
Plasmid: pGex-4T1-GST-METTL14 (full-length or partial)	This study	N/A
Plasmid: pFlag-CMV2-METTL14 (full-length or partial)	This study	N/A
Plasmid: pcDNA3-Myc-DNMT1	Addgene	Cat#36939
Plasmid: pcDNA3-GAL4-METTL14 (full-length or partial)	This study	N/A
Plasmid: pFlag-CMV2-DNMT1	This study	N/A
Plasmid: pLV-EF1a-IRES-Mettl14 (full-length or partial)	This study	N/A
Software and algorithms		
Graphpad Prism 7	GraphPad	https://www.graphpad.com/
Biorender	Biorender	https://www.biorender.com
R version 4.2.2	The R Project	https://cran.r-project.org/
Heatmapper webtool	Meissner et al.[73]	http://www.heatmapper.ca/
Zen version 2.1	Zeiss	https://www.zeiss.com/
ImageJ	Xia et al.[46]	https://imagej.nih.gov/ij/
LiftOver webtool	Bisia et al.[70]	https://genome.ucsc.edu/cgi-bin/hgLiftOver
FastQC version 0.11.5	Yang et al.[50]	https://github.com/s-andrews/FastQC
AfterQC version 0.9.6	Su et al.[51]	https://github.com/OpenGene/AfterQC
Bowtie2 version 2.3.4.1	Collignon et al.[52]	https://bowtie-bio.sourceforge.net/bowtie2
Trimmomatic version 0.33	Kalkan et al.[53]	http://www.usadellab.org/cms/?page=trimmomatic
STAR version 2.6.0c	Zhang et al.[54]	https://github.com/alexdobin/STAR
RSEM version 1.3.1	Ke et al.[61]	https://github.com/deweylab/RSEM
samtools version 1.6.2	Hayashi et al.[62]	http://www.htslib.org/
HTseq counts version 0.9.1	Herzog et al.[57]	https://pypi.python.org/pypi/HTSeq
tximport version 1.10.1	Krishnakumar et al.[63]	https://bioconductor.org/packages/release/bioc/html/tximport.html
DESeq2 version 1.22.2	Yang et al.[64]	https://bioconductor.org/packages/release/bioc/html/DESeq2.html
m6aViewer version 1.6.1	Neumann et al.[58]	http://dna2.leeds.ac.uk/m6a/

(*Continued on next page*)

Continued

REAGENT or RESOURCE	SOURCE	IDENTIFIER
Bedtools version 2.27.1	Wang et al.[71]	https://github.com/arq5x/bedtools2
bamTobw	Kim et al.[59]	https://github.com/YangLab/bamTobw
IGV tool version 2.9.4	Varley et al.[60]	https://software.broadinstitute.org/software/igv/

EXPERIMENTAL MODEL AND STUDY PARTICIPANT DETAILS

Cell lines

HeLa, COS-7, and HEK293/T cells and HEK293^{5XUAS} cells containing the stably integrated 5xUAS-luciferase reporter (gift from Bastian Stielow, Philipps University, Marburg, Germany)[88] were maintained in DMEM supplemented with 10% FBS and 1% penicillin and streptomycin (Gibco). Mettl3 knockout (KO) and wild-type (WT) J1 mouse embryonic stem cells (ESCs) (gift from Howard Y. Chang, Stanford University, USA)[23] and Dnmt1 KO mouse ESCs and the corresponding wild type (gift from Fabio Spada, Ludwig Maximilians University, Germany)[89] were cultured in high-glucose DMEM-containing 15% FBS, 1mM sodium pyruvate, 1% non-essential amino acids, 1% glutaMAX™, 1% penicillin and streptomycin, 0.1mM β-mercaptoethanol (Gibco), and 1000 units/ml recombinant mouse leukemia inhibitory factor (LIF) (Millipore) on tissue culture plates coated with 0.1% gelatin and feeder cells (irradiated mouse embryonic fibroblasts). Mettl14 KO and WT E14TG2a mouse ESCs (gift from Laixin Xia, Southern Medical University, Guangzhou, China)[32] and the corresponding rescued ES cell lines (generated in this study) were cultured on tissue culture plates coated with 0.1% gelatin, in N2B27 medium (50% DMEM/F12 and 50% Neurobasal Medium (Gibco), containing 0.1mM β-mercaptoethanol (Gibco), 2 mM L-glutamine (Gibco), B-27 serum-free supplement (Gibco), N2 supplement (Gibco), 1% penicillin and streptomycin), supplemented with 1000 units/ml recombinant mouse leukemia inhibitory factor (LIF) (Millipore), and a mixture, here called "2i", of the small-molecule inhibitors CHIR99021 (3μM, Axon Medchem) and PD0325901 (1μM, Axon Medchem). All cells were cultured at 37°C under 5% CO2 and routinely tested for mycoplasma contamination with the MycoAlert™ Mycoplasma Detection Kit (Lonza). None of these cell lines are listed in the database, maintained by ICLAC, of commonly misidentified cell lines.

METHOD DETAILS

Manipulations on cultured cells

Transfection of HeLa and HEK293^{5XUAS} cells was done with Lipofectamine™ 2000 or 3000 (Invitrogen) as indicated, and transfection of COS-7 cells was carried out with Fugene HD transfection reagent (Promega) according to the manufacturer's protocols. HEK293/T cells were transfected with either Lipofectamine™ 2000 or 3000 as indicated or with Fugene HD transfection reagent, according to the manufacturer's protocols.

For drug treatments, HeLa cells were seeded and treated with METTL3 inhibitor STM-2457 (MedChemExpress, HY-134836) at 1, 5, and 25μM, with FTO inhibitor (MedChemExpress, HY-127103) at 20μM, or with the corresponding vehicle control. After 72h of treatment, the cells were harvested and subjected to further analyses. ESCs were treated with METTL3 inhibitor STM-2457 at 50μM or with its vehicle control and collected 24h post-treatment for further analysis.

In vitro differentiation of ESCs

The transition from naïve to formative pluripotency was adapted from previous protocols.[62,63] Briefly, 2×10^6 naïve pluripotent ESCs were cultured on tissue culture plates coated with 0.1% gelatin, in "naïve medium" (2i/LIF serum-free N2B27 medium, see "cell lines" section). After 12 hours, the medium was replaced with FBS-containing medium (high-glucose DMEM containing 15% FBS, 1mM sodium pyruvate, 1% non-essential amino acids, 1% glutaMAX™, 1% penicillin and streptomycin, 0.1mM β-mercaptoethanol (Gibco)) to induce formative pluripotency. Cells cultured under these conditions were collected after 3 or 24 hours for further analysis.

Embryoid bodies (EBs) were obtained by spontaneous differentiation of ESCs. Briefly, ESCs were trypsinized and counted with a TC20™ Automated Cell Counter (BIORAD). They were seeded onto Petri dishes at 4×10^6 ESCs/dish (Greiner) in 15 ml EB medium (high-glucose DMEM-containing 15% FBS, 1mM sodium pyruvate, 1% non-essential amino acids, 1% glutaMAX™, 1% penicillin and streptomycin, 0.1mM β-mercaptoethanol (Gibco) and maintained for 8 days. The cells were precipitated by gravity, resuspended, and cultured in fresh medium every two days before collection of the EBs for further analysis. Brightfield microscopy images of the EBs were captured with an inverted microscope (Axio Observer 7, Zeiss). The area of each EB was measured with the ImageJ software, and the actual area (in μm^2) was calculated on the basis of the scale provided in the images.

Cell line generation

The METTL3 KO HeLa cell line was generated with the CRISPR-Cas9 nuclease system by homology-directed repair (HDR).[90] Briefly, sgRNAs were designed to target the start codon (ATG) and the first intron (about 500 bp downstream of ATG) of METTL3 according to the guidelines listed on the CRISPOR website (http://crispor.tefor.net). The sgRNAs were cloned into the pX461 vector (Addgene, 48140). In parallel, donor pUC18 vectors (GenScript, SD1162) were generated, containing gene sequences homologous to those flanking the sgRNA targeting sites, an adjacent selectable marker (mCherry or a puromycin resistance gene), and a mammalian transcriptional terminator (bGH, synthesized by Genewiz) or a triple terminator (bGH+hGH+SV40, synthesized by Genewiz). Co-transfection of HeLa cells with the donor vectors and gRNA-containing plasmids at a ratio of 2:1 was performed with Lipofectamine™ 2000 according to the manufacturer's instructions (Invitrogen). Twenty-four hours post-transfection, selection was initiated with 2μg/ml puromycin and continued for at least 10 days. Surviving mCherry-positive cells were sorted into 96-well plates (1 cell/well) by fluorescence-activated cell sorting (FACS) and grown for two to three weeks before clones were transferred into 24-well plates and METTL3 expression was measured by quantitative reverse transcription PCR (RT-qPCR) and western blotting. CRISPR-Cas9-targeted genomic regions in positive clones were PCR-amplified and sequenced. All relevant sgRNA sequences and primers are listed in Table S7.

In RNAi experiments, HeLa cells were transfected in 10 cm dishes with 20 nM short interfering RNAs (siRNAs, Horizon), using INTERFERin (Sartorius) according to the manufacturer's protocol. RNAi induction was performed in two rounds: an initial siRNA transfection followed by a second transfection 48 hours later. Cells were reseeded between transfection rounds and harvested after 96 hours (from the first transfection). The knockdown efficiency was checked by western blotting.

For Mettl14-rescued cells, a Mettl14^{WT} or Mettl14$^{\Delta RGG}$ cDNA was cloned into plasmid pLV-EF1a-IRES (Blasticidin S resistant) and used, along with packaging vectors (pMD2.G and psPAX2), to co-transfect HEK293/T cells with Lipofectamine™ 3000, according to the manufacturer's protocol. Supernatant containing lentivirus particles was collected 48 and 72 hours post-transfection, supplemented with polybrene, and used to infect Mettl14 KO ESCs. After two rounds of infection, cells were selected for 7 days with 10μg/ml blasticidin S48 and the surviving cells were pooled as stably rescued cell lines.

Immunofluorescence

Fugene HD transfection reagent (Promega) was used according to the manufacturer's recommendations to co-transfect COS-7 cells with 500ng Myc-METTL3 or Myc-METTL14 (in house) and RFP-DNMT1[91] plasmid. As control, cells were co-transfected, as described above, with Myc-METTL3 or Myc-METTL14 and 500ng empty backbone vector encoding RFP or with RFP-DNMT1 and empty backbone vector encoding the Myc tag. After 48 h, the cells were crosslinked with 4% paraformaldehyde (Electron Microscopy Sciences, 15710) for 10 min at room temperature (RT) and quenched with 0.125M glycine for 5 min at RT. After 20 min of permeabilization with 100% methanol at -20°C, the cells were incubated for 1 h at RT with PBS containing 0.5% Tween 20 and 5% BSA (Millipore-Sigma Aldrich). Epitope-tagged METTL3 or METTL14 was detected with mouse anti-Myc antibody (Cell Signaling Technology, 2276S) and visualized with an anti-mouse IgG coupled to Alexa Fluor 594 dye (ThermoFisher Scientific, A-11005). Myc-METTL3/14 and RFP-DNMT1 were detected respectively with a 458, 488, 514nm multiline argon laser and a 561nm DPSS laser. Slides were mounted with Prolong Gold Antifade Mountant with DAPI (Thermo Fisher Scientific, P36931). Images were captured with a confocal microscope (LSM 880, Zeiss).

For immunofluorescence in EBs, the structures were fixed in 4% paraformaldehyde solution for 2 hours at 4°C and washed three times with PBS under gentle shaking before being transferred into 30% (v:v) sucrose-PBS solution for cryopreservation. Fixed EBs were embedded in Tissue Freezing Medium (Leica) and cryosectioned to a thickness of 20μm under RNase-free conditions. The cryosections were washed with 1% SDS-PBS before 1h of permeabilization/blocking (3% BSA, 5% horse serum, and 0.3% Triton X-100 in PBS). After incubation with the primary antibody (overnight, 4°C in 3% BSA, 1% horse serum, 0,1% Triton X100) the cryosections were washed three times with PBS and incubated for 2 hours at RT with secondary antibody and Hoechst 33258 (Merck). Following three washes with PBS, the samples were mounted with a coverglass in Glycergel (Agilent Dako) and images were acquired with a Leica DM3000 microscope with a 20x-magnification objective. The following primary antibodies were used: FoxA2 (Cell Signaling, 8186), Gata4 (Abcam, ab307823), Gata6 (Cell Signaling, 5851), Sox17 (Abcam, ab224637).

NanoBRET

For donor saturation assays, HEK293 cells (4×10^5) were plated in a 12-well plate and co-transfected with 10ng NanoLuc-METTL3 or NanoLuc-METTL14 vector (synthesized by Genscript) and increasing concentrations (0-1000 ng) of a HaloTag DNMT1 vector (synthesized by Genscript) or a negative control HaloTag vector (Promega, G6591) vector. In all experiments, the cells were collected 24h post-transfection and the medium was replaced with phenol red-free OptiMEM I Reduced Serum Medium with 4% FBS in the absence (control sample) or presence (experimental sample) of 100nM NanoBRET 618 fluorescent ligand (Promega). Cells (2×10^4 cells/well) were plated into a 96-well white assay plate (Corning Costar) and incubated at 37°C, 5% CO2. Forty-five hours post-transfection, NanoBRET furimazine substrate (Promega) was added to both control and experimental samples at 10μM final concentration. Readings were performed within 5 min with a GloMax Discover (Promega) equipped with 450/80nm bandpass and 610nm longpass filters (reading setting: 0.3s). A corrected BRET ratio was calculated and defined as the 610-to-450 nm emission ratio determined for experimental samples (i.e., those treated with NanoBRET fluorescent ligand) minus that determined for control samples (not treated with NanoBRET fluorescent ligand). BRET ratios are expressed in milliBRET units (mBU), 1mBU being defined as the corrected BRET ratio multiplied by 1000.

RNA extraction and RT-qPCR

Total RNA was extracted with the RNeasy Kit (Qiagen) according to the manufacturer's instructions. Residual DNA was removed with the RNase-Free DNase Set (Qiagen). RNA was quantified with the NanoDropTM 1000 Spectrophotometer (Thermo Scientific). One microgram of RNA was reverse transcribed with the First Strand cDNA Synthesis Kit (Roche). Gene expression was analyzed with the LightCycler 480 SYBR Green I Master mix (Roche) on the LightCycler 480 real-time PCR system (Roche). Gene expression levels were normalized to either human *GAPDH* or mouse *Gapdh* and *Tbp*. Primer sequences are listed in Table S7.

Western blotting

Cells were washed with ice-cold PBS (Lonza), scraped, and homogenized in ice-cold lysis buffer [50mM Tris-Cl (pH 8.0), 150mM NaCl, EDTA 5mM, 0.5% NonidetP40 (NP-40)] supplemented with cOmplete™ Mini Protease Inhibitor Cocktail (Roche) for 15-30min. After centrifuging for 10 min at 17,000 g and 4°C, the supernatant was collected and proteins were quantified with the DC™ Protein Assay Kit (Bio-Rad). For the cell fractionation assay, proteins were extracted with Subcellular Protein Fractionation Kit (Thermo Fisher) according to the manufacturer's protocols. Cell extracts were fractionated by SDS-PAGE and transferred to nitrocellulose membranes for immunostaining. Membranes were blocked for 1 h with 5% (w/v) non-fat dried skimmed milk powder (Bio-Rad) in TBST and then incubated overnight at 4°C with primary antibody in blocking buffer. Membranes were washed three times with TBST and incubated with a 1:10,000 dilution of horseradish-peroxidase-conjugated secondary antibody for 1h. After three washes with TBST, the membranes were developed with the ECL Plus system (Amersham Biosciences) or with the SuperSignal™ West Femto Maximum Sensitivity Substrate, according to the manufacturer's protocols. Protein bands were detected with the ChemiDoc™ Imaging Systems (Bio-Rad). The following primary antibodies were used: β-actin (Sigma Aldrich, A5316), GAPDH (Proteintech, 60004-1-Ig), TBP (Abcam, ab818), H3 (Abcam, ab1791, Cell Signalling, 4499), METTL3 (Proteintech, 15073-1-AP), METTL14 (Sigma Aldrich, HPA038002), DNMT1 (Abcam, ab19905), Dnmt1 (Cell Signaling, 5032), SETD2 (Cell Signaling, 80290), DNNT3A (Abcam, ab307503), DNMT3B (Cell Signaling, 57868), H3K36me3 (Cell Signaling, 4909), Flag (Sigma Aldrich, F3165), Myc (Cell Signaling, 2276), GAL4 (Santa Cruz, sc-510), GST (Cell Signaling, 2624).

Recombinant protein purification

GST and GST-tagged proteins were expressed in *Escherichia coli* strain BL21(DE3) with the pGex-4T1 vector system (Amersham Biosciences, 27-4580-01). A single transformed colony was picked and cultured overnight at 37°C in 40ml LB with 100μg/ml ampicillin. The following day, 350ml fresh LB with 100μg/ml ampicillin was added. Recombinant protein expression was induced with 0.1mM isopropylthiogalactosidase (IPTG) at 16°C for 4h. The cells were harvested by centrifugation and sonicated on ice in PBS (Lonza) supplemented with 1% Triton and cOmplete™ Mini Protease Inhibitor Cocktail (Roche). The lysate was then incubated with Glutathione Sepharose 4B GST-tagged protein purification resin (Cytiva, 17075601) for 2h at 4°C. Elution of GST-tagged proteins was performed for 10min at room temperature with 50mM Tris, 10mM glutathione, pH 8.0. The efficiency of recombinant protein production was tested by Coomassie Brilliant Blue staining.

Recombinant human histones (H2A, H2B, H3.1, and H4) were expressed in E. coli BL21(DE3) or C41(DE3) cells following induction with 500μM IPTG (4 hours at 37°C). Cells were resuspended in lysis buffer (200mM NaCl, 20mM Tris-HCl pH 7.6, 1mM EDTA, 1mM β-mercaptoethanol) and lysed by sonication. The lysates were cleared by centrifugation (30,000g for 20 minutes) and the insoluble pellet was resolubilized in extraction buffer (6M guanidine HCl, 1mM DTT, 1x PBS, pH 7) and nutated at 4°C overnight. The extracts were cleared by centrifugation (30,000 g for 40 minutes), filtered, and diluted 1:1 with HPLC buffer A (0.1% trifluoroacetic acid (TFA) in water) before purification by reverse-phase HPLC on a column eluted with 30-70% buffer B (0.1% TFA in 90% acetonitrile and 10% water). The efficiency of purification was determined by quadrupole LC-MS (Agilent) and the purified histones were lyophilized. To reconstitute histone octamers, lyophilized histones were dissolved in unfolding buffer (20mM Tris-HCl pH 7.6, 6M guanidine HCl, 0.5mM EDTA, 1mM DTT), combined at 1:1:0.95:0.95 molar ratio (H2A:H2B:H3.1:H4), and diluted to 1mg/ml with unfolding 3 x 1L refolding buffer (20mM Tris (pH 7.6), 2M NaCl, 0.5mM EDTA, and 1mM DTT). The assembled octamers were purified by size-exclusion chromatography with a GE Superdex 200 increase 10/300 GL column. Wild-type nucleosome core particles (WT NCPs) were assembled by salt gradient dialysis of purified octamers and biotinylated Widom-601 DNA, at molar ratios of 1.2, 1.24, and 1.28 in buffer (2mM NaCl, 5mM Tris-HCl pH 7.6, 0.5mM EDTA, 0.5mM DTT). Assembled nucleosomes were concentrated with a 30-kDa molecular weight cutoff centrifugal filter device (Millipore Sigma) and formation was analyzed by native gel electrophoresis (5% acrylamide gel, 0.5X TBE, 120 V, 45 minutes) with ethidium bromide.

GST pull-down assays

GST pull-down assays were performed by incubating bead-bound GST or GST-METTL14 (full-length or partial) with Flag/His-tagged recombinant human DNMT1 protein (Active Motif) at 4°C for 2 h in ice-cold binding buffer [50mM Tris-Cl (pH 8.0), 150mM NaCl, EDTA 5 mM, 0.5% NonidetP40 (NP-40)] supplemented with cOmplete™ Mini Protease Inhibitor Cocktail (Roche). The beads were washed five times with ice-cold binding buffer containing 300mM NaCl, pelleted at 500g for 1 min, and taken up in SDS–PAGE sample buffer. Pulled-down proteins were resolved by SDS-PAGE and subjected to western blotting.

Co-immunoprecipitation with purified recombinant proteins

Anti-His antibody (Abcam, ab18184) (1μg) was incubated overnight at 4°C with Flag-tagged recombinant human METTL14 protein (Active Motif) in the presence or absence of equimolar Flag/His-tagged recombinant human DNMT1 protein (Active Motif) in NP40 buffer [50mM Tris-Cl (pH 8.0), 150mM NaCl, EDTA 5 mM, 0.5% NonidetP40 (NP-40)] prior to addition of Dynabeads™ Protein G

(Invitrogen) and incubation for 2 h. After three washings, the proteins associated with Protein G magnetic beads were analyzed by western blotting.

In the ternary complex assay, 1μg anti-His antibody (Abcam) was incubated at 4°C overnight in ice-cold binding NP40 buffer supplemented with cOmplete™ Mini Protease Inhibitor Cocktail (Roche) with a fixed level of Flag/His-tagged recombinant human DNMT1 protein (Active Motif), either alone or with GST-tagged recombinant METTL14 protein (fixed level) or with the latter and GST-tagged recombinant METTL3 protein (increasing levels). This was followed by addition of Dynabeads™ Protein G (Invitrogen) and incubation for 2h. After washing, proteins associated with Protein G magnetic beads were analyzed by western blotting.

In the *in vitro* pull-down DNMT1/DNMT3B-H3K36me3 assay, 20 nM in-house biotinylated WT NCPs or purchased biotinylated H3K36me3 NCPs (Epicypher) was conjugated with MyOne Streptavidin T1 Dynabeads (ThermoFisher Scientific) in binding buffer (1x PBS, 1% NP-40, 5mM EDTA, 5% glycerol, pH 7.5) for 30 minutes on ice. On-bead NCPs were then incubated with either 200 nM recombinant DNMT1-His-FLAG (ActiveMotif) or 100 nM recombinant DNMT3B-PWWP-GST (ActiveMotif) for 1 hour on ice with gentle shaking. After incubation, the beads were washed four times with washing buffer (1x PBS with 300mM NaCl, 1% NP-40, 0.1% sodium dodecyl sulfate, 5% glycerol, pH 7.5) and eluted with 1x SDS-PAGE sample loading buffer. Samples were analyzed by western blotting.

Co-immunoprecipitation assays on cell lysates

For co-immunoprecipitation in transfected cells, cells were washed 24 h after transfection with ice-cold PBS (Lonza) and lysed in ice-cold buffer [50mM Tris-Cl (pH 8.0), 150mM NaCl, EDTA 5mM, 0.5% NonidetP40 (NP-40)] supplemented with cOmplete™ Mini Protease Inhibitor Cocktail (Roche) for 15-30 min. The lysate was centrifuged for 10 min at 17,000g and 4°C and the supernatant was collected. Five percent of the protein lysate was used as input, while the remainder was incubated with the indicated antibody or corresponding control IgG overnight at 4°C, prior to addition of Dynabeads™ Protein G (Invitrogen) and incubation for 2 h. Dynabead-associated proteins were then washed five times in lysis buffer and subjected to western blot analysis. To exclude any scaffolding role of RNA in the interaction between METTL14 and DNMT1, cell lysate was treated with RNAse (Thermo Fisher Scientific) for 15 minutes at 37°C prior to immunoprecipitation. For co-immunoprecipitation involving DNMT1-Myc or DNMT3B-Myc with H3K36me3, the cell lysate was sonicated before immunoprecipitation. The endogenous immunoprecipitation assays were carried out with a combination of monoclonal and polyclonal anti-DNMT1 antibodies (Abcam, ab19905, Invitrogen, 60B1220.1) at 1:1 ratio.

GAL4-5XUAS recruitment assay

Lipofectamine™ 3000 (Invitrogen) was used to co-transfect HEK293^{5XUAS} cells containing the stably integrated 5xUAS-luciferase reporter[1] with pcDNA3-GAL4-METTL14 fusion expression constructs and pFlag-CMV2-DNMT1 according to the manufacturer's protocols. The transfection efficiency was checked by western blotting for each replicate. Forty-eight hours after transfection, cells were crosslinked for 8 min at room temperature with 1% formaldehyde, the reaction was stopped by adding 0.125 M glycine and then washing twice with cold PBS. ChIP experiments were performed according to the iDeal ChIP-seq kit for Transcription Factors protocol (Diagenode, C01010055). Sonication was performed with Bioruptor plus (Diagenode) in cold water with the following settings: 30 min with 30-s ON/OFF intervals and high sonication strength. Flag antibody (Sigma Aldrich, F3165), GAL4 antibody (Santa Cruz, sc-510), and mouse control IgG (2μg each) were incubated with chromatin overnight at 4°C. After extensive washing steps, ChIP-ed DNA was eluted, de-crosslinked overnight at 65°C, and then purified. Three microliters of DNA-fragment-enriched immunoprecipitate or 3μl input, supplemented with 0.5μM primers and SYBR Green Master mix (Roche), was subjected to 40 PCR cycles in a LightCycler 480 II (Roche). The percentage of input recovered after immunoprecipitation was calculated with the ΔCt formula: $(2-(\text{Ct IP}-\text{Ct Input})) \times 100$. The primer sequences are indicated in Table S7.

Dot blotting for 5mC and m^{6}A quantification

DNA and RNA were extracted (Qiagen, 27106; 75162) and poly(A) enrichment was performed on the RNA extracts (Sigma Aldrich, MRN70-1KT). The samples were spotted onto a nylon membrane (GE Healthcare Hybond-N+), the membrane was dried, and UV crosslinking was performed at 4000 x 100μJ/cm2. The membrane was stained with 0.04% methylene blue in 0.5 M sodium acetate and rinsed with PBS + 0.1% Tween-20 for 5 min and blocked for 1h in 5% bovine serum albumin and horse serum (for 5mC) or 3% non-fat dry milk (for m^{6}A) in PBS + 0.1% Tween-20, transferred into blocking solution supplemented with mouse anti-5mC antibody (Diagenode, C15200003) or rabbit anti-m^{6}A antibody (Synaptic Systems, 202003) diluted 1:500, and incubated overnight at 4°C. Thereafter, the membrane was washed three times with PBS + 0.1% Tween-20 for a total of 30 min. It was transferred into blocking solution supplemented with horseradish-peroxidase-conjugated secondary antibodies diluted 1:1000, incubated for 1 h at room temperature, washed three times with PBS + 0.1% Tween-20, and developed with the ECL system (Amersham Biosciences) according to the manufacturer's instructions. ImageJ software was used for signal quantification.

Site-specific m^{6}A demethylation

For site-specific m^{6}A demethylation, 2.5×10^6 HEK293/T cells were seeded in a 10-cm plate. After 12 hours, cells were co-transfected with 9μg gRNA targeting SQLE (squalene epoxidase) or non-targeting control vector, along with 9μg dCasRX-ALBH5 plasmid, according to a published protocol.[46] Transfection was conducted with Lipofectamine™ 2000 according to the manufacturer's instructions. Thirty-six hours post-transfection, the cells were harvested for further analyses. The gRNA sequences are listed in Table S7.

Bisulfite pyrosequencing

Genomic DNA extraction, including the recommended proteinase K and RNase A digestions, was done with the QIAamp DNA Mini Kit (Qiagen, 51306) according to the manufacturer's protocol. Bisulfite conversion of genomic DNA (1μg) was performed with the EZ DNA Methylation Kit (Zymo Research, D5002). Then 3μl converted DNA (corresponding to approximately 150 ng DNA) was subjected to PCR amplification of the specific region. PCR assays were performed with HotStarTaq DNA Polymerase (Qiagen, 203205) under the following cycle conditions: 95°C for 15min, 50 cycles of (95°C for 30s; Tm°C for 1min; 72°C for 1min), 72°C for 7min, and finally cooling to 4°C. Amplification was confirmed on agarose gel and pyrosequencing of successfully amplified PCR products was performed with the PyroMark Q24 System (Qiagen). Primer sequences were designed with PyroMark Assay Design SW 2.0 (Qiagen) and are listed in Table S7.

RNA-seq

For ESCs and EBs (day 8), RNA-seq library preparation was performed with TruSeq Stranded Total RNA Library Prep Gold (96 Samples) and TruSeq RNA Single Indexes Set A and Set B, according to the manufacturer's instructions and starting with 100 ng total RNA. High-throughput sequencing was performed on the Illumina NextSeq500 system. For other samples, inputs from m^6A-seq (see m6A sequencing section) or SLAM-seq data (see SLAM-seq section, using total counts) were used to evaluate gene expression.

m^6A Sequencing

The method for m^6A sequencing (m^6A-seq) was adapted from a protocol described previously.[18] Starting with 500μg total RNA, enrichment in polyadenylated RNA was done through one round of oligo-dT selection with the GenElute mRNA Miniprep Kit (Sigma Aldrich). The selected RNAs were then fragmented by incubating 90μl RNA (at 0.9μg/μl) at 94°C for 40 s in 10μl 10X fragmentation buffer (100mM Tris-HCl and 100mM ZnCl2) in thin-walled PCR tubes in a pre-heated thermocycler block with the heated lid open. Ten microliters of 0.5M EDTA was added and the tubes were placed on ice. The RNA was then precipitated with sodium acetate and resuspended in 300μl RNase-free water. RNA fragment size was assessed by running 0.25μg RNA on a 2100 Bioanalyzer (Agilent) with the RNA Nano kit (Agilent). 2-5μg fragmented RNA was kept at -80°C as input. The RNA was denatured at 70°C for 5min and then put on ice. The IP mix was prepared as follows: fragmented poly-A-enriched RNA from cultured cells in 290μl, 10μl proteinase inhibitors (Roche), 5μl (200 units) RNasin® Ribonuclease Inhibitors (Promega), 5μl of 200mM Ribonucleoside Vanadyl Complex (RVC) (Sigma Aldrich), 100 μl 5X IP buffer (50mM Tris-HCl, 750mM NaCl, 0.5% (v/v) NP-40), 3.5μl anti-m^6A antibody (Synaptic System, 202003), and 86.5μl RNase-free water. The mix was incubated overnight at 4°C on a rotating wheel. The next day, 50μl Dynabeads™ Protein G (Invitrogen) were washed twice with 1x IP buffer supplemented with antiproteases (Roche) and blocked by incubating the beads for 1h on a rotating wheel in washing buffer supplemented with 0.5mg/ml BSA. The beads were washed again twice, added to the IP mix, and incubated for 2 h at 4°C on a rotating wheel. The beads were washed three times with 1 ml washing buffer supplemented with 10μl RNasin® and 10μl RVC. Elution was performed by TriPure (Roche) extraction and RNA was resuspended in 9μl RNase-free water. A sequence library was prepared with the SMARTer® Stranded Total RNA-seq Kit v2 - Pico Input Mammalian (Takara) for both input and IP samples. Samples were sequenced with the Illumina NextSeq500.

Infinium Methylation array

Genomic DNA was extracted with the QIAamp DNA Mini Kit (Qiagen) according to the manufacturer's protocol. Infinium MethylationEPIC Array Service was provided by Diagenode. DNA methylation was analyzed on Infinium MethylationEPIC or MouseMethylation bead arrays as previously described.[92] Briefly, the EZ DNA Methylation Kit (Zymo Research) was used for conversion of genomic DNA (300–800ng) with sodium bisulfite, and methylation assays were performed with 4μl converted DNA at 50ng/ml, according to the manufacturer's protocol. Raw methylation array data were submitted to the NCBI's Gene Expression Omnibus (GEO) database.

SLAM-seq

Nascent transcript formation was measured with the SLAM–seq Kinetics Kit–Anabolic Kinetics Module (Lexogen) and SLAMseq Metabolic RNA labelling experiments were performed by Isogen Life Science. In brief, WT or Dnmt1 KO ESCs were incubated with 265μM 4SU for 2 hours before collection in the dark. For Mettl3 inhibitor treatment, WT ESCs were treated with 50μM STM-2457 or vehicle for 24h, with addition of 4SU to the medium at 265μM for the last 2 hours of treatment. For each clonal line, a negative control with no 4SU incubation was included for detection of T-to-C SNP variants (cf. SLAM-seq data analysis). RNA was then extracted with TriPure (Roche), according to the instructions of the SLAM–seq Kit (Lexogen). Alkylation of incorporated S4U nucleotides was performed from 4μg labeled RNA. A sequencing library was prepared from 200 ng converted RNA with the QuantSeq 3' mRNA-seq V2 Library Prep Kit with UDI (Lexogen) and sequenced on the Illumina NextSeq 2000 platform in SR100 mode.

RNA stability assay by actinomycin D treatment

WT and Mettl14 KO ESCs were treated with 5μg/ml actinomycin-D (Sigma) or vehicle for 0, 2, 4, 8 hours. Likewise, WT and METTL3 KO HeLa cells were treated with 1μg/ml actinomycin D or vehicle for 0, 4, 6, and 8 hours. Cells were collected and RNA was extracted with the RNeasy Kit (Qiagen) according to the manufacturer's instructions. Sequencing libraries were then prepared with TruSeq Stranded Total RNA Library Prep Gold (96 Samples) as described in the "RNA-seq" section, starting from 200 ng total RNA.

Polysome profiling

Polysome profiling was done by previously reported methods[93] with some modifications. Five 15-cm plates each of METTL3 KO and WT HeLa cells were prepared as described in the "cell lines" section. Fifteen minutes before harvest, 100μg/ml cycloheximide (CHX) (Sigma) was added to the medium. Cells were washed twice with ice-cold PBS supplemented with 100μg/ml CHX, scraped, and centrifuged at 4°C (500g for 5 minutes). Cell pellets were resuspended in 500μl lysis buffer (20mM Tris pH 7.4, 100mM KCl, 5mM MgCl2, 100μg/ml CHX, 1% Triton X- 100, supplemented with cOmplete™ Mini Protease Inhibitor Cocktail (Roche) and 40U RNase Inhibitor (Promega)), incubated at 4°C for 20 minutes, and centrifuged (13000g for 20 minutes). The supernatant was treated with the RNase-Free DNase Set (Qiagen) according to the manufacturer's protocol and then centrifuged at 4°C (13,000g for 15 minutes). The A260 absorbance of each sample was measured to adjust the RNA amount to 300μg. A 10–50% w/v sucrose gradient was prepared for each sample in lysis buffer without Triton X-100 and adjusted lysates were loaded onto the sucrose gradient and centrifuged at 4°C (190,000g for 90 minutes, Beckman, rotor SW41Ti). The gradients were then fractionated into 0.4-ml fractions with an ISCO Density Gradient Fractionation system at 1ml/min speed. The A254 absorbance of each fraction was measured by the optical unit of the fractionating system. Fractions corresponding to non-polysomes (free RNA, 40S, 60S, and 80S) and polysomes were collected. RNA was extracted with TRIzol LS (Invitrogen) and purified with lithium chloride (LiCl) precipitation solution (Invitrogen) according to the manufacturer's protocols. For sequencing, the 40S, 60S, and 80S fractions were pooled into a single sub-polysome fraction called the "monosome fraction". cDNA libraries from the sub-polysome and polysome fractions were prepared and sequenced as previously described.

Precision run-on and sequencing (PRO-seq)

PRO-seq experiments were performed and analyzed as described previously.[65,66,94] Briefly, nuclear run-on assays were performed on 10×10^6 ESCs nuclei combined with 0.5×10^6 spike in Drosophila S2 cell nuclei. The mixture was incubated for 3 minutes at 30°C with 25μM Biotin-11-ATP/UTP/CTP/GTP (PerkinElmer). After this, total RNA was extracted and fragmented in 0.2M NaOH for 10 minutes on ice. Biotinylated nascent RNAs were then purified on M-280 streptavidin beads (Invitrogen). Enzymatic steps were conducted with RppH (NEB) and PNK (NEB) to remove the 5' cap, repair the triphosphate, and repair the 5' hydroxyl ends. Adapter ligation and reverse transcription were performed with SuperScript III (Invitrogen), followed by PCR amplification. Libraries were size-selected with AMpure XP (Beckman Coulter #A63882) and sequencing was done on a NovaSeq 6000 (Illumina) platform with single-read runs.

QUANTIFICATION AND STATISTICAL ANALYSIS

Sequencing & array data analysis

Pre-processing of sequencing data

Sequencing data from m^{6}A-seq, polysome-seq, ChIP-seq, and RNA-seq were pre-processed as follows. First, the raw sequencing data were analyzed with FastQC (v0.11.5).[95] Low-complexity reads were removed with the AfterQC tool (v0.9.6)[96] using default parameters. For RNA data (m^{6}A-seq, polysome-seq, ChIP-seq, and RNA-seq), reads were mapped to human tRNA and rRNA sequences with Bowtie2 (v2.3.4.1)[97,98] to exclude reads originating from rRNA or tRNA. The rRNA and tRNA sequences were downloaded from https://www.ncbi.nlm.nih.gov/nuccore using "Homo sapiens"[Organism] (for HeLa cells) or "Mus musculus"[Organism] (for ESCs and EBs) AND (biomol_rrna [PROP] OR biomol_trna [PROP] as search parameters. Reads that did not map to tRNA or rRNA sequences and ChIP-seq reads were further processed with Trimmomatic (v0.33)[98] using default parameters to remove adapter sequences. The resulting fastq data were again analyzed with FastQC to ensure that no further processing was needed.

m^{6}A-seq data analysis

Pre-processed reads (cf. previous section) from HeLa cells were mapped against the human reference genome (GRCh37/hg19) with the STAR algorithm (v2.6.1d)[99] using the reference transcriptome based on Ensembl (v85)[100] and LNCipedia (v5.2)[101] (referred to hereafter as Ensembl+LNCipedia) in single-end mode (HeLa cells). Pre-processed reads (cf. previous section) from ESCs and EBs were mapped against the mouse reference genome (GRCm38/mm10), also using the STAR algorithm (v2.6.1d) in single-end mode. The reference transcriptome based on Ensembl (v99) was used as reference transcriptome (referred to hereafter as mouse Ensembl). Gene expression was evaluated on the basis of HTseq counts (v0.9.1)[102] of input samples. m^{6}A sites were identified from IP samples with the m6aViewer peak-calling tool (v1.6.1),[103] using the input to estimate background noise. Sites showing significant enrichment over input in all replicates (per condition) and present in genes showing an expression level of at least 1TPM were considered for further analysis. For visual representations of local enrichment profiles, HPB normalized coverage profiles were generated with the bamTobw tool (https://github.com/YangLab/bamTobw)[104] and uploaded into the IGV tool (v2.9.4).[105]

Differential analysis of m^{6}A sites was performed as previously published.[52] Briefly, the m^{6}A counts provided by m6aViewer were first imported into R and adjusted for changes in gene expression by dividing values by the ratio input$_{sample}$ / input$_{control}$ of the corresponding transcript in the inputs (cf. RNA-seq data analysis). Then differential analysis was performed with edgeR (v3.42.2),[106] with the normalized m^{6}A levels being protected from further re-scaling by fixing the library size for all samples as lib.size = rep(10̂6, X) in the voom function (with X being the number of samples in the cohort). Principal component analysis (PCA) was performed from normalized m^{6}A counts in ESCs and EBs to estimate variability between biological replicates. The threshold for significant differential m^{6}A was set at corrected $p < 0.05$ and an absolute fold change >1.5.

m^6A-seq data annotation

The association of m^6A sites with transcripts (isoform level) was performed with the m6aViewer tool (v1.6.1)[103] on the basis of the reference transcriptome used for read mapping (Ensembl+LNCipedia for HeLa and mouse Ensembl for EBs). Each m^6A site was assigned to a transcript region by intersecting its chromosomal position with the regions defined in the section "Infinium array reannotation". To identify the regions richest in m^6A, the distribution of m^6A sites across transcript regions was computed as percentages.

RNA-seq data analysis

RNA-seq data were pre-processed/analyzed as described under 'Pre-processing of sequencing data', then analyzed with DESeq2 (v1.22.2).[107] For differential expression of RNA-seq data, pre-processed data (cf. previous section) were then mapped to the human transcriptome (GRCh37/hg19) with the RSEM tool (v1.3.1)[108] using Ensembl+LNCipedia reference transcriptome and converted to BAM with SAMtools (v1.6.2).[109] The 'expected read counts' were submitted with the tximport package (v1.10.1).[110] Under conditions where m^6A-seq was performed, the input samples were used for RNA-seq analysis, as mentioned in the legends. In those cases, m^6A input data were pre-processed/analyzed as described under "Pre-processing of sequencing data" and "m^6A-seq data analysis"[108–110]. Then differential analysis was performed with edgeR (v3.42.2).

Infinium methylation array data analysis

Raw Infinium MethylationEPIC data (HeLa cells) and MouseMethylation data (ESCs and EBs) were pre-processed according to published guidelines[111]: CpG probes of low quality (detection p-value threshold: 0.05) were removed from the analysis. Additionally, Infinium MethylationEPIC probes targeting methylation sites located on the X- and Y-chromosomes or at common single-nucleotide polymorphisms and cross-reactive probes (i.e. targeting several genomic locations) were filtered out on the basis of the extended annotation of McCartney et al.[112] β-values were computed with the following formula: β-value = M/[U+M], where M and U are the raw "methylated" and "unmethylated" signals, respectively. β-values were corrected for type I and type II bias with the peak-based correction.[113] For HeLa data, technical triplicates of each biological replicate were merged into one metasample, using the median β-value of each probe. Principal component analysis (PCA) was performed on the basis of the 2,070 most variant CpGs (standard-deviation > 0.29) in WT and METTL3 KO HeLa cells to estimate variability between biological replicates. For differential analysis between METTL3 KO and WT cells, the obtained median β-values were converted to M-values and p-values were computed with Student's t-test. Then the Benjamini-Hochberg multi-testing correction was applied and probes showing a corrected p-value < 0.05 and a $\Delta\beta > 0.2$ were defined as significant.

For visual representations, Infinium coordinates in hg19 (HeLa) or mm10 (ESCs and EBs) were converted to wig files, using the median β-value of the biological triplicates as coverage feature. To improve visualization, the coordinates were extended to 40 bp and overlapping coordinates were slightly shifted downstream to remain visible. The resulting wig files were uploaded into the IGV tool (v2.9.4).[105]

Infinium array reannotation

For Infinium MethylationEPIC array reannotation, long noncoding transcript positions were obtained from the LNCipedia website ('lncipedia_5_2_hc_hg38.bed') and other transcript positions were obtained from Gencode (v28).[114] For Infinium MouseMethylation reannotation, transcripts from Gencode (vM25) were used. Within the genome, "promoters" and "gene-bodies" were defined, respectively, as the regions located from 250 bp upstream to 250 bp downstream of the transcription start site (TSS) and from 250 bp upstream-250 bp downstream of the TSS to the transcription termination site (TTS). The "gene-body" region was further subdivided into four regions corresponding to those distinguished in transcripts: a "stop" region extending 500 bp upstream and downstream from the stop codon, introns excluded, a "5' UTR" preceding the start codon, a "CDS region" between the two previous ones, and a "3'UTR" downstream of the stop codon. Gene-bodies of noncoding genes were excluded. Note that when the "promoter" region is discussed in relation to a transcript region, it is called "TSS". Infinium MethylationEPIC chromosome positions in hg19 (from Illumina annotation file vB4) were converted to hg38 with the liftOver tool,[115] while Infinium MouseMethylation chromosome positions were obtained in GRCm38/mm10 from Illumina annotation file (v1.0 A1 GS Manifest file). Infinium positions were finally overlapped with the aforementioned regions (TSS, 5'UTR, CDS, Stop, 3'UTR).

CpG Island annotation

CpG Island (CGI) positions were obtained for the hg19 human genome build from UCSC Table Browser (downloaded on June 2023). CGI positions were then overlapped with the 'Ensembl+LNCipedia' transcript positions with bedtools intersect (v2.25.0).[116] Finally, each gene presenting at least one CGI more than 1.5 kb from its TSS was considered to have a gene-body CGI.

ChIP-seq analysis

Dnmt1[87] (GSM2059182) and Dnmt3b[15] (GSE72856) ChIP-seq data in ES cells were downloaded from the GEO website as raw data (fastq) and re-analyzed. Pre-processed data (cf. previous section) were aligned to the genome (GRCh37/hg19) with Bowtie2 (v2.3.4.1) and SAMtools (v1.6.2) was used to convert the output file to the BAM format. Duplicates were removed with Picard Tools (v2.20.4). Peaks were called with MACS2 (v2.1.1), with IP or IgG as test and INPUT as control, and only default parameters were used. Peaks overlapping with IgG peaks, on the basis of Bedtools merge (v2.25.0), were filtered out. Only reproducible peaks based on Bedtools merge were used for further analysis. Bigwig files were generated from BAM files using deepTools (v3.5.4)[117] with bamCoverage. Visualization was performed with computeMatrix followed by plotProfile or plotHeatmap, with deepTools.

Polysome-seq data analysis

Pre-processing was performed as previously described (cf. RNA-seq data analysis section). Counts were imported into R and transcripts containing "lnc-", "_" or "_AS" were filtered out to limit sources of non-coding transcripts. Then differential analysis was performed with edgeR (v3.42.2), with the parameter normalize set at "quantile" in the voom function. To account for changes in expression, the polysome fractions were normalized to the sub-polysome fraction by defining the contrast in the makeContrasts function as '(groupM3KO.poly - groupM3KO.sub) - (groupWT.poly - groupWT.sub)'.

RNA stability-assay analysis

Pre-processing was performed as previously described (cf. m6A-seq data analysis section). Expression values from WT and Mettl14 KO ESCs were then fitted to an exponential decay model by linear regression in R, as previously described.[52] Only genes with reliable regressions (half-life > 1 hour in at least one condition and absolute correlation coefficient > 0.5 for the regression) were used for further analysis. For stability data in WT and Mettl3 KO ESCs, half-life values were obtained from puclic data[61] (GSE86336), downloaded as a processed data table on GEO, and the m^{6}A status of transcripts was derived from our in-house m^{6}A-seq data (this study).

SLAM-seq data analysis

SLAM-seq analyses were performed following a previously established protocol,[57] using the SLAMdunk pipeline (v0.4.3).[58] Briefly, reads were trimmed and mapped to the mouse genome (mm10) with NextGenMap, which accepts multiple mismatches. Reads were filtered to keep those with unique 3'UTR alignments. T-to-C SNPs were excluded (using 'no 4SU negative controls' as background). Total and T-to-C conversion counts were generated for each 3'UTR transcript region. The 3′ UTR counts were then imported into R and analyzed with edgeR (v3.42.2) for differential analysis. Total counts were used for steady-state expression analysis. For nascent RNAs, the conversion counts were normalized to total counts for nascent RNAs. The threshold for significant differential expression was set at corrected $p < 0.05$ and absolute fold change >1.5.

To assess post-transcriptional regulation using SLAM-seq data, we then compared RNA fold changes of steady-state gene expression and nascent RNA regulation. This method was adapted from a previously established protocol using exonic and intronic reads in RNA-seq as proxy for steady-state and nascent RNA regulation, respectively.[52,118]

PRO-seq data analysis

The raw fastq data were trimmed with Cutadapt (v1.14) and Trimmomatic (v0.33)[98,119] and then aligned with either the mm10 or dm3 genome using bowtie2.[120] The strand-specific single nucleotide ends of aligned reads were constructed using BEDTools with genomecov.[116] Bedgraph data were normalized to the number of reads mapped to the spike-in dm3 genome before being converted into bigwig data for further analysis. Bigwig files were then averaged for each condition with deepTools using bigwigCompare, with –operation set at 'mean'. Visualization was performed with computeMatrix and plotProfile from deepTools.

Data integration

5mC and m^{6}A data integration in WT cells

To investigate the relationship between 5mC and m^{6}A in WT cells, 5mC and m^{6}A levels at corresponding sites were summarized, respectively, using the median of the β-value and $\log_2$ fold enrichment across biological replicates. Four complementary approaches were used:

1. In the "transcript-centric" analysis, transcripts (found at > 1 TPM) were classified as 'm^{6}A marked' or 'non m^{6}A marked' according to whether at least one isoform was modified with at least one m^{6}A or not. Then the numbers of 5mC-modified (β-value > 0.25) Infinium probes corresponding to 'm^{6}A marked' and 'not m^{6}A marked' transcripts were determined, and these categories were further broken down according to whether the Infinium probe was located in the promoter or the gene-body.
2. In the "transcript-gene-body-centric" analysis, transcript gene bodies (from transcripts found at > 1 TPM and presenting at least one Infinium probe) were classified as 'm^{6}A marked' or 'non m^{6}A marked' according to whether or not at least one isoform was modified in its gene-body with at least one m^{6}A. For each transcript, the longest isoform was selected as a representative of the transcript and the mean 5mC level was computed across the gene-body of that isoform. Transcript gene bodies were then stratified as '5mC-modified' (β-value > 0.25) or 'non 5mC modified'. Finally, transcript stratification was overlapped according to m^{6}A and 5mC marking. The list of stratified transcripts is available in Table S1.
3. In the "region-centric" analysis, the different regions (TSS, 5'UTR, CDS, Stop, 3'UTR) of transcripts (found at > 1 TPM) were classified as 'm^{6}A marked' or 'non m^{6}A marked' depending on whether at least one isoform was modified with at least one m^{6}A in that region (note that m^{6}A could also be present in another region of the same transcript). Infinium probes were then classified as 'm^{6}A associated' or 'not m^{6}A associated' depending on the presence of m^{6}A in the same region of the corresponding transcript. The relationship between 5mC and m^{6}A was then investigated in three ways:
    - i Infinium probes were grouped into four bins of increasing β-value (0-0.25, 0.25-0.5, 0,5-0.75, 0.75-1). For each bin, the percentage of probes associated with m^{6}A was computed by means of a bootstrap approach: random selection of 10% of the probes followed by binning and percentage computation was repeated one hundred times to robustly evaluate the association between the 5mC level and the percentage of m^{6}A-associated CpGs.
    - ii For each transcriptomic region, the percentage of Infinium probes that were 5mC modified (β-value > 0.25) and m^{6}A associated was computed.
    - iii For each transcriptomic region, Infinium probes were grouped into 1000 bins of increasing β-value and for each bin the number of probes associated with m^{6}A was determined, to visualize the correlation between the 5mC level and m^{6}A presence.

Integration of 5mC, m6A, and other sequencing data in WT & KO cells

Transcripts identified as "m^6A-marked" (cf. "transcript-gene-body-centric" analysis) were overlapped with transcripts corresponding to "5mC-marked" genes (average gene-body β-value > 0.25). These genes are commonly referred to as "5mC-m^6A targets" througout the study. The annotation described under 'Infinium array reannotation' was used to associate genes with Infinium probes.

When focusing on 5mC, genes having at least one Infinium probe in the gene-body were selected. Unless otherwise stated, genes with at least one probe with $\Delta\beta < -0.1$ in the differential 5mC analysis between METTL3 KO and WT cells were considered to be "METTL3-dependent" for DNA methylation.

Whole Genome Bisulfite Sequencing (WGBS)

Parental and METTL3 KO WGBS data for mouse ESCs[31] (GSE126239) were downloaded as processed data (CG.meth.txt and CpG_report.txt files respectively) from GEO (https://www.ncbi.nlm.nih.gov/geo/). Sites with less than 10-read coverage were filtered out. When methylation values were available for both strands for the same CpG site, the values were averaged if the two values were similar (absolute $\Delta\beta < 0.2$) and discarded otherwise. Sites for which at least one methylation site per condition was available were kept. For each site, Δβ was computed as the difference between the mean (or unique) values for METTL3 KO and WT cells.

WGBS data annotation

Each WGBS site was assigned to a transcript region by intersecting, with bedtools intersect (v2.25.0),[116] its chromosomal position with the promoter and gene-body regions defined in the section "Infinium array reannotation".

Additionally, repeated regions for the mm10 genome build were downloaded from the repeatMasker database with Table Browser from the UCSC website (https://genome.ucsc.edu/cgi-bin/hgTables) (downloaded on the 2024-01-17). For simplicity, the repeated regions were re-defined as follows:

1- 'repFamily' was used as main criterion
2- Families with less than 1000 occurrences and the family 'Unknown' were grouped under the term 'Other'.
3- The multiple 'hAT' families were regrouped under a single term, as were the 'TcMar' families
4- For better comparison with Xu et al.,[31] the ERVK family was refined into IAPEz and non-IAPEz ERVK by means of the "repName"

The mm10 repetitive regions obtained were then overlapped with the WGBS sites with bedtools intersect (v2.25.0).[116]

Finally, WGBS sites overlapping simultaneously with a repeated region and a promoters or gene-body were excluded.

Integration of public Mettl14 and H3K36me3 ChIP-seq data

For comparison of public Mettl14[35] and H3K36me3[55] ChIP-seq data (GSE206730, GSE31039), bigwig files were directly downloaded from the GEO website (https://www.ncbi.nlm.nih.gov/geo/). H3K36me3 having been aligned with mouse genome mm9, the genomic locations of relevant bed files (e.g. Mettl3-dependent 5mC sites or Dnmt3b ChIP-seq peaks) were lifted from mm10 to mm9 by means of the 'liftOver' tool.[115] Scores for each genomic region were then computed with computeMatrix from deepTools (v3.5.4) and the matrices were imported into R. The signal was first averaged per bin and per condition. Then, to correct for differences in analysis methods between the two datasets, the signal was normalized to local background by adjusting each condition's signal relatively to the mean signal of the outermost 10% bins at the 5' and 3' ends of the windows.

Integration of data from ESCs and EBs

For 5mC, when β-values are utilized, data were processed as previously described (cf. Infinium methylation array data analysis section) with no additional normalization. To mitigate batch effects between the 'Mettl3' and 'Mettl14' datasets and between ESCs and EBs, integration of the 5mC data involved separate normalization for each experimental set. Within each batch (i.e. ES Mettl3, EB Mettl3, ES Mettl14, and EB Mettl14), the data underwent z-score transformation for the whole batch (including WT, KO, and rescued cells when relevant). Then, the normalized data were averaged per condition. ES data from the Mettl3 and Mettl14 KO batches were merged together, as were EB data from both batches. To establish baseline values, WT cells from the Mettl3 and Mettl14 batches were averaged as one unified "WT" signal (separately for ES and EB) for downstream analysis.

For RNA-seq data, as with 5mC, the datasets were first segregated into ESCs and EBs for each batch (Mettl3 or Mettl14). The data were then normalized using z-score transformation within each batch (including WT, KO, and rescued cells when applicable). We then merged the two EB batches and performed hierarchical clustering using average linkage. GSEA was carried out with the fGSEA package (v.1.26.0),[121] with genes pre-ranked by $\log_2$ fold change from the differential analysis. Gene set collections were downloaded from the Molecular Signatures Database (v.7.5.1; http://www.gsea-msigdb.org/gsea/msigdb/index.jsp).

Statistical analysis

Statistical significance was calculated with Student's *t*-test, the Wilcoxon rank-sum test, the Pearson or Spearman correlation test, the hypergeometric distribution test, the chi-squared test, the Kolmogorov-Smirnov test, ANOVA, or the linear regression test with interaction, with the type of test (paired or unpaired, one-sided or two-sided) specified in the corresponding legend. When required, correction for multiple testing was applied by means of the Benjamini-Hochberg method or FDR, as indicated. The criterion for statistical significance was *p*-value (or corrected *p*-value) < 0.05. No statistical method was used to predetermine sample size. Unless otherwise stated, error bars in the graphical data represent means ± standard error of the mean or median and interquartile range

(IQR), and boxplots present medians as center lines, with box limits representing the upper and lower quartiles and whiskers representing 1.5×IQR. All sequencing and Infinium array data were generated from three independent experiments, except for the m^6A-seq data for METTL3-KO, which was generated from two replicates. Statistical details of experiments can be found in the figure legends. Statistical analyses were performed with Graphpad Prism version 7 or R version 4.2.2. Schemes were created with BioRender.com.

Supplemental figures

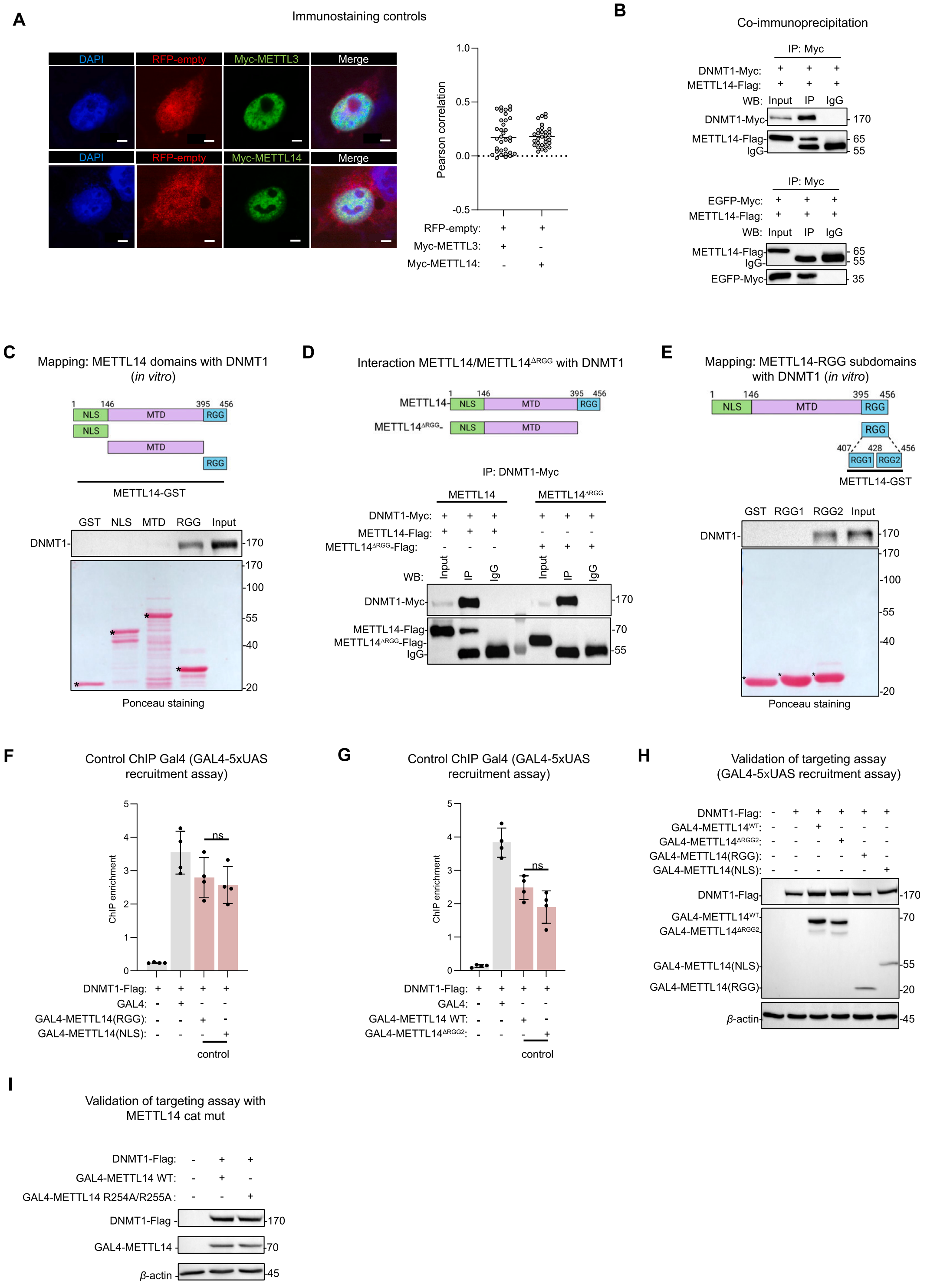

(legend on next page)

Figure S1. METTL3-METTL14 recruit the DNA methyltransferase DNMT1 to chromatin, related to Figure 1

(A) Immunostaining of COS-7 cells transfected with Myc-METTL3 or Myc-METTL14 (green) and empty RFP vector (red), as negative controls of Figure 1B. Scale bars, 5 μm, median as horizontal bar.

(B) METTL14-FLAG interacts with DNMT1-Myc by co-immunoprecipitation in transiently expressing HeLa cells (*n* = 3). EGFP-Myc as negative control.

(C) Schematic illustration of METTL14 domains (top) and pull-down of GST-tagged METTL14 domains with recombinant FLAG/His-tagged DNMT1 (bottom). Asterisks mark METTL14 domains. (*n* = 3).

(D) CoIP in transiently transfected HeLa cells indicates that DNMT1-Myc interacts with full-length METTL14-FLAG, but not with METTL14-ΔRGG-FLAG. (*n* = 3).

(E) Schematic of the METTL14 RGG1 and RGG2 subdomains (top) and pull-down showing interaction between GST-tagged RGG2 and recombinant FLAG/His-tagged DNMT1 (bottom). Asterisks mark the RGG subdomains (*n* = 3).

(F and G) The GAL4-METTL14 fusion constructs used in Figures 1F and 1G display similar chromatin binding by GAL4 ChIP-qPCR. Two-tailed unpaired t test (ns, non-significant).

(H and I) Expression of the GAL4-tagged constructs and FLAG-tagged DNMT1 in HEK2935XUAS cells, as used in GAL4-5XUAS recruitment assays (related to Figures 1F, 1G, and 1I).

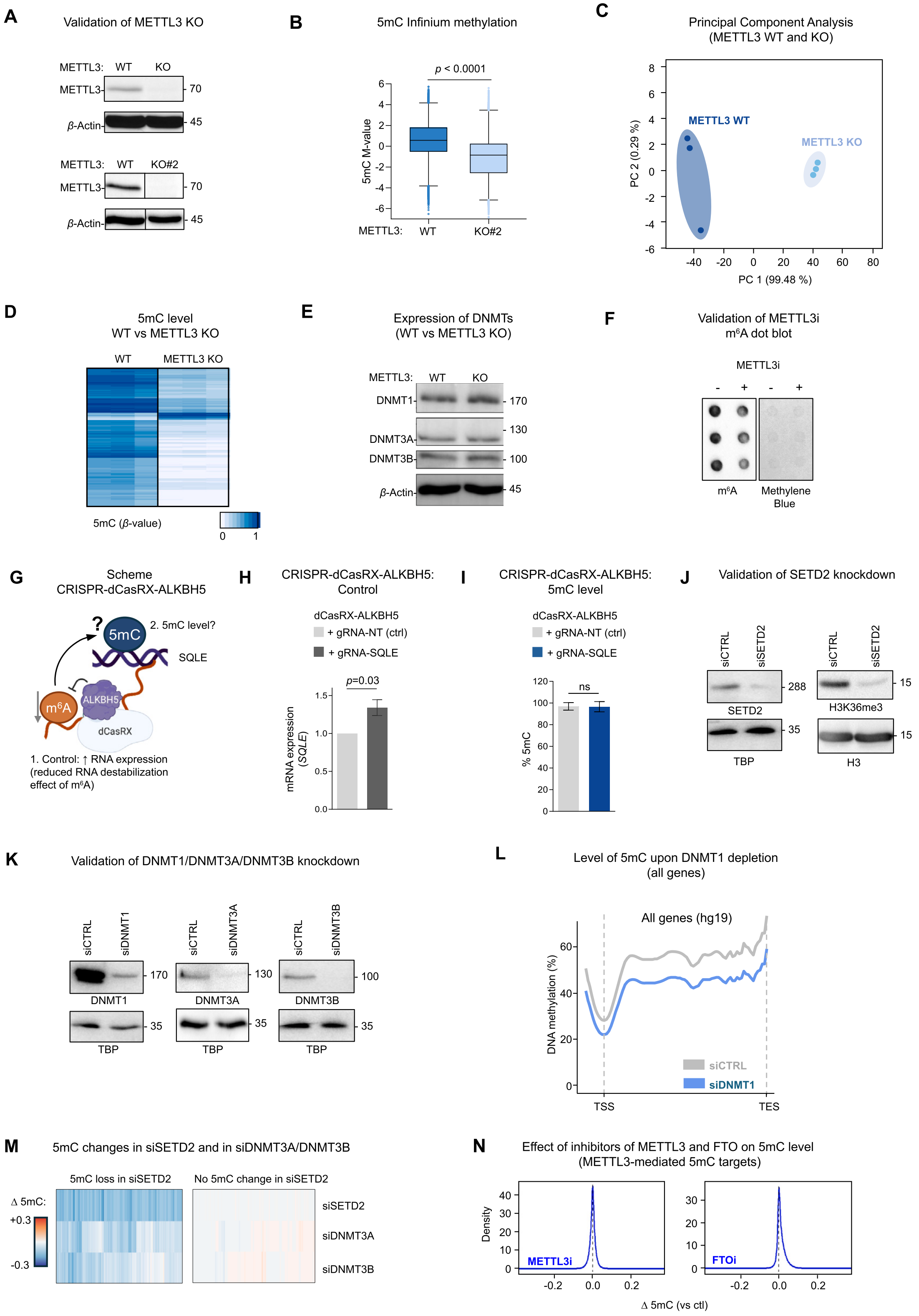

Figure S2. METTL3 promotes DNMT1-dependent gene-body 5mC, related to Figure 2

(A) Validation of METTL3 knockout by western blotting in two independent HeLa cell clones ($n = 3$).

(B) Reduced DNA methylation in a second HeLa METTL3 KO clone ($n = 3$).

(legend continued on next page)

(C) Principal-component analysis (PCA) based on the 2,070 most variable CpGs in WT and METTL3 KO HeLa cells.

(D) Heatmap depicting the 5mC level of the 10,000 CpGs with the most variation ($\Delta\beta$) among WT and METTL3 KO HeLa cells.

(E) METTL3 KO does not affect the expression of DNA methyltransferases by western blotting (*n* = 3).

(F) Validation of reduced m^6A levels in HeLa cells treated with 25 μM STM-2457 by dot blotting (*n* = 3).

(G–I) Scheme representing targeted m^6A erasure by CRISPR-dCasRX-ALKBH5 (G). In HEK293T cells, targeting dCasRX-ALKBH5 to SQLE increased RNA levels (H, by RT-qPCR), as expected from the RNA-destabilizing effect of m^6A (H), but it did not affect local 5mC levels (I, by pyrosequencing). Data as means ± SEM (*n* = 3).

(J) Reduced levels of SETD2 (left) and H3K36me3 (right) in SETD2-knockdown HeLa cells (*n* = 3).

(K) Reduced levels of DNMT1, DNMT3A, and DNMT3B following knockdowns in HeLa cells (*n* = 3).

(L) Reduced CpG methylation across all genes in DNMT1-KD HeLa cells (*n* = 3).

(M) SETD2-dependent 5mC sites ($\Delta\beta \leq -0.1$ in SETD2-KD cells) are hypomethylated following depletion of DNMT3A or DNMT3B, whereas negative control sites ($|\Delta\beta| \leq 0.005$ in SETD2-KD cells) are globally unaffected.

(N) Differential 5mC levels ($\Delta\beta$) indicate that METTL3 (STM-2457) or FTO (FB23-2) inhibitors have little to no impact on METTL3-dependent sites.

p values by two-tailed t test (B, H, and I).

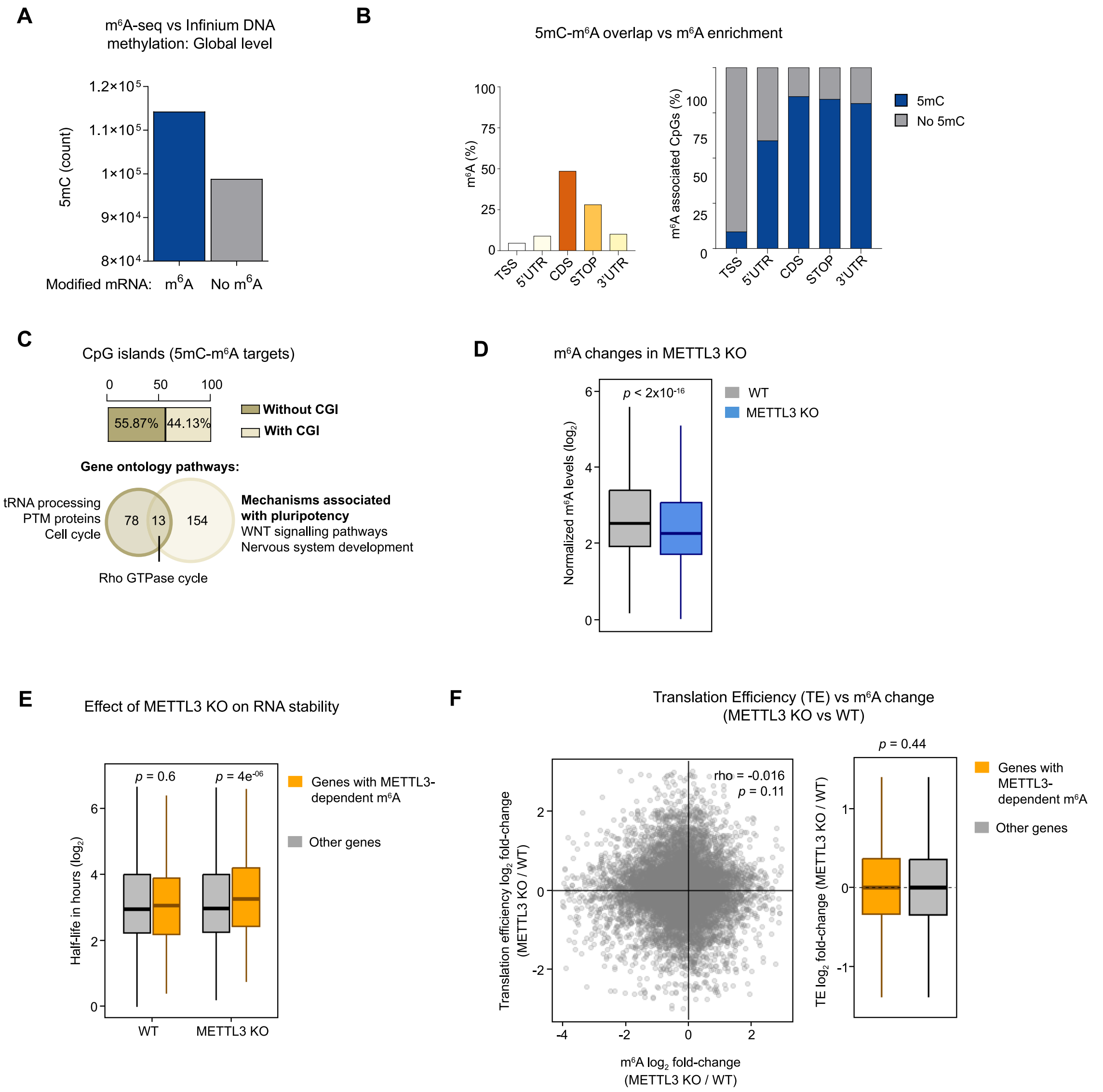

Figure S3. Both 5mC and m^{6}A fine-tune expression of common target genes, related to Figure 3

(A) Number of methylated CpGs associated with genes whose transcripts are either m^{6}A-marked or not in HeLa cells.

(B) Proportions of m^{6}A peaks in transcript regions (left) and percentage of 5mC-modified CpGs among those co-occurring with m^{6}A by transcript region (right). *p* values by hypergeometrical test: TSS = 1, 5′ UTR = 0.61, CDS = 1.13e−206, stop codon = 4.13e−81, and 3′UTR = 4.67e−3.

(C) Percentage of 5mC-m^{6}A target genes with or without intragenic CpG islands (CGI, top) and representative associated gene ontology pathways (bottom).

(D) METTL3 depletion globally reduces m^{6}A levels in HeLa cells ($n = 2$).

(E) METTL3-dependent m^{6}A-marked genes display increased transcript half-life in METTL3-depleted HeLa cells, as assessed by actinomycin D assay followed by RNA-seq ($n = 3$).

(F) Changes in m^{6}A do not correlate with changes in translation efficiency (TE, by polysome profiling sequencing) upon METTL3 depletion ($n = 3$). METTL3 dependency defined by a 1.5-fold decrease in m^{6}A level in METTL3 KO. Spearman correlation analysis (left).

p values by two-sided t test (D–F, right).

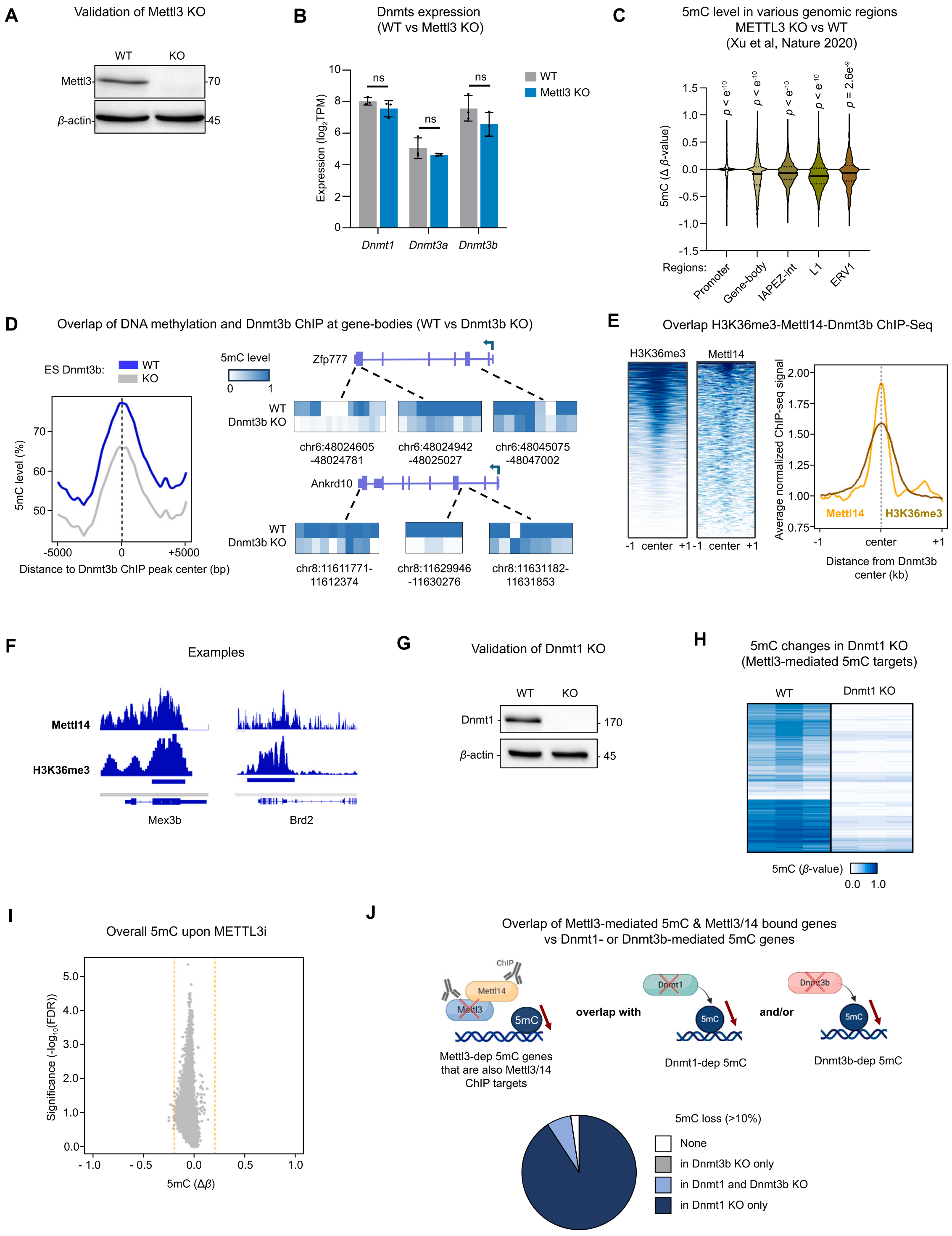

Figure S4. In ESCs, Mettl3-Mettl14 promote DNMT1-dependent gene-body 5mC, related to Figure 4

(A) Validation of Mettl3 knockout by western blotting in ESCs (*n* = 3).

(B) Mettl3 KO in ESCs does not affect the expression of DNA methyltransferases (Dnmt1, Dnmt3a, and Dnmt3b) by RNA-seq. Data as means ±SD (*n* = 3).

(C) Whole-genome bisulfite sequencing (WGBS) shows 5mC reduction in gene-body and intergenic regions in Mettl3-depleted ESCs. From published data (GEO: GSE126243).[31]

(D) Dnmt3b depletion in ESCs leads to DNA hypomethylation in regions identified as Dnmt3b targets by ChIP-seq. From published data (GEO: GSE72856).[15]

(legend continued on next page)

(E and F) H3K36me3 and Mettl14 ChIP-seq signals are enriched at Dnmt3b target regions (ChIP-seq peaks) in ESCs (E), with examples of ChIP-seq tracks (F). From published data (GEO: GSE72856, GSE206730, and GSE31039).[15,35,55]

(G) Validation of Dnmt1 knockout by western blotting in ESCs (n = 3).

(H) Global DNA hypomethylation observed among genes with Mettl3-dependent 5mC, following Dnmt1 depletion in ESCs.

(I) No significant changes in 5mC following Mettl3 inhibitor treatment (STM-2457) in ESCs (n = 3). Data plotted as in Figure 2E.

(J) Distribution of Mettl3-Mettl14 ChIP-seq targets (among genes with Mettl3-dependent 5mC deposition) based on their reliance on the catalytic activity of Dnmt1 and/or Dnmt3b in ESCs (5mC loss $\geq$10% upon Dnmt1 and/or Dnmt3b KO).

p values by two-sided t test (B and C).

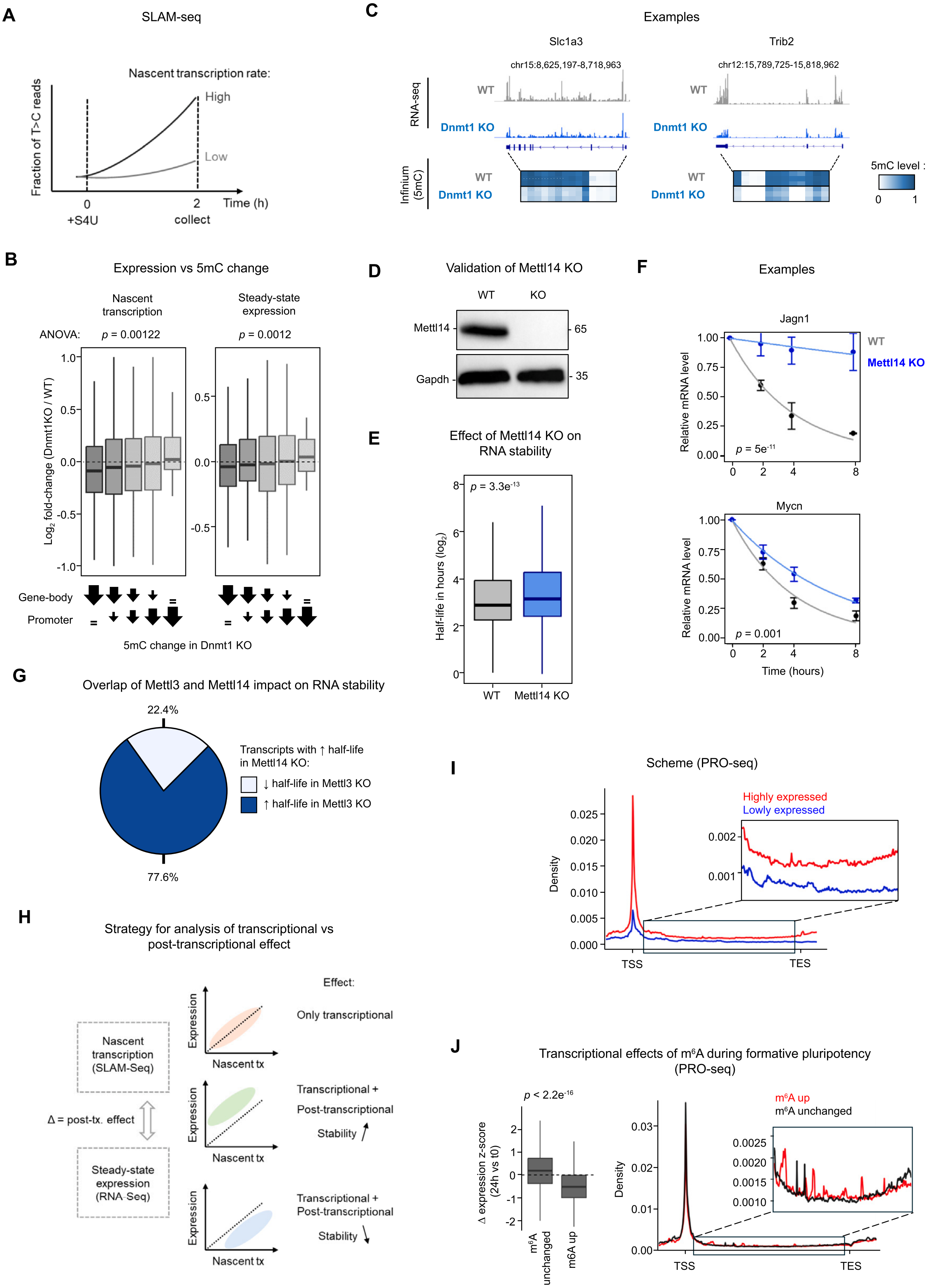
A
SLAM-seq
Nascent transcription rate:
High
Low
Fraction of T>C reads
0
+S4U
2
collect
Time (h)
C
Examples
Slc1a3
chr15:8,625,197-8,718,963
Trib2
chr12:15,789,725-15,818,962
RNA-seq
WT
Dnmt1 KO
Infinium (5mC)
5mC level :
0
1
B
Expression vs 5mC change
Nascent transcription
Steady-state expression
ANOVA:
p = 0.00122
p = 0.0012
Log2 fold-change (Dnmt1KO / WT)
1.0
0.5
0.0
-0.5
-1.0
Gene-body
Promoter
=
5mC change in Dnmt1 KO
D
Validation of Mettl14 KO
WT
KO
Mettl14
65
Gapdh
35
E
Effect of Mettl14 KO on RNA stability
p = 3.3e-13
Half-life in hours (log2)
8
6
4
2
0
WT
Mettl14 KO
F
Examples
Jagn1
Relative mRNA level
1.00
0.75
0.50
0.25
0.00
p = 5e-11
WT
Mettl14 KO
Mycn
p = 0.001
0
2
4
8
Time (hours)
G
Overlap of Mettl3 and Mettl14 impact on RNA stability
22.4%
77.6%
Transcripts with ↑ half-life in Mettl14 KO:
↓ half-life in Mettl3 KO
↑ half-life in Mettl3 KO
H
Strategy for analysis of transcriptional vs post-transcriptional effect
Effect:
Nascent transcription (SLAM-Seq)
Δ = post-tx. effect
Steady-state expression (RNA-Seq)
Expression
Nascent tx
Only transcriptional
Transcriptional + Post-transcriptional
Stability ↑
Transcriptional + Post-transcriptional
Stability ↓
I
Scheme (PRO-seq)
Highly expressed
Lowly expressed
Density
0.025
0.020
0.015
0.010
0.005
0.000
0.002
0.001
TSS
TES
J
Transcriptional effects of m6A during formative pluripotency (PRO-seq)
p < 2.2e-16
Δ expression z-score (24h vs t0)
2
1
0
-1
-2
m6A unchanged
m6A up
m6A up
m6A unchanged
Density
0.03
0.02
0.01
0.00
0.0025
0.0020
0.0015
0.0010
TSS
TES

Figure S5. Coordinated regulation of gene expression through 5mC transcriptional effect and m6A post-transcriptional effect in ESCs, related to Figure 5

(A) Schematic of nascent transcript measurement by SLAM-seq, using 4-thiouridine (S4U) incorporation into newly synthesized RNA and T-to-C chemical conversion.

(B) Changes in nascent and steady-state transcript levels upon Dnmt1 KO correlate with 5mC loss. Genes are grouped by the extent of 5mC loss in the gene-body ($\Delta\beta$ left to right: < -0.2, -0.2 to -0.15, -0.15 to -0.1, -0.1 to 0; >0) and promoter region ($\Delta\beta$ left to right: >0, 0 to -0.05, -0.05 to -0.1, -0.1 to -0.2, <-0.2).

(C) Example of genes with Mettl3-dependent 5mC that are downregulated (by RNA-seq) and hypomethylated (by 5mC Infinium) in Dnmt1 KO ESCs.

(D) Validation of Mettl14 knockout in ESCs by western blotting ($n = 3$).

(E–G) Depletion of Mettl14 globally increases RNA stability in ESCs (actinomycin D assay and RNA-seq, $n = 3$) (E), with representative transcripts (F), and this depletion has a post-transcriptional effect comparable to that seen in Mettl3 KO ESCs (G, from published data GEO: GSE86336).[61]

(H) Schematic of the strategy used in Figure 5I using SLAM-seq data. Linear correlation between nascent transcription (“nascent tx”) and steady-state transcript levels (“expression”) indicates transcriptional regulation, while deviations above or below the $x = y$ diagonal suggest post-transcriptional regulation (stabilizing or destabilizing effect, respectively).

(I) PRO-seq maps active transcription, as shown here in ESCs grown in 2i + LIF for highly and lowly expressed genes (>25 and 1–5 cpm, respectively, $n = 3$).

(J) Gain of m^6A (fold-change > 1.5) is associated with reduced gene expression at 24 h of formative pluripotency induction (left, by RNA-seq), with no concomitant change in active transcription (right, by PRO-seq).

p values by one-way ANOVA (B), two-sided t test (E and J), and linear regression (on $\log_2$ values) test (F).

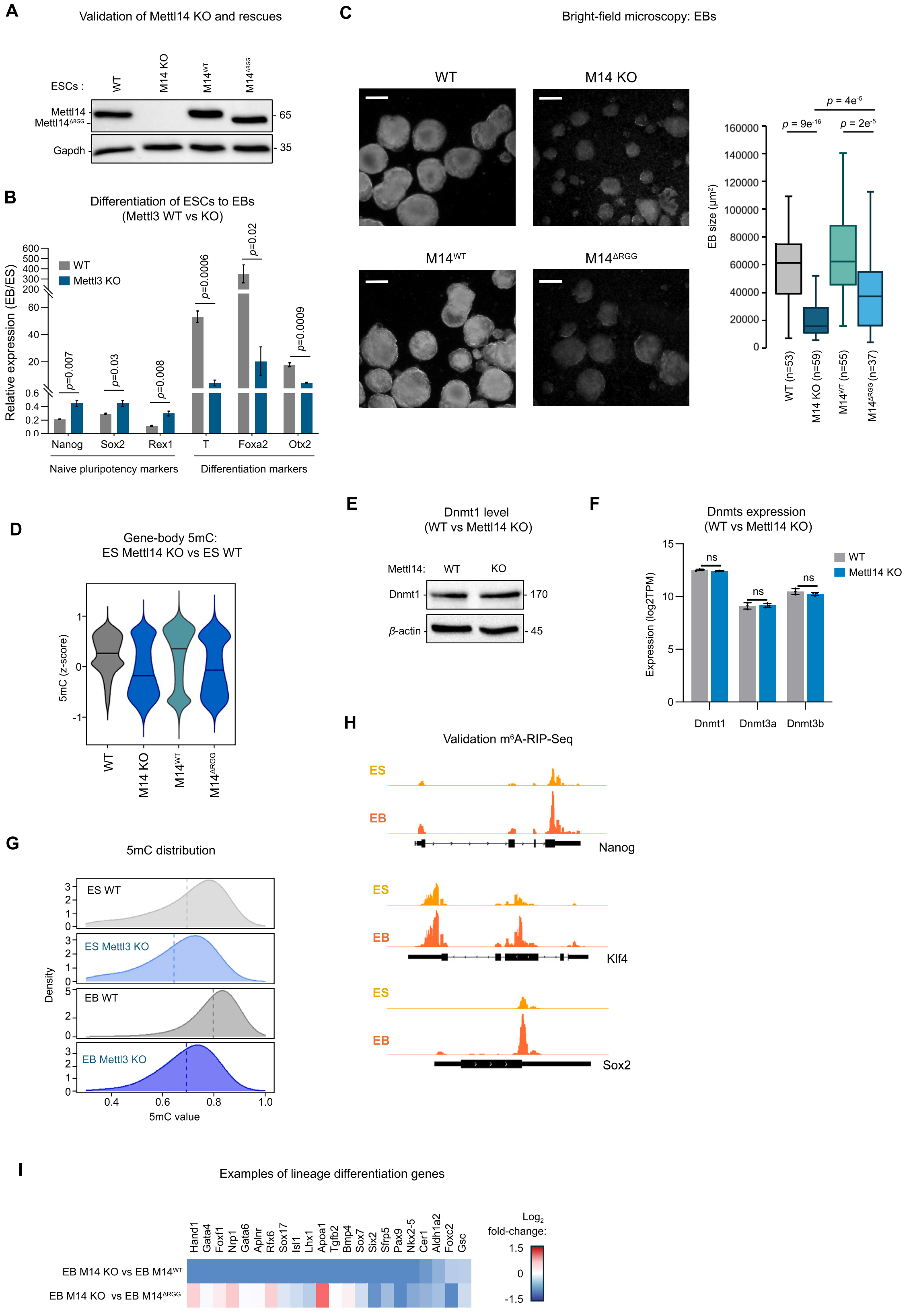

(legend on next page)

Figure S6. The role of both 5mC and m^{6}A during ES-to-EB differentiation, related to Figure 6

(A) Validation of Mettl14 KO and rescue with Mettl14^{WT} or Mettl14$^{\Delta RGG}$ in ESCs by western blotting ($n = 3$).

(B) Mettl3 KO EBs failed to upregulate the differentiation markers T, Foxa2, and Otx2 and to downregulate the pluripotency markers Nanog, Sox2, and Rex1. EB-to-ES ratio by RT-qPCR ($n = 3$).

(C) EB formation upon Mettl14 depletion is fully rescued by Mettl14^{WT} but only partially by Mettl14$^{\Delta RGG}$, as judged on the basis of EB size at day 8. Scale bar, 200 μm. Number of EBs (n) as indicated.

(D) Mettl14 KO reduces gene-body 5mC levels in ESCs, which is rescued by Mettl14^{WT} but not Mettl14$^{\Delta RGG}$ expression ($n = 3$).

(E and F) Mettl14 KO does not affect Dnmt1 protein levels, (E, by western blotting, $n = 2$) or transcript levels of the DNA methyltransferases Dnmt1, Dnmt3a, and Dnmt3b (F, by RNA-seq, $n = 3$).

(G) Mettl3 KO leads to global DNA hypomethylation in ESCs and EBs ($n = 3$). Group medians as dashed lines.

(H) Representative tracks with gain of m^{6}A upon exit from pluripotency, obtained for known target RNAs.

(I) Heatmap of key lineage differentiation genes (RNA-seq) showing that Mettl14$^{\Delta RGG}$ expression partially rescues differentiation of Mettl14 KO EBs.

Data as mean ± SEM (B) or means ±SD (F). p values by two-tailed t test (B, C, and F).

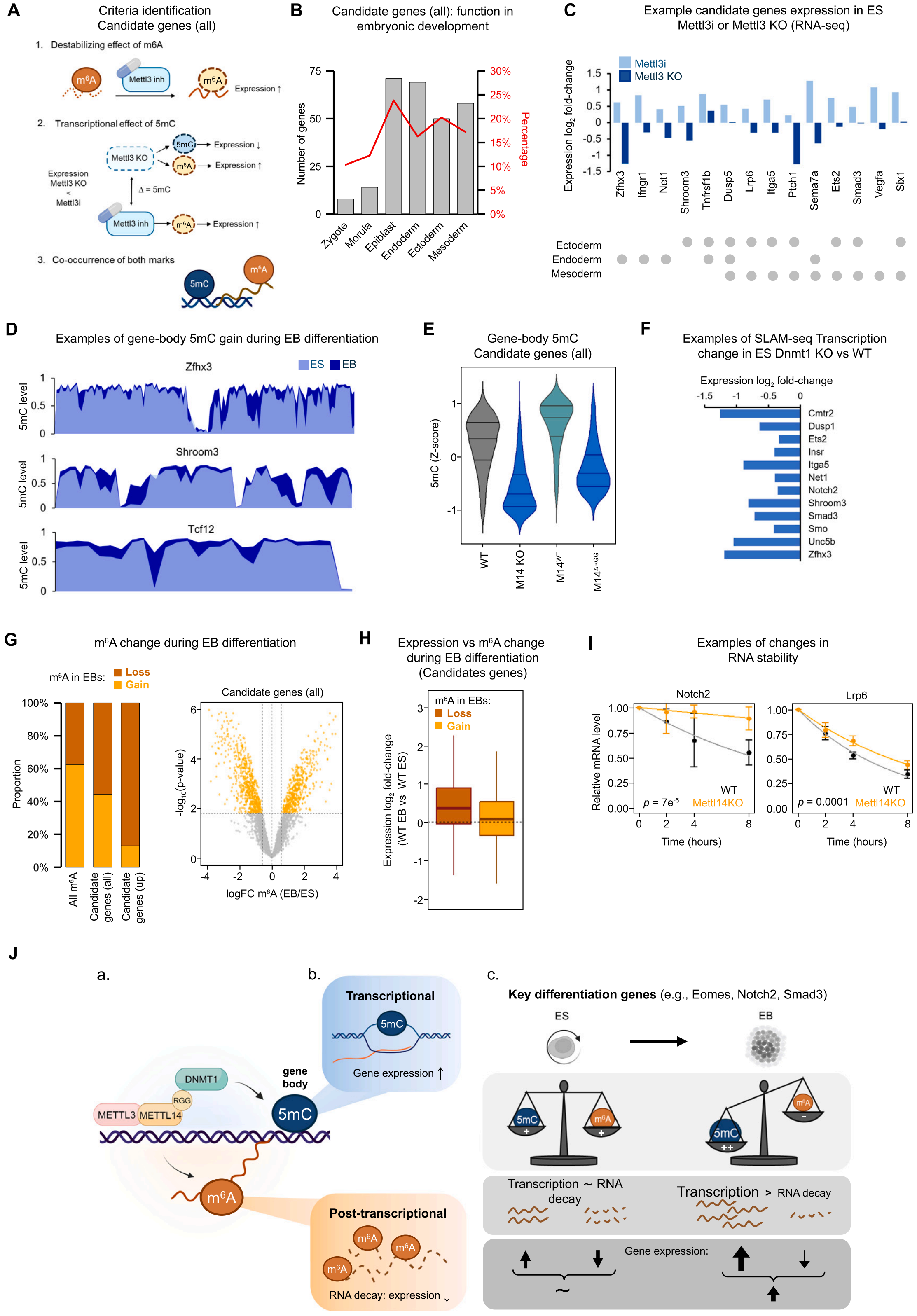

(legend on next page)

Figure S7. The dynamics of 5mC and m^{6}A regulate expression of key genes in differentiating ESCs, related to Figure 7

(A) Criteria for identifying candidate genes regulated by 5mC-m^{6}A in ESCs: (1) destabilizing m^{6}A effect (expression $\log_2$ fold-change > 0 in Mettl3i), (2) a transcriptional effect of 5mC, leading to lower expression upon Mettl3 KO (fold-change Mettl3 KO $<$ fold-change Mettl3i), and (3) co-occurrence of m^{6}A and gene-body 5mC (average $\beta \geq 0.25$).

(B) GO annotation for peri-implantation development among candidate genes. Gray bars represent gene counts (left y axis), and the red line shows percentage (right y axis) in each GO category.

(C) Divergent regulation of differentiation-involved candidate genes following Mettl3 inhibition or Mettl3 KO in ESCs by RNA-seq.

(D) Examples of candidate genes with an increased gene-body 5mC level during EB differentiation.

(E) Mettl14 KO reduces gene-body 5mC levels in candidate genes in EBs, and normal levels are rescued by Mettl14^{WT}, but not Mettl14$^{\Delta RGG}$ expression ($n = 3$).

(F) Examples of candidate genes showing, in ESCs, reduced nascent transcript formation following Dnmt1 depletion.

(G) Candidate genes display either gain or loss of m^{6}A during differentiation, with "up" candidate genes mainly losing m^{6}A.

(H) Relief from post-transcriptional downregulation through m^{6}A loss ($\log_2$ fold-change < 0) facilitates upregulation of candidate genes during EB differentiation.

(I) Examples of candidate genes with increased transcript stability following Mettl14 depletion in ESCs (actinomycin D assay). Linear regression (on $\log_2$ expression values) test with interaction.

(J) Schematic model of Mettl3-mediated DNA gene-body methylation and RNA methylation. (a) This study highlights that, aside from known RNA methylation mechanisms, Mettl3-Mettl14 recruits Dnmt1 to chromatin via the RGG domain to promote gene-body methylation. (b) On shared 5mC-m^{6}A targets, gene-body methylation promotes nascent transcription, whereas m^{6}A has a post-transcriptional destabilizing effect. (c) In ESCs, 5mC and m^{6}A counteract each other on shared targets, but the balance between the two marks may shift during exit from pluripotency. Specifically, upregulation of many key differentiation genes is unlocked by a prominent increase of 5mC and reduced m^{6}A.